Title
Seismic scattering in the subduction zone of the Middle America region

Author
Dominguez, Luis Antonio

Publication Date
2012

Peer reviewed|Thesis/dissertation

University of California
Los Angeles

Seismic scattering in the subduction zone of the Middle America region

A dissertation submitted in partial satisfaction
of the requirements for the degree
Doctor of Philosophy in Geophysics and Space Physics

by

Luis Antonio Dominguez-Ramirez

2012

Abstract of the Dissertation

Seismic scattering in the subduction zone of the Middle America region

by

Luis Antonio Dominguez-Ramirez

Doctor of Philosophy in Geophysics and Space Physics

University of California, Los Angeles, 2012

Professor Paul M. Davis, Chair

Seismic scattering is the direct consequence of the changes in the elastic properties of the medium. These so-call heterogeneities play a fundamental role for the understanding of the propagation of seismic waves and their possible effect on the analysis of seismic risk. This dissertation examines the scattering properties of Middle America region at continental scale, and provides a discussion of the current methods aimed to model the effect of small-scale heterogeneities in the crust.

Using data from a portable array deployed in Mexico perpendicular to the trench, we identified and modeled trapped crustal waves that were previously undocumented. When low frequency ($f < 1Hz$) body phases from teleseismic events reach the trench from the ocean side, the lateral discontinuity between the continental and oceanic crust behaves as a line source that generates surface waves. This trapped mode travels with a significantly small attenuation through the crust as if it were propagating through a waveguide structure. Interestingly, conversion rates for this phase can reach up to 60% the amplitude of the incident phase in the vertical component. The scattered wave is better observed following the SP, PS, and SS phases for events in the southern hemisphere. Numerical models using a boundary element formulation support this hypothesis. Comparison between the simulations and the

seismic records suggested that the structure formed by the flat-subducting slab and the crust behaves very similar to a sedimentary basin but at a larger scale. These observations could explain differences in attenuation along different paths of propagation in this area.

The second part of this work focuses on the evaluation of the different component of the attenuation for local events and small scale heterogeneities. Three phenomena determine the attenuation: 1) Geometrical spreading; 2) conversion of mechanical energy into heat (intrinsic attenuation); and 3) redistribution of energy (scattering). We estimated independent measurements of intrinsic and scattering attenuation using multiple scattering models based on radiative transfer theory. Results show significant frequency dependence of the intrinsic attenuation opposite to the frequency independent intrinsic attenuation observed in laboratory experiments. We proposed an alternative model to reconcile the observation and laboratory experiment taking into account the losses of energy due to leakage into the mantle. Proper characterization of scattering properties in the Meso America region is needed to better understand the origin of coda and for a better evaluation of seismic risk maps.

The dissertation of Luis Antonio Dominguez-Ramirez is approved.

Caroline Boyce

Jian Zhang

David D. Jackson

Paul M. Davis, Committee Chair

University of California, Los Angeles

2012

To Salvador Salas

(1945-2008)

Table of Contents

List of Figures

List of Tables

Acknowledgments

This work would be impossible without the continuous support from many people through my life and academic career. First of all, I want to thank my mentor Prof. Paul Davis. Not only for guiding me through the elaboration of this work, but also for his concern and support in my personal life. Thank you for encouraging me to explore new possibilities and ideas even when I felt completely disappointed with my results. I also want to thank Prof. Caroline Boyce, Prof. Jian Zhang and Prof. Dave Jackson for being part of my committee. Thank you for your support and for giving me the opportunity to TA ESS8 and ESS135, it was been one of the most rewarding experiences at UCLA. I also want to thank to Prof. John Wasson for his concern and support during my second year.

I am grateful to Prof. Barbara Romanowicz and the Berkeley Seismo lab for hosting me during one quarter. Discussion with students and professors greatly improved the interpretation of the results. I also want to thank Prof. Igor Morozov for numerous discussion in almost every meeting, I have attended to.

I especially want to thank Prof. Xyoli Pérez-Campos who truly change my life by encouraging me to apply to UCLA. I also want to thank Prof. Francisco "Paco" Sanchéz-Sesma, it has been a great pleasure our ongoing collaboration. Thank you for sharing the IBEM code to compute the synthetic seismograms in Chapter 3 and for teaching me seismology from a unique and irreverent point of view.

I deeply appreciate all my fellow graduate students and friends. I am specially indebted to Minoo Kosarian, thank you so much for looking after me and for being role model of a scientist and human being. I truly admire your work and dedication but overall your sincere friendship. To Emily Foote, thank you for being such an enormous moral support from my very first day at UCLA. To Igor Stubailo, thank you for always being there to figure things out, for holding me the day I fainted in Paul's Office, and for numerous adventures in Peru, Mexico and the DMV. My sincere gratitude to Qi Wang and Kaiqing Yuan for your friend-

ship and programing assistance and for sharing a great adventure in Alaska. I also want to thank Ana González and her family, their friendship made me feel at home. To Hector Yuen Zhou, my best friend of many years. There are way too many things that I have to thank him. For pushing me to apply for graduate school, for helping to find my way my very first day in the US, for telling me how bad student and programmer I am otherwise I would never improve. I also want to express my gratitude to Xóchitl Flores-Marcial for her love and support through these years.

Thank you also to the ESS staff: Lauri Holdbrook, Oscar Lovera, Steve Salyards, Gloria Contreras, Gary Glessner, etc. I apologize if I cannot mention everybody. But, everyone's enthusiasm makes this department a great place to work.

Last but not least, I want to express my love and gratitude to the person that I admire the most, my querida mamacita. You are my greatest inspiration for every moment in my life and my main reason to become a better person.

Vita

1999–2005	Ingeniera en Telecomunicaciones, Universidad Nacional Autónoma de México
2006-2009	MSc. Geophysics and Space Physics. UCLA
2008–2012	Teaching Assistant, Earth and Space Sciences Department, UCLA

Publications and Presentations

Dominguez, Luis Antonio, Sanchéz-Sesma, Francisco José, Davis Paul. Scattering of teleseismic body waves by the lateral crustal heterogeneity at the Pacific trench of Mexico. Bull. Seism. Soc. Amer. Vol. 101, no. 3, pp. 1281-1290, June 2011.

CHAPTER 1

Introduction

For most of history earthquakes remained as one of the most enigmatic forces of nature. Their sporadic and erratic behavior gave rise to numerous myths and legends. Although several ancient civilizations had remarkable success explaining natural phenomena such as the orbits of the planets and the occurrence of eclipses, earthquakes remained in an aura of mystery. Not until the development of modern instrumentation in the past century, were scientists able to constantly monitor and analyze their causes and effects. We now know that thousands of earthquakes shake the earth every year, and that they are the result of the release of energy along weak areas known as faults. In addition, earthquakes have provided an invaluable tool to explore the structure and composition of the Earth's interior.

Earthquakes are not repetitive and monotonic events of nature. They occur under a vast range of circumstances and scenarios. For example, mid-ocean ridges are long-shaped features on the seafloor where new oceanic crust is constantly formed. Here, earthquakes are triggered by mechanical forces acting in opposite directions due to ascending materials from the mantle. Contrarily, subduction zones are areas where tectonic forces converge. The oceanic crust that was once formed at mid-ocean ridges is now destroyed and return to the mantle completing the super continent cycle. Interestingly, sea water plays at pivotal factor for the generation of intermediate and depth earthquakes at subduction zones (Jung et al. 2004; Billen 2009). As cold slabs sink into the mantle, changes in pressure and temperature cause metamorphic reactions that increase the pore pressure and possibly hydrofracturing that changes the effective pressure, giving rise to intermediate and deep earthquakes along

subduction zones (Green II et al. 2010). All these ingredients make every tectonic setting unique and every earthquake distinctive.

One of the major challenges for seismologists seeking to understand earthquakes is to obtain realistic models of wave propagation. The main obstacle lies in the vast number of geological conditions that can highly affect the amplitude of the seismic waves including path and site effects beneath stations. Common examples of the complexity caused by site and path effects are the 1985 Mexico City earthquake and the 1994 Northridge earthquake. The Mexico city earthquake stands out by the fact that most of the building collapses occurred $400km$ from the rupture zone. Trapping and conversion of seismic energy into the metropolitan basin amplified the seismic waves causing the collapse of dozens of buildings (Anderson et al. 1986; Eissler et al. 1986; Ekström and Dziewonski 1986; Houston and Kanamori 1986; Anderson and Quaas 1988; Bard 1988; Esteva 1988; Grigoriu et al. 1988; Seed et al. 1988; Lermo et al. 1988; Sánchez-Sesma et al. 1988; Singh et al. 1988; Mendoza and Hartzell 1989; Rosenblueth et al. 1989; Ordaz and Singh 1992; Kanamori et al. 1993). On the other hand, the Northridge earthquake revealed the potential that focusing effect can cause on the infrastructure (Hauksson and Jones 1995; Miller 1998; Gao et al. 1996; Davis et al. 2000). Modeling and understanding of the mechanisms that rule the propagation leads to a better characterization of potentially hazardous areas to human life and infrastructure. Once seismic energy is released from the earthquake, scattering modifies the propagation and power energy of the waves due to heterogeneities in the medium of propagation.

It has long been recognized that seismic waves decay at a grater rate than that predicted by pure geometrical spreading (see review by Knopoff 1964). It was proposed that most of the decay is due to the conversion of elastic energy into heat which is refered to as intrinsic attenuation. In a pioneering work, Aki 1969 shown that scattering of energy due to the heterogeneities in the medium also contributes to the attenuation of the energy. Although significant progress has been achieved through the years (Morozov 2009; Sato and Fehler 2009; Xie 2010), separation of the intrinsic and scattering components of attenuation is still

an unsolved problem.

Aki and Richards 1980 classified the scattering regimes of seismic wave propagation according to the ratio between the scale length of the heterogeneity a, the travel distance L and the wavelength λ. Figure 1 shows this classification using the non-dimensional numbers ka and kL. This diagram indicates the regions of validity of the different models of propagation. The product kL can be reinterpreted as 2π times the travel distance L divided by the number of wavelengths λ; and the ka as 2π times the characteristic size of the heterogeneities in wavelength units. A medium is considered homogenous when either the travel distance is smaller compared to the scale length $L < a$, or when the the scale length of the heterogeneities is much smaller than the characteristic wavelength. Ray theory is bounded by the isoline $D = 1$, where D is the wave parameter defined as $D = 4L/ka^2$. This is the ratio between the Fresnel zone and the characteristic scale length of the inhomogeneity. Perturbation methods are needed when the wavelength, the characteristic scale of the medium, and the travel distance are comparable.

Wu and Aki 1985 provided a phenological classification of the scattering problems using the non-dimensional parameter ka:

i) $ka \lesssim 0.01$. Weak scattering regime. Under this condition, wave propagation is accurately modeled using homogeneous-medium approximation. Waves attenuate mainly due to the geometrical spreading of the waveform and intrinsic attenuation of the medium.

ii) $0.01 \lesssim ka \lesssim 0.1$ Rayleigh scattering regime. Loss of energy under this range is highly dependent on frequency, scattered power is proportional to k^4 and in all directions. The color of the sky is a typical example of scattering under this regime. The characteristic scale of the molecules of air is small compared with the wavelength of the visible light. As a result, short wavelengths (blue colors) dominate the spectrum.

iii) $0.1 \lesssim ka \lesssim 10$. Propagation in the Mie scattering characterizes by a weak frequency

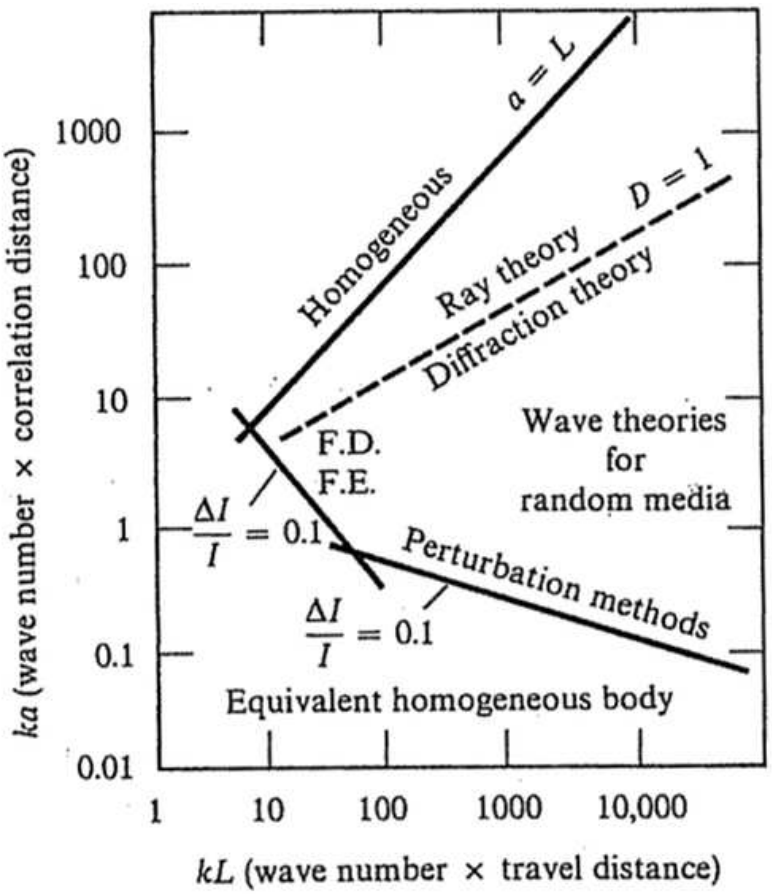

Figure 1.1: Classification of scattering regimes as a function of the products ka and kL. a and L are the correlation and travel distances, and k is the wavenumber. From Aki and Richards 1980.

dependance and forward scattering. For example, particles of water contained in clouds have a characteristic scale large enough to generate Mie scattering. Therefore, all visible wavelengths are equally scattered which is why clouds appear white in the sky.

iv) $ka > 10$ High or infinite frequency regime. In this case, propagation is determined by the geometry of the interface. Ray theory predicts effects such as focusing, defocussing and interference. Refraction and reflection angles between two media with different elastic properties are adequately computed by means of the Snell's law, and amplitudes

by reflection and refraction coefficients.

Research results documented here focus on the scattering properties of the Middle American region. A collaborative project between UCLA, the California Institute of Technology and the National Autonomous University of Mexico deployed a portable broadband seismic array in 2005-2007. The main target of this project was to image the geometry of the subduction zone and explore the seismic features along a profile perpendicular to the trench.

Chapter 2 reviews the geological history and tectonic features of the Middle America region. This chapter highlights the importance that this region has for the understanding of the dynamics of subducting slabs at a global scale. Several studies using P- wave (Husker and Davis 2009), surface waves (Iglesias et al. 2010; Stubailo et al. 2012), ambient noise (Gaite et al. 2012), and Q (Chen and Clayton 2009) tomography, receiver functions (Pérez-Campos et al. 2008; Kim et al. 2010), and relocated earthquakes (Pardo and Suarez 1995) suggest that the Cocos plate subducts nearly horizontal, $\sim 10\,km$ below the Moho, for about $\sim 250km$ from the trench. The present work examines the consequences that this geometry has on the wave propagation due to the flat nature of the subducting slab.

Chapter 3 reports the waveguide properties of the Middle America region for teleseismic events. This section examines the characteristics of an anomalous phase detected using the MASE array. Observations show that body phases coming from the southern hemisphere convert into surface waves at the trench. I discuss under which circumstance this conversion occurs. Distinction between the incident and scattered field is carried out using the $\tau - p$ transform and fk analysis. In addition, synthetic seismogram suggest that trapping of the scattered field is the result of the flat geometry of the subducting slab. In this case, low frequency ($< 1\,Hz$) body waves are scattered by the trench and trapped into the crust. Dimensional analysis suggest that Mie scattering is the dominant regime for the generation and propagation of the scattered field.

Chapter 4 reviews the modeling of coda waves and the estimation of the attenuation. Het-

erogeneous nature of the crust ranges from grain size to meters long discontinuities that induce the generation of scattered waves in the Rayleigh regime and km sized layers that forward scattered waves in the Mie regime. The combination gives rise to coda waves. In this section, I present the evolution of the different models of coda, and the current techniques aimed to separate the contribution of the scattering attenuation from the total attenuation. In Chapter 5, I applied the Multiple Time Lapse Window (MTLW) analysis to the MASE array data as well as permanent stations along the Pacific trench of Mexico. I focus the discussion on the effect that different assumptions have on the separation of intrinsic and scattering attenuation. In particular, I analyze the consequences of assuming that the geometrical spreading factor is spherical and that the radiation pattern at a given scattering point is isotopic. In addition, I consider two different velocity models: 1) a depth dependent two-layer model representing the crust and the mantle, 2) an infinite medium with constant velocity. This chapter seeks to reconcile lab experiments which suggest that intrinsic attenuation remains constant in the frequency range of $0 \leq f \leq 100 Hz$ (Lindsay 1914; Knopoff 1964; McKenzie et al. 1982; Jackson 1993; Cao and Jackson 1996; Jackson 2000; Romanowicz and Durek 2000), and field estimates (Mayeda et al. 1992; Fehler et al. 1992; Hoshiba et al. 2001; Jin et al. 1994; Feustel et al. 1996; Tselentis 1998; Akinci and Eyidoğan 2000; Badi et al. 2009; Chung et al. 2010) which show a strong frequency dependance in the same range.

Chapter 6 deals with the analysis of coda waves using a very high dense seismic array in Long Beach, California. This novel experiment, deployed by a prospecting oil company (Nodal Seismic), consisted of nearly five thousand station spaced every $\sim 100\, m$. Geometry and location of this array offer a unique opportunity to explore the nature of coda waves at frequencies between $1 \leq f \leq 20\, Hz$. I examine the seismic records for two local events (Mw = 2.5, Mw = 3.4) to determine the transition between coherent forward scattered body waves and the onset of incoherent coda waves. I propose the use of the entropy of the array as a metric to resolve the coherency in the data and the self-similarity of the waveforms as

they propagate though the network. This result sheds remarkable insight into the existing models of scattering. Lastly, general conclusions are presented in Chapter 7.

CHAPTER 2

Tectonic Setting

2.1 Introduction

The Middle America Region (MAR) is a geographic region where the Cocos, Riviera, and North America converge. It is one of the ten subduction zones of the world where the slab subducts at a very shallow angle known as flat subduction zones (Gutscher et al. 2000; Gutscher et al. 2000). The major scientific importance of this area from the geological and tectonic point of view resides in understanding what are causes of flat subduction. Several authors have proposed different mechanisms to explain the change in geometry (Gephart 1994; Gutscher 2002; Lallemand and Hueret 2005; Schellart 2008; Wagner et al. 2008) however an unified theory is still missing (Skinner and Clayton 2011).

Figure 2.1 shows the present configuration of these plates, the major fractures zones, and the focal mechanism along the edges of the plates. At the present time, the Cocos and Rivera plates subduct underneath the North America plate at a rate of 5-8 cm/yr (Muller et al. 2008). The evolution of the Cocos and Rivera plates has been highly controversial (Bandy and Mortera-Gutierrez 1995, DeMets and Wilson 1997, Bandy et al. 1998, Suarez et al. 1990). It is believed that the Rivera plate detached from the Cocos Plate from 5-10 Ma (DeMets and Traylen 2000). This event led to the reorganization of the tectonic structure forming a triple junction with a diffuse oblique extension zone in the area between these two plates. The deformation zone extends both inland and offshore forming the Colima rift and the Manzanillo graben, respectively (Stock and Lee 1994). Gorbatov and Fukao 2005

suggested that a tear in the ancient Farallon plate $\sim 25\,Ma$ gave rise to present configuration of the Cocos plate and subsequent fragmentation of the Rivera plate. Seismic tomography images (Yang et al. 2009) suggest that differential subduction rates between the Cocos and Rivera plate formed a gap at depth between the two plates. Unusual volcanism in this area can be explained by rollback of the Rivera plate and toroidal flow of the mantle wedge (Pérez-Campos et al. 2008; León Soto et al. 2009; Manea and Manea 2011; Skinner and Clayton 2011). In addition, trench retreat can be explained as the result of the transition from dipping to flat subducting regime of the Cocos plate likely caused by the detachment of the Farallon plate.

The Cocos plate shows three major morphological structures that intersect the trench from the ocean side. The Orozco and O'Gorman fracture zones extend from the East Pacific Rise (EPR) to the trench without interfering with the tectonic setting. Contrarily, the Tehuantepec ridge (TR) marks a diffuse triple point between the Cocos, the Caribbean and the North America plate (Manea et al. 2005). A striking difference between the Rivera and Cocos plate is their distinctively dipping angles. Whereas the Rivera plate subducts at an angle of $\sim 60°$, the Cocos plate has a variable dipping angles that ranges from subhorizontal in Central Mexico to steep angle $\sim 50°$ in the flanks of the plate. The Rivera plate forms a transition zone between the Middle America trench and the spreading center in the Gulf of California with a dipping angle of $60 - 65°$ (Yang et al. 2009). The geological history of this area has been traced to the collision of the Pacific-Farallon seafloor spreading center and the North America plate 28Ma ago (Atwater 1970; Atwater and Stock 1998). Subduction of the Farallon plate in the early Cenozoic formed the Sierra Madre Occidental, a northwest structure that covers a large part of central and western Mexico whose volcanism is typical of a subduction zone (Ferrari et al. 1999). As the spreading center approached the trench, the Farrallon plate fragmented into three major plates: Juan de Fuca, Cocos and Nazca plates (Mammerickx and Klitgord 1982; Stock 1988). The Cocos plate then fragmented into several ephemeral microplates: the Monterrey ($\sim$ 30 to $19Ma$), the Arguello($\sim$ 20

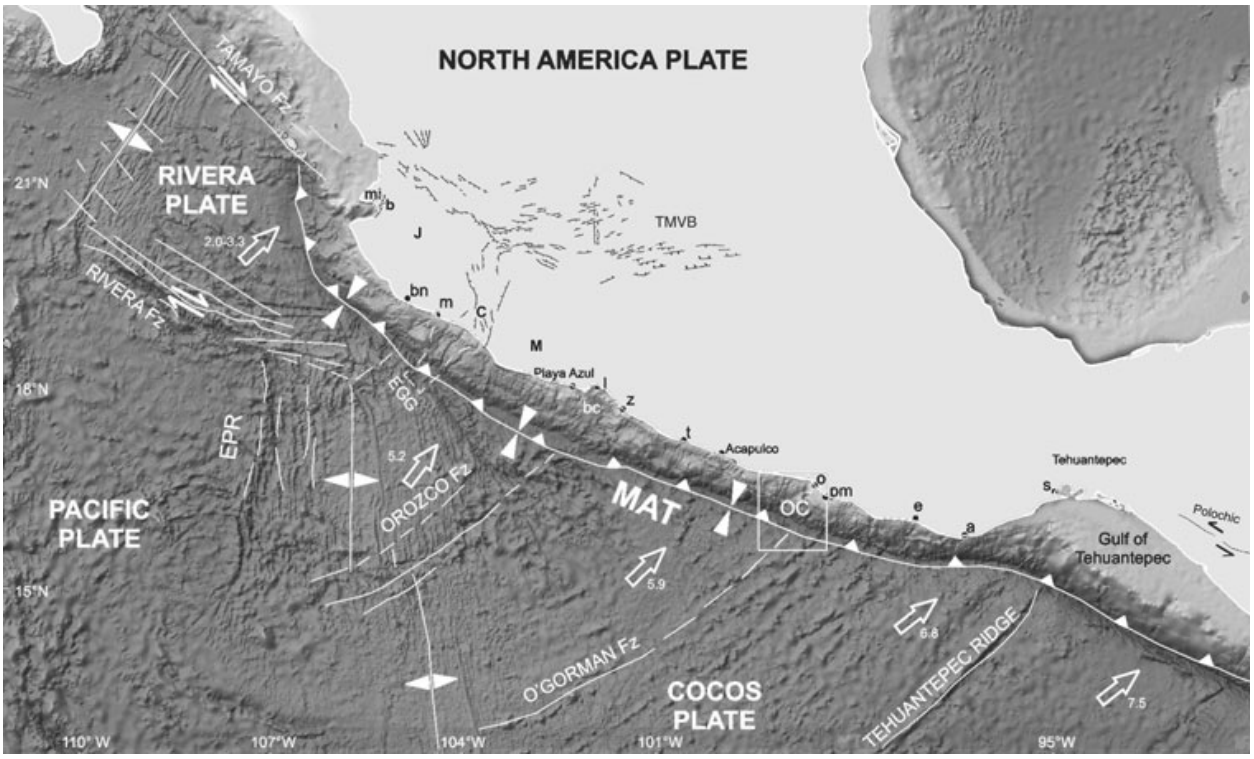

Figure 2.1: Simplified tectonic map of the Middle America Region. MAT Middle America trench; EPR East Pacific Rise; EGG El Gordo Graben; Fz fault zone; J Jalisco block; C Colima graben; M Michoacan block.(Ramírez-Herrera et al. 2011)

to $\sim$ 18Ma), the Guadalupe ($\sim$ 20 to $\sim$ 14 Ma) and Magdalena (14 to 12 Ma) plates. These shorth-lived microplates detached from the Cocos plate and subducted west of Baja California. Interestingly, the subduction process ceased without leaving a corresponding geological record. In contrast, the detachment and subduction of the Riviera plate shows a strong deformation of the overlying crust (Stock and Lee 1994).

Several types of volcanism are found in the vicinity of the triple junction. Alkaline lavas typical of rifting process superimposed calc-alkaline volcanism related to the subduction process. The tectonic evolution of these plates gives rise several questions. Is the detachment of the Riviera plate responsible for the uneven seismic distribution (Pacheco and Singh 2010)? is the Trans- Mexican volcanic belt anomalous signature and geometry consequence of the

Figure 2.2: Stratigraphic Terrenes by Campa and Coney 1983. Shaded areas show volcanic provinces.

detachment of the Farallon plate(Ferrari 2004; Verma 2002)? What are the mechanisms that connect the tectonic configuration with the geological and seismic features of this region?

2.2 Geology

The geology of the Middle America Region can be subdivided into twelve distinctive terranes (see Fig. 2.2), classified into three categories according to their geomorphological origin (Campa and Coney 1983): (1) the North American provenance - (Chihuhua and

Caborca terranes), (2) Gondwanan provenance - (Maya, Coahuila, and Sierra Madre terranes), and (3) Pacific provenance (Alisitos, Vizcaino, Guerrero, Juarez, Mixteca, Oaxaca and Jalapa terranes). The Chihuhua and Caborca terranes are located in the northwestern Mexico. Formed in the Precambrian, their outcrops have strong similarities with lithologies in Arizona and California. In eastern Mexico, the Coahuila, Maya and Sierra Madre terranes formed as a the result of the opening of the Gulf of Mexico. Rift assemblage of continental redbeds and evaporites in the upper Mesozoic and Cenozoic gave rise to these formations. Finally, accretion of Mesozoic terranes in the late Cretaceous originated the Pacific provenance.

The western margin of Mexico resulted from the continuous subduction process that started 160Ma (Keppie 2004). The Sierra Madre Occidental (SMO) is the largest volcanic province in this region. It extends N-S from the Mexico-US border to the Tehuantepec isthmus. It is composed mainly of silicic ignimbrites that cover $300,000 km^2$ formed by the subduction of the Farallon plate and the opening of the Gulf of California from the Cretaceous to the Cenozoic, also know as the southern (or Mexican) Basin and Range province, it is a typical example of subduction-related calc-alkaline province. Two major episodes of ignimbrite flare-up occurred in the southern section of the SMO in the Oligocene and early Miocene (Ferrari et al. 2002). Lack of compressional structures in the last 20Ma suggest detachment and rollback of the slab (Nieto-Samaniego et al. 2006; Morán-Zenteno et al. 2007).

The Sierra Madre del Sur (SMS) comprises the geological terranes of: Guerrero, Oaxaca, Juarez, Xolapa and Mixteca (Sedlock et al. 1993). It is a non-volcanic mountainous range formed by the present subduction of the Cocos plate and the former Farallon plate. The SMS is located south of the TMVB and bordered on the East by the Isthmus of Tehuantepec. Gravitation and seismic studies suggest crustal thickness of $25 - 40 km$ (Valdés et al. 1986; Urrutia-Fucugauchi and Flores-Ruiz 1996). It was initially formed by a major shortening event in the late Cretaceous related to the Laramide orogeny of the North America Cordillera (Dickinson and Lawton 2001). The SMS is also characterized by an extensive distribution

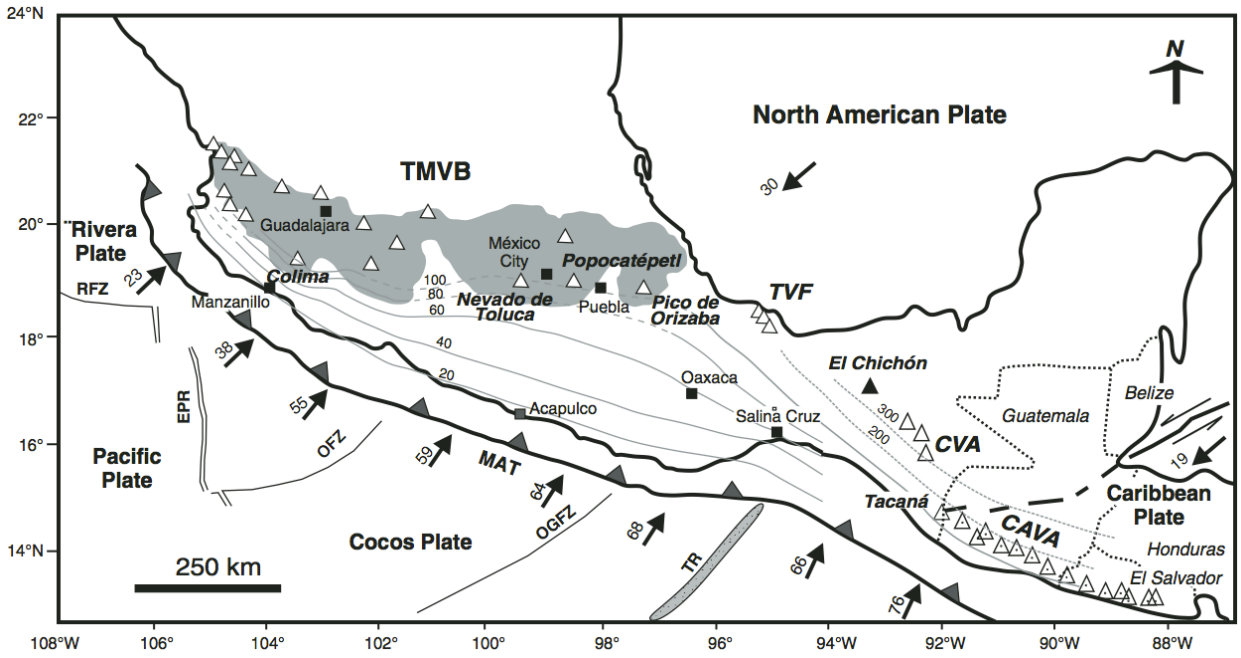

Figure 2.3: Map of major volcanic structures along the Middle America region. Triangles indicate location of the active volcanoes. RFT - Rivera Fracture zone, EPR - East Pacific Rise, OFZ - Orozco Fracture Zone, MAT - Middle America trench, TR - Tehuantepec Ridge, TMVB - Trans-Mexican Volcanic Belt, CVA - Chiapanecan Volcanic Arc, TVF - Los Tuxtlas Volcanic field, CAVA - Central America Volcanic arc. After Macías 2007.

of plutonic bodies aligned along the trench (Morán-Zenteno et al. 1996).

2.3 Volcanism

The Middle America region shows a large number of volcanic structures with diverse origins (See Fig. 2.3). In addition to the igneous structures found along the SMO described in the former section, northern and central Mexico exhibit numerous intraplate-type volcanoes formed in the late Cenozoic (Aranda-Gómez et al. 2007). These structures cannot be explained by extensional state of the stress in the crust. An alternative hypothesis suggests

that detachment of the Farallon plate opened up "a slab window" (Van Der Lee and Nolet 1997). Therefore, upwelling of mantle material triggered the intra-plate volcanism in this area. Another interesting feature of the volcanic lavas found in this region is their unexpected geochemistry. Younger rocks (Pliocene-Quaternary) show more primitive signatures than older samples (late Oligocene-Miocene) with little or no assimilation. The chemistry of the older samples indicates greater degrees of differentiation and contamination.

In the South, the Central America Volcanic (CAV) arc forms a trench-parallel structure that extends from Panama to southeast Mexico. The Tacána volcano, located at the Mexico-Guatemala border, marks the northern end of this structure. Volcanism reappears inland at the Chipanecan volcanic arc (CVA) $200km$ from the trench. Numerous authors (Nixon 1982; Burbach et al. 1984; Pardo and Suarez 1995) suggest that change in the geomorphology of the volcanic arc is likely due to changes in the geometry of the subduction zone and extensional changes at the triple junction between the Caribbean, Cocos and North America plates. The CVA forms a scattered group of low-relief structures with alkaline signature formed in the Pliocene to recent age (Damon and Montesinos 1978). Lastly, El Chichón volcano is the youngest and more active structure of this group. Located between the CVA and Los Tuxtlas Volcanic Field (TVF), erupted on March 28, 1982 causing the death of $20,000$ people.

In the Pacific Ocean, along an abandoned ocean ridge, oceanic type volcanoes form isolated islets named Revillagigedo, Socorro and Guadalupe islands. Other areas of small concentrated volcanism can be found in the NW states of Baja California (San Quintín volcanic field and Tres Vírgenes volcanic complex), Sonora (the Pinacate volcanic field) and the SE states of Veracruz (Los Tuxtlas volcanic field) and Chiapas (the Chiapanecan volcanic arc). The largest and most active volcanoes are located in the front arc of the TMVB between the latitude 19° and 20°. Some of the major stratovolcanic strucutures are: Pico de Orizaba (Citlaltépetl), Colima, Popocatépetl, Paricutín, Nevado de Toluca, Tacána, and El Chichón. The geochemical composition of these volcanoes varies from andesitic-dacitic (Citatépetl,

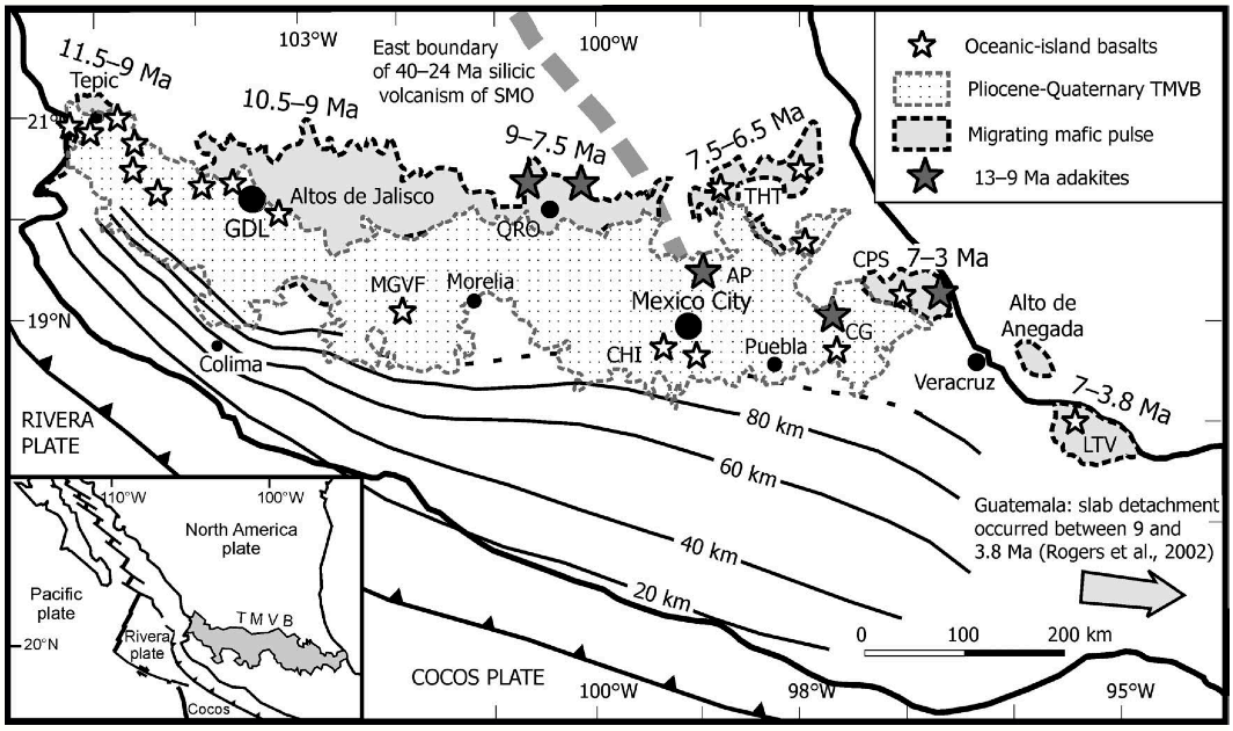

Figure 2.4: Schematic representation of the geological evolution of the TMVB. Depth contours indicate the location of the slab (Pardo and Suarez 1995). Stars show small regions of OIB type volcanism and adakites. Note the eastward migration of the mafic pulse. After (Ferrari 2004).

Popocatépetl, Nevado de Toluca), andesitic (Colima and Tacaná) to trachyandesitic (El Chicón) (Macías 2007). The Popacatepétl volcano is perhaps the greatest volcanic risk in this area. Located $65km$ from the Mexico City, a potential eruption will threaten the lives of 20M people. First eruptive reports date from 1363 as shown in pre-hispanic records to the present time (1994-2007) (Macías 2007).

2.4 Formation of the Trans-Mexican Volcanic Belt

The origin of the Trans-Mexican Volcanic Belt in Mexico is highly controversial. Several authors (Ferrari et al. 2001; Ferrari et al. 2005; Sheth et al. 2000; Verma 2002) have proposed different models to explain its unusual orientation and irregular chemical signature. In this region, calk-akaline volcanism associated with subduction zones; ocean island basalts; and alkaline volcanism coexist (Marquez et al. 1999). Two major volcanic provinces overlap in this area: The Sierra Madre Occidental (SMO), the Trans-Mexican Volcanic field (TMVB). The Sierra Madre Occidental is the largest ($\sim 296,000 km^2$) and oldest volcanic structure of Mexico ($\sim$26-32 Ma). It extends roughly $\sim 2,000\, km$ N-S and is composed of silicic ash flows and rhyolitic lavas (Moore et al. 1994). This volcanic province was formed due to the subduction of the Farallon plate and exhibits two major periods of volcanism at $\sim$30 Ma and $\sim$23 Ma (Ferrari et al. 1999). Motion of the Chortis block (Caribbean plate) in the Neogene progressively modified the boundary between the Farallon plate and the North America plates causing uplift of the subduction zone (Morán-Zenteno et al. 1996).

The TMVB is an unusual example of a volcanic arc in a subduction zone, it extends for about $\sim 1000 km$ E-W, from the city of Puerto Vallarta in the Pacific coast to the state Veracruz in the Gulf of Mexico. The eastern end of the arc is located $\sim 150\, km$ from the trench whereas the western end is about $\sim 400\, km$ away from the trench. It contains more than $8,000$ structures with different lithologies including: stratovolcanoes, domes, calderas and monogenetic cone fields (Gómez-Tuena et al. 2011). Calc-alkaline volcanism is dominant but small areas of alkaline OIB-type basalts can be found along the Colima graben in the western side of the arc, and along the the Sierra Chichinautzin south of Mexico city (Luhr 1997; Marquez et al. 1999).

Two episodes of volcanism indicate southward migration of the arc (Marquez et al. 2001). During the Mio-Pliocene a massive volume of mafic volcanism formed the northern section of the arc between 11Ma to 6Ma (Ferrari et al. 1999). From the Pliocene to the present

volcanism migrated southward forming the front arc where the largest stratovolcanoes (ex. Pico de Orizaba, Popocatepetl, Iztlacihuatl) and monogenetic cones (ex. Paricutín, Michoacán-Guanajuato Volcanic field) are located. Coexistence of poligenetic and monogenic volcanoes in the same area can be explained by either differential magma supply rate (Fedotov 1981) or regional differential stress (Takada 1994). Alaniz-Álvarez et al. 1998 proposed that the dominant mechanism to explain the coexistence of volcanism is the state of the stress. Monogenic volcanoes are preferentially oriented parallel to structures with high displacement rates while stratovolcanoes have the tendency to form along structures with low displacement rates.

A well accepted model for the formation of the TMVB was proposed by Ferrari 2004. Figure 2.5 illustrates the geological evolution and formation according to this model. Initially, a broad volcanic arc was formed in the Miocene ($17 - 10Ma$) with a typical subduction zone signature Gómez-Tuena et al. 2011. Andesitic to dacitic volcanism extended eastwards from the western end of Michoacan (longitude 102°) to the Gulf of Mexico (longitude 96.5°). Plate reorganization initiated by the subduction of the Magdalena microplate (12.5Ma) triggered a tear in the slab. The tear opened up a slab window (Fig. 2.5) that allowed seepage of hot material from the mantle wedge. Initiation of the tear most likely occurred on the southern end of the Baja California. Extensional structures such as the Colima graben agreed well with this hypothesis. Mafic volcanism indicates that the tear in the slab propagate eastward from 11Ma to 5Ma. Between 7.5Ma and 3.5Ma, large silicic complexes and calderas formed in the west side of the TMBV between Tepic and Mexico City. An additional evidence of the tear in the slab is the decrease in the plate motion of the Riviera plate with respect to the North America plate (DeMets and Traylen 2000). Between 9Ma and 7Ma, the rate convergence decreased from $\sim 50mm/yr$ to $\sim 12mm/yr$. Reduction of the plate motion is likely due to the loss of pull force exerted by the subducting slab after the detachment. OIB-type volcanism appeared after the detachment of the slab between 5Ma to 3.5Ma, different scenarios have been proposed to explain this apparent contradiction in the tectonic setting.

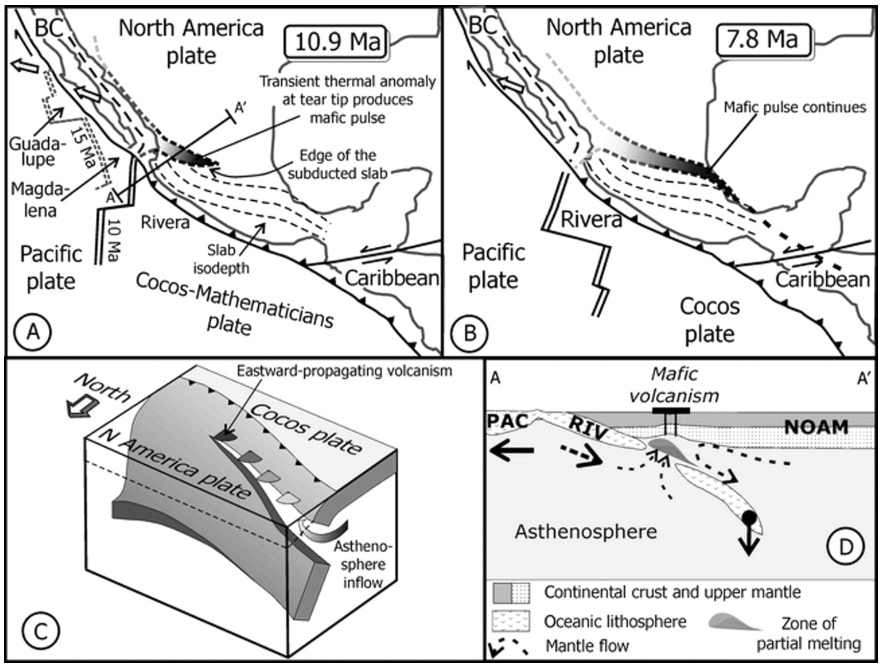

Figure 2.5: Schematic model proposed by (Ferrari 2004). A tear in the slab in the late Miocene propagated eastwards, the gap between the slab and the asthenosphere gave rise to the OIB volcanism along the TMVB.. A) shows the tectonic setting $10.9\,Ma$, subduction of the Magdalena plate initiates a tear in the slab. B) Eastward propagation of the tear induced a mafic pulse that gave rise to OIB type volcanism along the TMBV. C) 3D scheme showing the flow of hot material from the asthenosphere. D) Diagram along the cross section AA' in A, RIV - Riviera plate, NOAM - North American plate, PAC - Pacific plate.

Based on geochemical analysis of the lavas, Marquez et al. 1999 suggested the existence of mantle plume beneath the TMVB. Verma 2002 proposed that OIB lavas originated from continental rifting caused by upwelling of mantle material. Nonetheless, opponents to these theories point out that plate motion reconstructions fail to predict the location of the OIB-lavas. Moreover, regional geology does not show evidence of crustal uplift. Lastly, the OIB-volcanism appears in small volumes compared to other continental flood basalts.
Ferrari et al. 2001 introduced a comprehensive model for the generation of OIB- volcanism.

Geological data, plate tectonic history and petrological observations suggest that the slab started to rollback at the end of the Miocene. This is another possible consequence of the tear of the slab and decrease in the subduction rates. Differential stress at the tear induced melting of the mantle wedge generating lavas with OIB- signatures.

Another factor to take into account is the crustal assimilation along the TMBV. For example, the Colima volcano, at the eastern end of the arc, shows lower levels of crustal assimilation compare with other volcanoes located further inland such as the Popocatepetl, Citlatepetl, Nevado de Toluca and Pico de Orizaba (Lassiter and Luhr 2001). Crustal assimilation is commonly related to the age, composition and storage time at the base of the crust. Therefore, it is also an indicator of the crustal evolution.

The mechanisms that cause slab detachment are still unclear (Davies and Von Blanckenburg 1995). Cloos 1993 pointed out that the age of the subducting slab determines the buoyancy as in sinks into the mantle. However, a possible tear in the Farallon plate in the Middle America region suggests a different scenario.

2.5 Seismicity

Seismic observations in Mexico describes the behavior of the seismogenic zone. Pardo and Suarez 1995 analyzed the geometry of the subduction by relocation of local and teleseismic events. This study provided strong evidence of the lateral variation of the subduction angle of the Cocos plate that revealed a very shallow angle of subduction in the central part of the subducting Cocos plate. In addition, relocated events showed a poorly defined Wadati-Benioff zone and irregularly distributed seismicity (Singh and Pardo 1993). Most of the earthquakes cluster towards a narrow band of $\sim 80km$ from the trench, seismicity becomes absence at depths greater that $\sim 60\,km$. Pacheco and Singh 2010 investigated the state of the stress and seismicity of this area. They defined three distinctive areas of seismicity as a function of the distance to the trench by analyzing the focal mechanisms. (1) Coupling

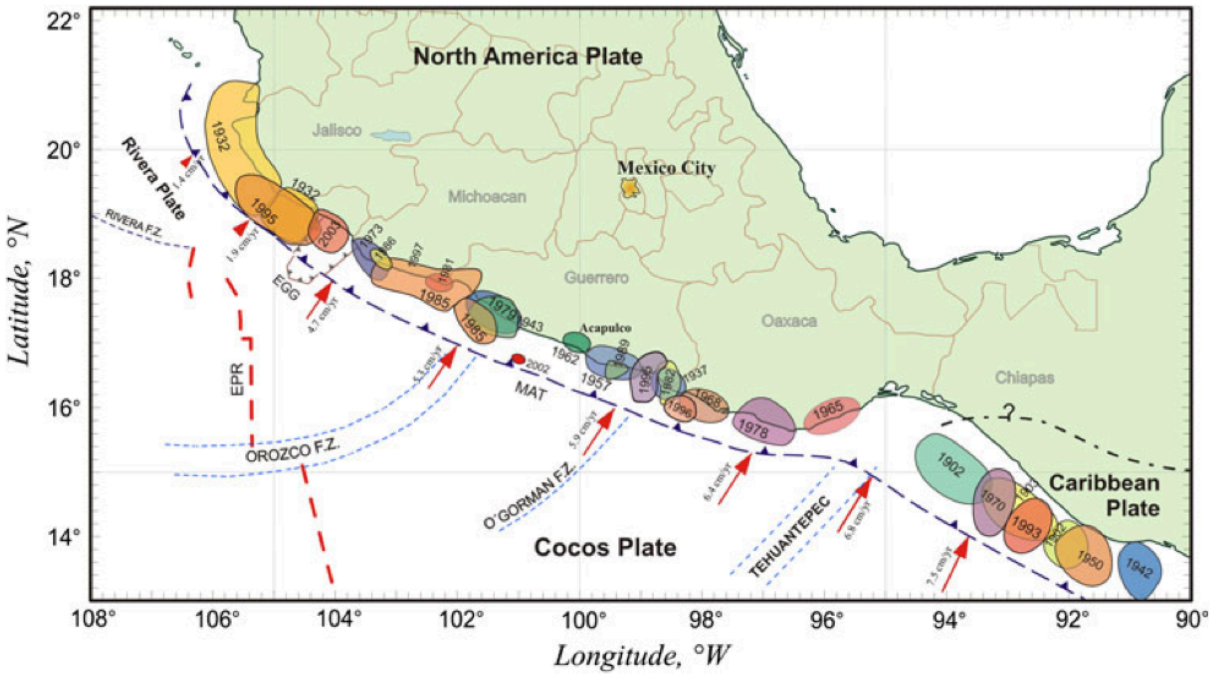

Figure 2.6: Ruptures zones of major events reported in last century. Variation in the plate motion is indicated by arrows along the trench, numbers inside the shaded zone indicate the year. By Ramírez-Herrera et al. 2011.

between the slab and the overriding plate is stronger at a distance $\sim 80-105\,km$ from the trench and at a depth $25-45km$, focal mechanisms in the area show down-dip compressional and extensional events are associate with the unbending of the slab. (2) Between $\sim 105-160\,km$ seismicity drops drastically and restarts sparsely between (3) $160-240\,km$ where it stops completely as the slab changes its sub-horizontal subduction angle and sinks into the mantle.

Large megathrust events occur at a shallow depth next to the trench as shown in Figure 2.6. For example, the June 3 1932, Manzanillo earthquake, and their aftershock generated a local tsunami that caused considerable destruction in the coast of Colima (Okal and Borrero 2011). Another important event is the great $Mw = 8.1$ Michoacan earthquake occurred

in September 19, 1985 (Anderson et al. 1986; Singh et al. 1988). This event had its epicenter $400km$ away from Mexico City where most of the destruction occurred due to amplification of the seismic wavefield in the metropolitan basin. Doublet events have also been reported along the subduction zone . On June 7, 1982 two earthquakes magnitude $Mw = 6.9$ and $Mw = 7.0$ occurred within few hours in Ometepec, Guerrero (Astiz and Kanamori 1984). Occurrence of this kind of events may be caused by a local distribution of comparable-size asperities along the trench. Also notice in Fig. 2.6, two areas known as seismic gaps in Tehuantepec region and near the city of Acapulco that have no historical record of major earthquakes (Singh et al. 1981; Suarez et al. 1990). Location of these regions of low seismicity represent an major seismic hazard as pointed out by Kanamori et al. 1993. If an event similar to the Michoacan earthquake occurred within the Guerrero gap, the spectral response at Mexico city is predicted to reach amplitudes twice as large as the 1985 Michoacan earthquake. Although large megathrust events occur mostly along the subduction zone, other large events such as 1912 $M_w = 7.0$ Acambay earthquake (Singh et al. 2011) occur inland near large urban areas.

Non-volcanic tremor (NVT) has been documented on the horizontal section of the Cocos plate. Payero et al. 2008 found two clusters of NVT located at $\sim 150 - 170\,km$ and $\sim 210 - 240\,km$ from the trench. A thermal model by Manea et al. 2004 predicts that fluid migration is expected to occur at these distances due to metamorphic transitions from the oceanic crust. NVT occurs at a depth of 40 to $50km$ where the blueschist-eclogite dehydration takes place at $450°C$. (Hacker et al. 2003). In a recent paper, Husker et al. 2012 reported that tremor highly clusters at an epicentral distance of $\sim 215\,km$ from the trench which is claimed to provide adequate pressure, temperature, and fluid content. In addition, they reported that there is a strong correlation between the NVT and SSE.

Silent earthquakes or slow slip events are also observed and provide new clues into the causes of the flat subduction and the sparse seismic activity of flat section of the Cocos plate. Lowry et al. 2001 first reported a moment magnitude release $Mw \geq 6.5$ in Guerrero. Kostoglodov

et al. 2003 and Yoshioka et al. 2004 described an equivalent $Mw = 7.5$ SSE in the Guerrero gap. This event started in October 2001 and lasted for $6 - 7$ months. Additionally, Franco et al. 2005 reported the detection of SSE in the Oaxaca region in 2001-2002. Another large SSE was documented by Radiguet et al. 2011. This event had a maximum displacement of $15cm$ over a length scale of $25km$, and a equivalent $Mw = 7.5$. Walpersdorf et al. 2011 observed two other events with similar magnitude occurred in 2009-2010. Vergnolle et al. 2010 reviewed GPS observations from 1997-2008 that shows a regular but aperiodic activity in the Guerrero gap. Larson et al. 2007 investigated the crustal deformation associated of a $Mw = 7.5$ also occurred in the Guerrero region. SSE show a well-define seismic cycle of loading and unloading mechanism as illustrated by Cotte et al. 2009.

Song et al. 2009 proposed a possible mechanism for the generation of SSE. Conversion of Sp phases at the interface between the slab and the overriding plate indicates a thin ultra low velocity layer ~ 2 to $2.7\,km/s$ with a variable thickness $\sim 3-5\,km$. This layer correlates well with areas where SSE have been detected, and it is an indicator of the poor coupling of the slab. Kim et al. 2010 provides a possible scenario to reconcile the seismological observation along the subduction zone. Inversion of the amplitude of the receiver functions reveals that the presence of weak hydrous minerals on top of the oceanic layer reduces the shear modulus at the interface between the slab and the continental crust. Further, existence of high pore pressure related to fluid release from the slab correlate well observation of SSE and NVT, similar results have been found in Japan and Cascadia (Audet et al. 2009; Rubinstein et al. 2010). Observations in Mexico (Kostoglodov et al. 2010; Vergnolle et al. 2010) demonstrated that NVT is intensified during periods of large slow slip events.

Seismicity in the Guerrero and Oaxaca can be summarized in the following way. Unlike other subduction zones along the Pacific rim, the middle America region does not show evidence of either deep events or a well-defined subduction zone. These differences in seismicity are most likely due to the geometry of the subducting slab, although the causes are still not well understood (Skinner and Clayton 2011). Lack of seismicity in the dipping section of the

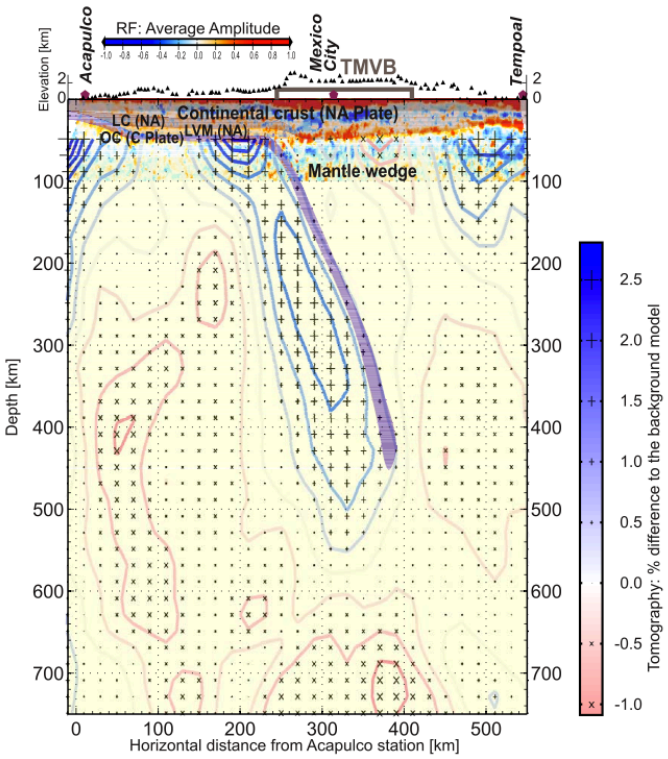

Figure 2.7: Combined results showing P- wave tomography of the slab overlaid by the receiver function analysis of the lithosphere down to $100\,km$. Observed truncation of the slab at $\sim 500\,km$, and variations of the Moho at $\sim 40\,km$. C = Cocos plate, NA = North American plate, LC = lower crust, LVM = low velocity mantle, and OC = Oceanic crust. By Pérez-Campos et al. 2008.

slab is still an unresolved problem. Detachment from the flat section could results in lack of stress in addition to high temperatures for brittle failure (Jackson et al. 2008) as suggested by numerical simulations (Manea and Gurnis 2007).

2.6 Structure of the upper mantle and the subducting slab

Structure of the upper mantle and geometry of the subducting slab have prompted strong interest in this area. Several authors have examined the geometry of the subducting slab

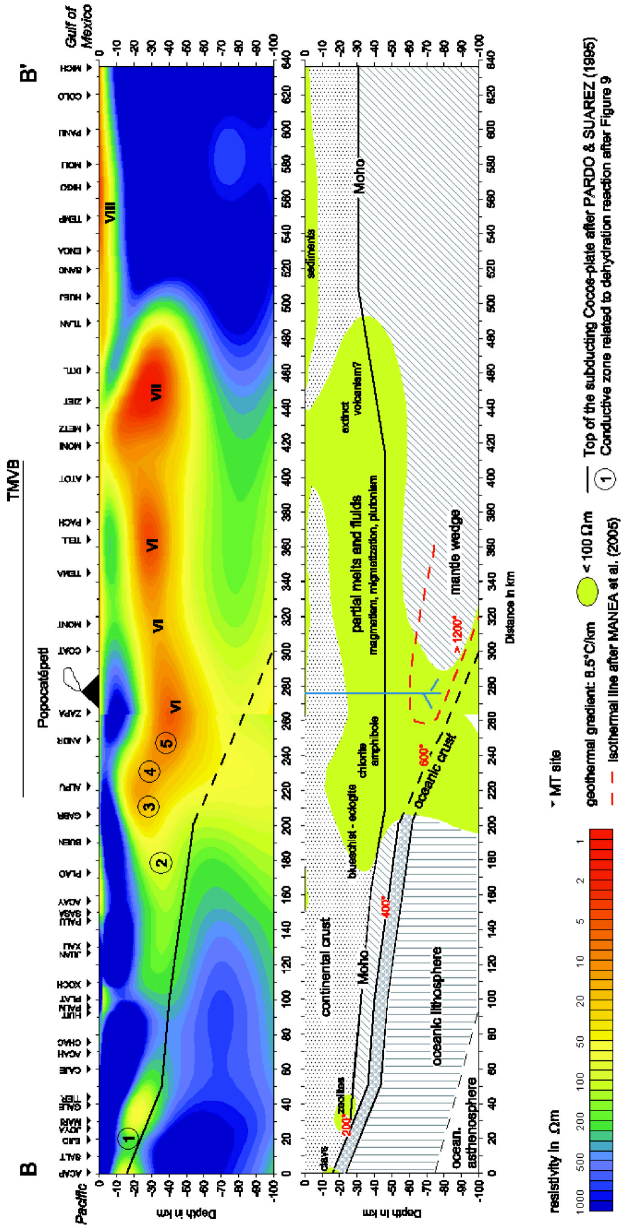

Figure 2.8: Magnetotelluric profile and mineralogical interpretation by Jödicke et al. 2006. The profile was carried out from the cities of Acapulco to Tampico perpendicular to the trench.

using different techniques. Couch and Woodcock 1981 inferred the thickness ($\sim 9\,km$) of the oceanic crust using magnetic and gravity data along a profile perpendicular to the trench near Acapulco. This study suggested a very shallow angle of subduction in the continental margin of about $\sim 2°$. Kostoglodov et al. 1996 refined this model by introducing seismological and gravitational constraints. Valdés-González and Meyer 1996 examined the aftershocks of the Petatlán earthquake, their model suggest a $45km$ depth Moho and a $8km$-thick slab subducting an $10°$ between the Pacific coast and Mexico City. Pérez-Campos et al. 2008 reported the receiver function analysis of the horizontal section of the slab revealing a low velocity channel between the continental crust and the oceanic mantle. Husker and Davis 2009 obtained the P- wave tomography of this area. Based on a tomographic thermal model, they concluded that the slab subducts horizontally from the trench up to $250km$ inland before plunging $\sim 507 - 520km$ into the the mantle at an angle $\sim 74°$ (See Fig. 2.7). Iglesias et al. 2010 carried out surface wave tomography of this area, their results indicate a zone of low velocity zone beneath the TMVB at a period of $\sim 20s$ related to the mantle wedge. This result is in agreement with attenuation of Lg waves (Singh et al. 2006) and Q tomography of the mantle wedge (Chen and Clayton 2009). Lg waves show a significantly higher attenuation along the TMVB compare to the fore arc. In addition, Q tomography of the mantle wedge revealed a region of high attenuation in the northern part of the TMVB between 80 to $120\,km$ depth. High attenuation zones are common indicators of partial melts, and are well correlated with geological observations and resistivity profiles.

Jödicke et al. 2006 carried out a comprehensive study along two profiles perpendicular to trench. This study suggests several metamorphic reactions related to fluid released from the Cocos plate. Figure 2.8 shows mineralogical interpretation of one of these profiles based on the conductivity experiments and thermal models, areas of low conductivity and high attenuation are related to fluid release from the slab (Ogawa et al. 2001). For example, conductive zone 1 is located between $10 - 30km$ from the trench may be linked to shallow water release from subducting clays or zeolites. Eclogite transitions occur in conductive

zones 2 and 3 about 175 km and 215 km from the trench, respectively. Notice the gap in the dehydration of the slab in the flat portion of the slab. Zones 4 and 5 mark the beginning of the active front of the TMVB. Interestingly, an elongated conductive anomaly (denoted by Roman numerals: VI, VII) appears in the back arc of the TMVB and beyond indicating partial melts and possibly related to extinct volcanism.

As previously discussed in Section 2.3, volcanism is more active in the southern part of the TMVB suggesting a complex melt transport. Jödicke et al. 2006 proposed three possible mechanism: (1) fluids in a major shear zone, (2) fossil partial melt and associated metamorphic fluids, and (3) graphitic shear zones in the middle crust. Relative low temperatures in the corner of the mantle wedge can cause migrating of the volcanism as suggest by numerical simulations (Manea et al. 2005).

2.7 Conclusions

The Middle America region formed as a result of the collision between North and South America. In the Cretaceous, the Farallon plate formed the Sierra Madre Occidental, a large igneous province (LIP) characterized by several ignimbrite flare-ups that cover an extensive area of the present Northwest Mexico. From the Miocene to the present, collision of the Pacific ridge progressively fragmented the Farallon plate into several microplates and opened up the Gulf of California. This event lead to the formation of the TMVB, an oblique to the trench volcanic arc with a remarkable variety of volcanic products. Geochemical signature of the lavas range from the subduction to rift- like lavas. Attempts to develop a model for the formation of TMVB had resulted in an intense debate between groups with different geophysical evidence. On one hand, geochemical analysis of the lavas suggest a rift related process, but on the other hand imaging of the upper mantle indicates a possible tear and flattening of the slab. Additionally, recent discovery of non-volcanic tremor, slow slip events (SSE) and zones of low velocity on top of the slab have provided new elements to support

or rule out the proposed models.

Until now, former and present studies favor the hypothesis that water release significantly reduced the viscosity of the mantle wedge. In addition, detachment of the Farallon plate and tearing of the Cocos plate release a significant gravitational load inducing flattening of the slab. The MAR offers an intriguing geologic and tectonic scenario that challenges our present understanding of the processes that rule subduction around the world. In particular, scientists have focused their attention in mapping the geometry of the subducting slab to explain evolution of the tectonic history and geology of the region. The major questions to solve in this area are perhaps what caused the flattening of the slab and what are the implications for the geology and the seismic activity.

CHAPTER 3

Scattering of Teleseismic Body Waves by the Lateral Crustal Heterogeneity at the Pacific Trench of Mexico

3.1 Abstract

We examine the scattered field generated at the Pacific trench of Mexico upon the incidence of teleseismic body waves; and the waveguide properties associated with the structure of the subduction zone. In this study, we analyzed seismic records from a portable array perpendicular to the trench which show a distinctive phase with phase velocity of $3.5\,km/s$ following body wave phases. This signal is better observed following phases with high incident angles such as PS, SP and SS arriving from the ocean side of the trench, for events at teleseismic distances with magnitude larger than $M_w = 7.0$. Weak scattered signals were detected for events down to $M_w = 6.2$ and for direct P and S phases.

We found that the lateral transition between the dipping slab and continental crust, with an inclined boundary formed by the subducting slab at the trench, generates a strong discontinuity that scatters seismic waves generating a secondary field with amplitude comparable to the incident wave. This phase appears for incident body wave arrivals with characteristic wavelength comparable to the thickness of the continental crust. Analysis of the observed scattered field shows that the trapped waves are vertically polarized surface waves. Numerical modeling suggests that the impedance contrast at the trench and the geometry of the subducting slab form a waveguide-like structure that efficiently generates and transmits

trapped seismic waves along the continental margin.

3.2 Introduction

The Pacific trench of Mexico is a convergent plate boundary defined by the subduction of the Cocos plate beneath the North America plate. This is one of the ten areas around the world were flat subduction has been identified (Gutscher et al. 2000; Gutscher et al. 2000). A number of effects on wave propagation associated with this structure have been observed and examined by several authors. Shapiro et al. 1998 and Shapiro et al. 2000 recognized a scattered wave that propagates through the accretionary prism. Garcia et al. 2009 documented two modes of propagation: one along the coast, and the other perpendicular to the trench associated with the structure of the subduction zone. Furumura and Singh 2002 used numerical simulations to explore the waveguide properties of the subducting slab and its role in the propagation of guided waves.

The study area shows several important differences between a flat and a regular subduction zone. Some of these distinctive characteristics are the unusual geometry of the subducting zone and the irregular distribution of the seismicity (see e.g. Pardo and Suarez 1995; Pérez-Campos et al. 2008). The geometry of the slab can be separated into three sections: (1) the normal dipping section, from the trench to $\sim 80\,km$. (2) A flat section of the slab that extends $\tilde{8}0$ km from the trench to $250\,km$ inland just beneath the Moho, and (3) the steeply dipping section of the slab at $250\,km$. Coupling between the slab and the continental crust is stronger in the first $80\,km$ where most of the seismicity clusters. Beyond $250\,km$, the slab sinks aseismically into the mantle down to $550\,km$ as revealed by P-wave tomography (Husker and Davis 2009). The recent detection of an ultra slow velocity zone (Pérez-Campos et al. (2008); Song et al. 2009) in the interface between the flat section of the slab and the crust may also be an important factor for trapping guided waves in the first $250\,km$ from the trench, along with the high velocity of the underlying slab.

In recent years, several experiments around the world such as BOLIVAR (Guadez et al. 2006), TUCAN (Abers et al. 2007), VEOX (Pérez-Campos et al. 2008), and CASC93 (Rondenay et al. 2001) used temporary arrays to obtain images of the crust and upper mantle. However, in some cases the scattering and trapping of seismic waves by the subduction zone can strongly affect the interpretation of the results. For example, Morozov 2004, and Morozov and Zheng 2006 modeled scattering from the Cascadia trench zone and showed that it could potentially be interpreted as mode conversions on the subducting structures in receiver-function analysis. In order to identify converted body waves from the deep mantle, it is important to recognize body wave scattering due to structural contrasts between different tectonic units, which is examined here.

3.3 Data and Instrumentation

The Mesoamerican Seismic Experiment (MASE) consisted of a linear array of one hundred broadband seismic stations. The network extends approximately 550 kilometers perpendicular to the trench, from the city of Acapulco on the Pacific Coast of Mexico to the city of Tempoal $80km$ from the Gulf of Mexico, spacing between stations is $5-6\,km$ (see Fig. 3.1). Each station was instrumented with a broadband three-component Guralp CMG-3T seismometer, with a sampling rate of $100\,Hz$. The experiment was conducted for approximately two years from 2005-2007. In this study, we analyzed 26 teleseismic events with magnitudes larger than $M_w = 7.0$ recorded by the MASE array, shown in Figure 3.2. Table 3.1 lists those events that gave rise to a detectable scattered wavefield, all of them occurred in the southern hemisphere.

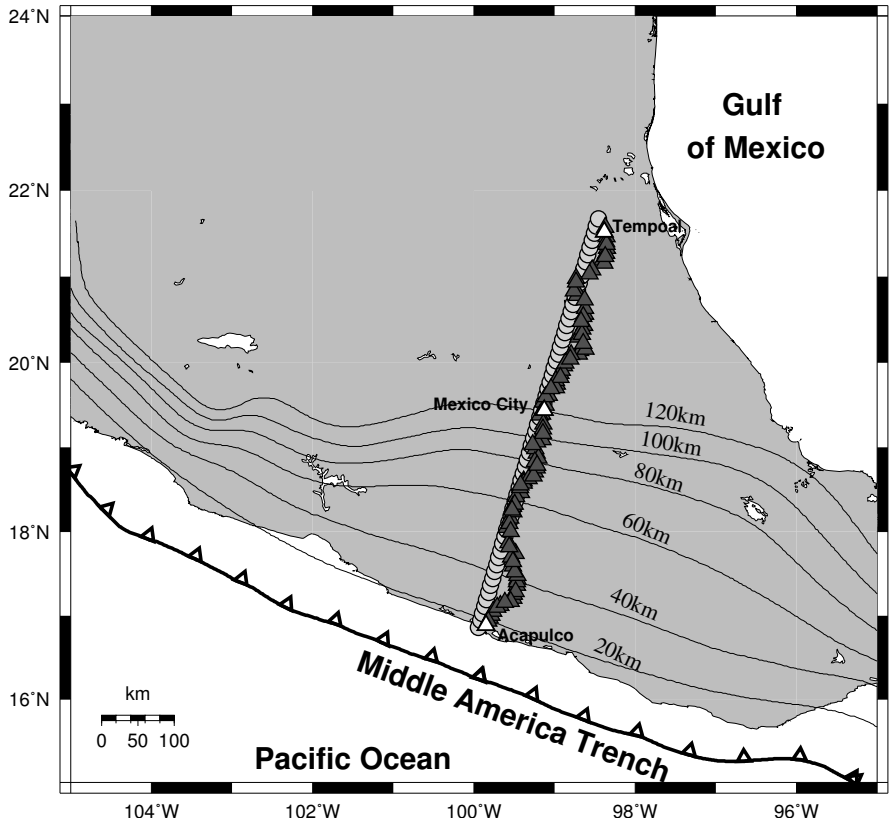

Figure 3.1: Station map of the MASE array. Slab isodepth contours by Pardo and Suárez (1995). Triangles show the location of the MASE stations, circles indicate the locations along the array for which we computed synthetic seismograms.

3.4 Scattered field analysis

We identified the scattered field by its relatively low apparent phase velocity as it moves across the array. In order to separate the scattered from incident waves, we computed a modified version of tau-p transform and *fk* diagrams for each event, and measured the slowness of the scattered field. Each seismogram was low-pass filtered with a Butterworth filter with corner frequency of $1\,Hz$ and then down sampled to 10 samples per second for faster processing. We compute a matrix representation of the data by linearly interpolating the retrieved seismograms onto a regular grid in space and time. The goal of interpolating

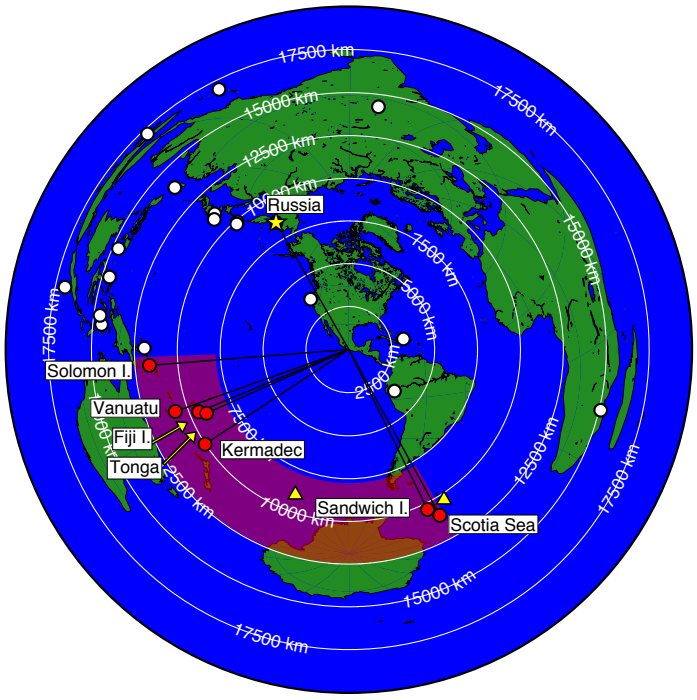

Figure 3.2: Events $M_w > 7.0$ recorded by the MASE network. Events marked with open circles do not show evidence of scattering. Solid circles indicate those events analyzed in this study that produced a measurable scattered field. (See Table 3.1 for more details).

the data is to create an image-like representation of the data and fill gaps in the array where data is missing either to malfunction of the station or excessive cultural noise. The resulting image enhances the visual detection of weak scattered signals that otherwise cannot be seen by direct visualization of the waveforms. The standard tau-p transform consists of slant stacking the seismograms along the line given by the equation,

$$T(x) = px + \tau(p). \tag{3.1}$$

Date	Region	Latitude	Longitude	Depth [km]	M_w	Distance [degrees]	Backazimuth [degrees]
2006/05/03	Tonga	-20.19	-174.12	55	8.0	81.76	245
2006/01/02	Fiji I.	-19.93	-178.18	582	7.2	85.24	247
2006/05/16	Kermadec I.	-31.81	-179.31	152	7.4	90.25	236
2006/07/17	Scotia Sea	-61.03	-34.37	13	7.0	93.54	153
2007/03/25	Vanuatu	-20.62	-169.36	34	7.1	96.58	250
2006/01/02	Sandwich I.	-60.96	-21.61	13	7.4	99.16	151
2007/04/01	Solomon I.	-8.47	157.04	24	8.1	104.95	262
2007/01/20	Scotia Sea*	-55.42	-29.53	10	6.2	93.27	147
2005/20/12	Pacific Ocean*	-57.38	-139.23	10	6.5	81.19	201

Table 3.1: List of events sorted by distance that generate scattered fields from the trench. Location of the events is shown in Figure 3.1. Last two rows are events with magnitude lower than 7.0 that show a weak scattered field.

Where $T(x)$ is the travel time, x is the epicentral distance, p is the horizontal slowness, and $\tau(p)$ is the time intercept at zero distance for a given slowness. We modified the standard tau-p transform by assuming that the x-axis is the distance from the trench (in this case the scattering source) to the station. p corresponds to the horizontal slowness in the direction of the array which roughly coincides with the direction of propagation of the scattered field. Thus, we slant stacked the seismograms in time windows of 25 seconds along sloping lines given by Eq. (1), and determine the root mean square value of the resulting average waveform for each set of parameters (p, τ). Figure 3.3 shows an example of the tau-p transform field for the Scotia Sea event. The section shows the SS phase arrival for the vertical component; the y axis is time from the event origin and the x-axis is distance to the trench. The scattered field is clearly observed branching off the main generating phase. The slowness of the scattered field observed in the tau-p domain is $0.29\,s/km$ ($3.45\,km/s$ apparent phase velocity), and the ratio of the incident stacked root mean square value of the scattered field to stacked root

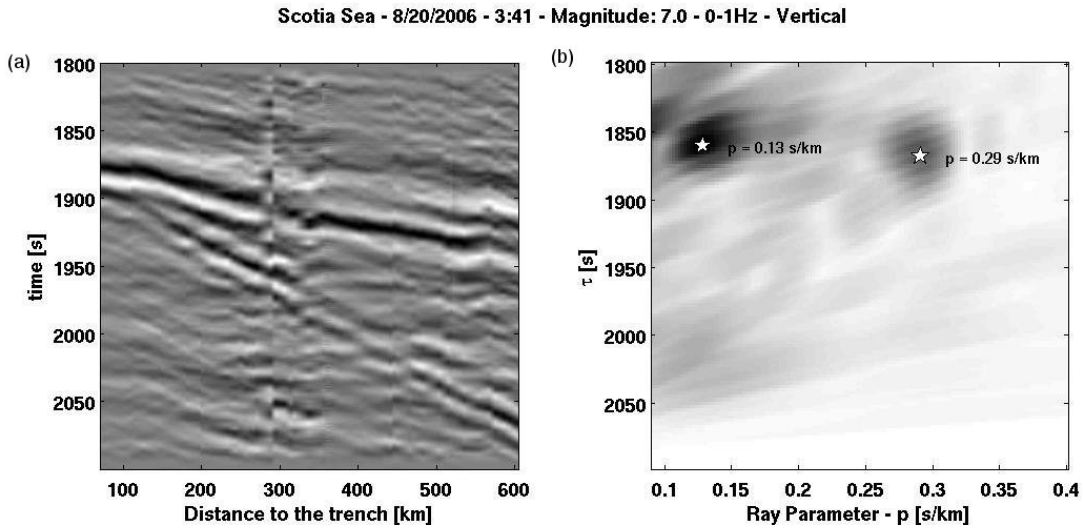

Figure 3.3: Tau-p transform for the Scotia Sea event. (a) shows an interpolated image obtained from the seismograms filtered between $0 - 1\,Hz$. (b) shows the tau-p field; stars indicate maxima in the field that corresponds to the arrival of the incident and scattered fields.

mean square value of the incident field is approximately 66%. A summary of the results obtained using the tau-p transform is shown in Table 3.2 for all events listed in Table 3.1.

Frequency-wavenumber spectra for three selected events (Tonga, Fiji and Vanuatu) and phases (SP, SS) are shown in Fig. 3.4, to demonstrate the differences in slowness between the scattered and incident field for different sources. Each subfigure corresponds to a $300s$ time window containing both incident and scattered fields. A significant amount of energy appears between the 3 and $4\,km/s$ iso-velocity lines regardless of the apparent velocity of the incident field, with a peak on the frequency axis around $0.05\,Hz$, i.e., a wave with a dominant $20\,s$ period, and characteristic wavelength of $\sim 70\,km$. The tau-p transform can efficiently be used to identify the scattered field along different parts of the record. A remarkable feature of this field is its strong amplitude compared to the amplitude of the generating field that can reach amplitudes of up to 68% of the incident field. The *f-k* analysis shows the presence

Event	Phase	p	Inc. Angle at 50 km	Phase	p	Inc. Angle at 50 km	Phase	p	Inc. Angle at 50 km	Phase	p	Inc. Angle at 50 km	Phase	p	Inc. Angle at 50 km
Tonga	*P*	5.26	18	PP	8.23	29	S	10.27	21	**SP**	12.39	47	**SS**	15	31
Fiji	P	4.80	16	PP	7.96	28	*S*	9.50	19	**SP**	11.87	44	**SS**	14	30
Kermadec	P	4.63	15	PP	7.92	28	*S*	9.10	18	**PS**	11.08	23	**SS**	14	30
Scotia Sea	P	4.59	15	PP	7.83	27	S	8.73	17	**PS**	11.04	23	**SS**	14	30
Vanuatu	P	4.50	15	PP	7.72	27	S	8.54	17	**PS**	10.91	22	**SS**	14	30
Sandwich	P$_d$*iff*	4.44	15	PP	7.62	27	S	8.33	16	**PS**	10.78	22	**SS**	14	29
Solomon	P$_d$*iff*	4.44	15	PP	7.42	26	$S_d iff$	8.32	16	**PS**	10.41	21	**SS**	14	28
Pac. Ocean	P	5.31	18	PP	7.84	28	*S*	10.36	21	SP	12.45	47	*SS*	14	30
Scotia Sea	P	4.59	16	PP	8.26	29	S	8.74	31	*PS*	11.04	22	SS	14	29

Table 3.2: List of the phases generating the scattered fields for the events shown in Table 3.1, p corresponds to the ray parameter in spherical coordinates. Phases in bold generate strong scattered fields; italics indicate a weak scattering signal; and normal font denotes no observable evidence of scattering. Approximate values of the angles of incidence are given based on the iasp91 model. Values of the ray parameter correspond to the closest station to the event.

Event - Inc. Phase	Slowness Inc. Field [s/km]	App. Vel. Inc. Field [km/s]	Slowness Scat. Field [s/km]	App. Vel. Scat. Field [km/s]	$\frac{\langle v^{Sc}\rangle_{rms}}{\langle v^{in}\rangle_{rms}}$[%]
Tonga - SP	0.10	8.83	0.27	3.57	44
Tonga - SS	0.11	8.83	0.26	3.81	21
Fiji - SP	0.06	15.87	0.27	3.72	23
Fiji - SS	0.10	19.98	0.26	3.86	60
Kermadec - PS	0.09	11.00	0.29	3.49	28
Kermadec - SS	0.13	7.63	0.27	3.66	68
Scotia Sea - PS	0.07	14.20	0.28	3.62	11
Scotia Sea - SS	0.13	7.77	0.29	3.43	66
Vanuatu - PS	0.05	19.04	0.27	3.65	22
Vanuatu - SS	0.10	9.80	0.26	3.81	47
Sandwich - PS	0.09	11.00	0.30	3.28	38
Sandwich - SS	0.09	11.00	0.28	3.51	37
Solomon - PS	0.09	11.00	0.30	3.28	53
Solomon - SS	0.09	11.00	0.24	4.17	44

Table 3.3: Apparent phase velocities for the scattered field obtained by using the τ-p Transform.

of two signals for which the apparent velocity of the scattered field is relatively independent of incident field. We used these methods to analyze records from all teleseismic events of magnitude larger than 7.0 recorded by the array. Figure 3.2 shows the map of all events examined in this study. We found that events that originated in the northern hemisphere do

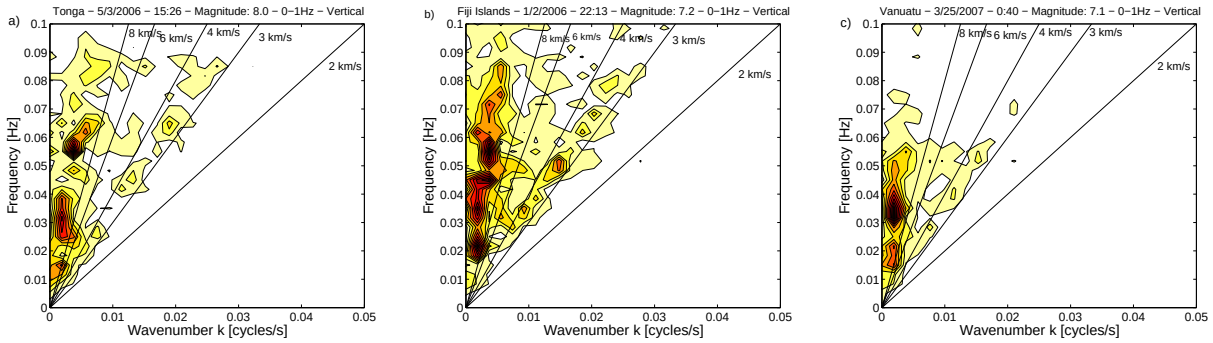

Figure 3.4: *fk* spectrum for the events analyzed showing the scattered signal with apparent velocity of $3 - 4\,km/s$.

not generate an observable scattered field; only events occurring in the southern hemisphere, marked with in solid circles, produce significant scattered fields from the trench. Triangles indicate the locations of two events with magnitude 6.2 and 6.5 that show a weak but still detectable scattered field. Table 3.3 indicates the incident angles and generating phases for the events that produced a detectable scattered field.

3.5 Propagation features

We investigate the origin and the propagation features of the scattered wavefield by generating families of synthetic seismograms using convolution of a reference waveform with a scattering series. We define a reference waveform as the section of the seismograms where the incident and the scattered field overlap. To obtain this waveform, we chose a time window from the closest station to the trench. For this station, we assume that the scattered field is in phase with the incident field, and they diverge towards the North due to the difference in slowness. Comparing each seismogram with a family of synthetic seismograms provides a better insight into the propagation characteristics and origin of the scattered fields. We convolve the reference waveform with a scattering series consisting of two pulses. The first

pulse marks the onset of the incident field (t_0) and has unitary amplitude while the second pulse has variable amplitude $-1 < A_2 < 1$ and marks a set possible onsets of the scattered field with time $t_n > t_0$. For each station, we generate a family of synthetic seismograms for different lag times and amplitudes, and then compare each synthetic waveform with the observed seismogram by computing the correlation coefficient. The set of parameters (A_2, t_n) that provides the largest correlation coefficient is selected for later analysis. Then the variation of t_n with distance is extrapolated to determine the zone where the incident and scattered fields branch off. Whereas the set of parameters A_2 indicates the relative amplitude ratio between these two fields, and the spatial decay of the scattered field as it propagates across the array. Figure 3.5 shows the results of convolution detection of the scattered field induced by the SS phase for the Scotia Sea event. Stars indicate the set of parameters t_n that provide the largest correlation coefficient, the box to the right shows the corresponding A_2 parameters. Open symbols are considered outliers; and consequently, they are not taken into account in the interpretation. Convolution analysis reveals two important features of the field. (1) Extrapolation of the onset times of the scattered and incident field shows a common merging point which coincides with the location of the trench. (2) The scattered field suffers little spatial decay suggesting a nearly constant geometrical spreading. This is consistent with the hypothesis that the trench acts as a linear source of the scattered field which is trapped in the crust.

3.6 Particle motion

We examine the particle motion by stacking separately the incident and the scattered field for events and phases with a high signal to noise ratio for the scattered field section. The seismograms were stacked by time shifting the records by the delay time obtained by dividing the distance to the trench by the phase velocity estimated through the tau-p transform. In order to avoid overlapping with the incident field, only records from the northern half of

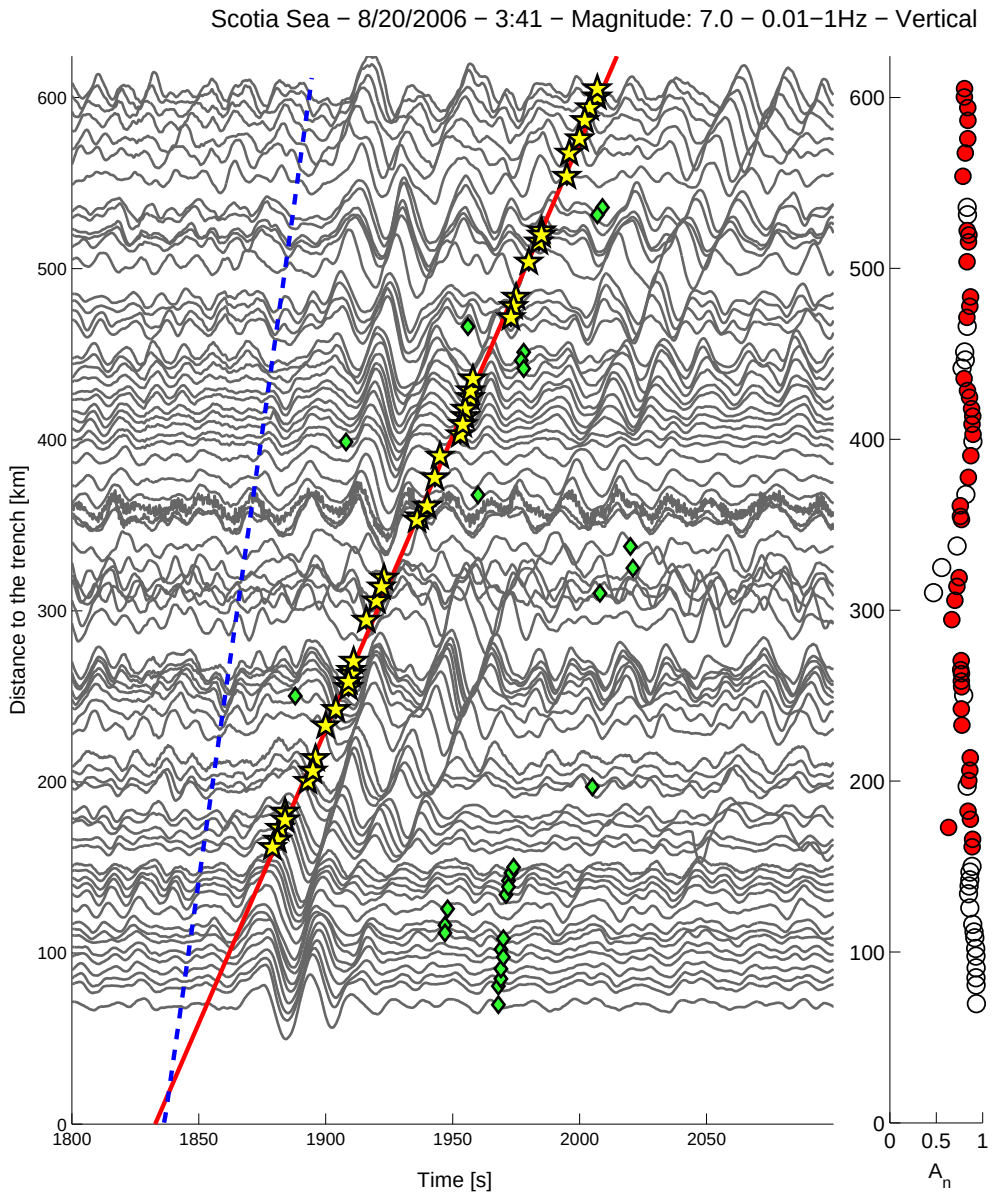

Figure 3.5: Cross-correlation detection of the scattered field and back projection of the incident and scattered field for the Scotia sea event. Dotted line shows the extrapolation of the incident field; solid line was obtained by fitting the points of maximum correlation coefficient for the scattered field. Diamonds are considered outliers and therefore not used for extrapolation. The right box shows the relative amplitude A_n of the scattered field with respect to the incident field that provided the largest correlation coefficient; outliers are shown by open circles.

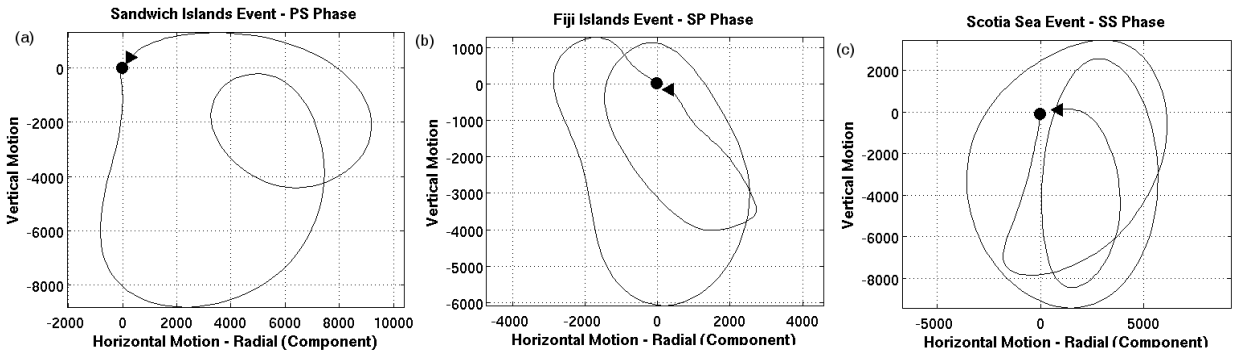

Figure 3.6: Particle motion. For three different events and phases: (a) Sandwich Island event, SP phase; (b) Fiji Islands, PS phase; and (c) the Scotia Sea event, SS phase that show a retrograde particle motion for the scattered field based on the stacking of seismograms.

the array are stacked. For large events, such as Solomon Islands ($M_w = 8.1$) and Tonga ($M_w = 8.0$), stacking is severely hindered by the long time source function of the incident field, which causes the incident field to overlap the scattered field at most of the stations. Fig. 3.6 shows the particle motion of the scattered field for three different events and three different generating phases. For all of these three cases, we observe retrograde particle motion of the scattered field consistent with the interpretation that the scattered field is composed of Rayleigh-type waves. In addition, apparent velocity of the scattered field measured by means of the tau-p transform is in the range of surface wave velocities with period between 20-30 seconds for central Mexico (Iglesias et al., 2010).

3.7 Modelling

Synthetic seismograms were computed for a two dimensional structure using the Indirect Boundary Element Method (IBEM), Sánchez-Sesma and Campillo (1991) and Sánchez-Sesma et al. (1993). We modified this method originally tailored to simulate the seismic response of alluvial valleys for incident P, S and Rayleigh waves to compute the response of

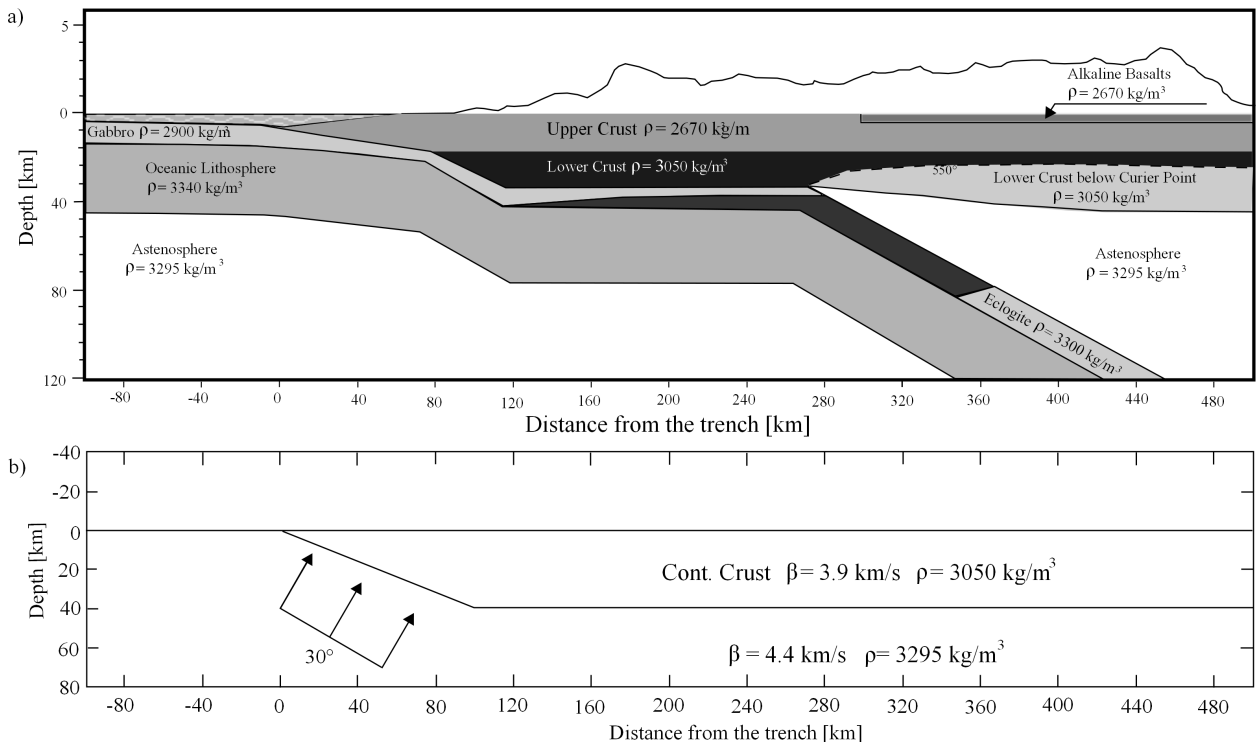

Figure 3.7: (a) Scheme of the subduction zone and model of density modified from Franco et al. (2005). (b) Simplified basin-like model based on this structure that was used to compute the synthetic seismograms shown in Fig. 3.8.

the larger-scale continental sized structure. The original code assumes that the size of the discontinuity and the characteristic wavelength of the incident field are comparable. This condition corresponds to the geometry analyzed here. We used a simplified model of the region based on the continental structure proposed by Franco et al. (2005) shown in Figure 3.7. The total length of the model is extended to 800 km in the North and left plane-layered to delay and minimize spurious reflections from the far end. For the continental crust, we assume a density of 2700 kg/m^3 and S- wave velocity of 3.2 km/s, with a constant thickness of 40 km. For the mantle, we consider a homogeneous half space with density of 3200 kg/m3 and S- wave velocity of 4.4 km/s. Locations of the computed seismograms are indicated in Figure 3.1 by solid circles located along a line through the MASE array. To simulate the

incident field, we used an SV plane wave at an incident angle of 30 degrees that generates the scattered field in the crust. Figure 3.8 shows a comparison between synthetic and real seismograms for the vertical and radial components for the Scotia Sea event, in which the SS phase excites the scattered field. In both real and synthetic seismograms, we observed that the scattered field is stronger in the vertical component with amplitude similar to the incident field, while in the horizontal component the incident field dominates the record. This simplified model generates surface waves similar to those observed at basin edges (see e.g. Anderson et al., 1986; Kawase, 1996). Basins are well known for their capacity of trapping energy from distant sources; the observations presented here show an analogous case of a scaled basin simulating a waveguide. Velocity of propagation in the continental crust is lower than the surrounding medium which is analogous to alluvial valleys in solid rock; this is also a required condition for the waveguide effect proposed here. Unlike basins, the structure proposed here is open at one end. This condition was imposed due to the fact that records do not show a back reflected waves from the other coast. This suggests that the scattered field dissipates as it moves away towards the Gulf of Mexico.

3.8 Interpretation and discussion

In general, we observe that the scattered field is a strong signal superimposed on the incident body phases caused by the structural contrast between the continental and oceanic units. When body wave phases reach the trench from the ocean side, scattering and trapping into the crust generates guided surface waves. This phase was observed after body wave phases coming from events with backazimuth between $150 - 250^{\circ}$ at teleseismic distances between 70 to 112 degrees. The scattered field appears following most body wave phases, but it is better seen after the PS, SP and SS phases. These phases have higher incident angles than phases such as P, S which produce weaker scattered signals that are difficult to detect. The PP phase is clearly observed and arrives at about the right incident angle

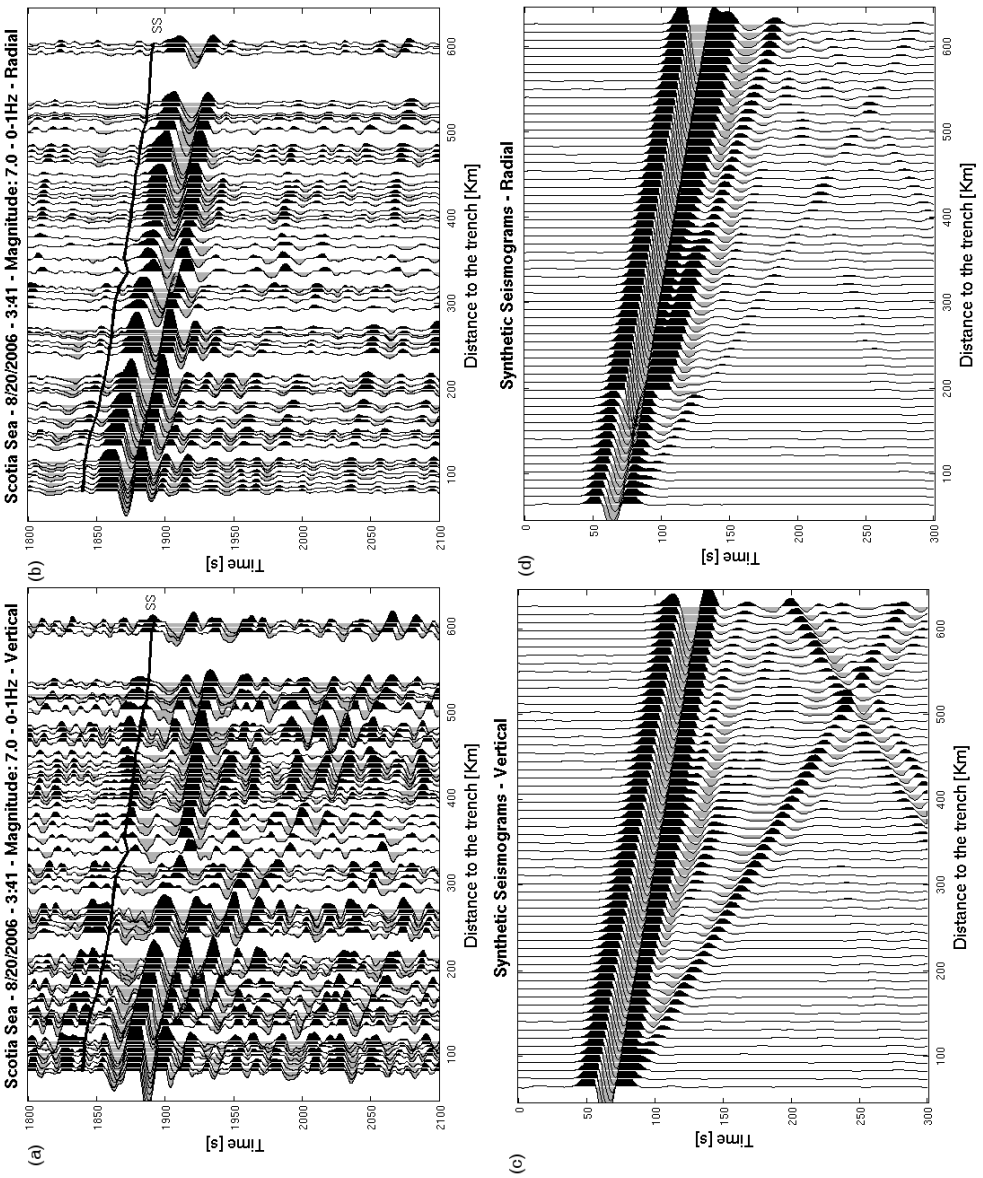

Figure 3.8: Synthetic seismograms computed for comparison with the Scotia Sea event. (a) and (b) show the real seismograms retrieved from the MASE array, in the vertical (a,c) and horizontal components (b,d). The solid line shows the time of arrival of the generating phase, in this case SS phase. (c) and (d) show synthetic seismograms obtained using the IBEM method.

and azimuth for the events analyzed. But, it has low amplitude and high frequency content, characteristics which do not favour the generation of the scattered field. Another factor influencing the excitation of scattered waves from the trench is the ratio between the vertical scale length of the continental structure and the characteristic wavelength of the incident field. The body phases from the teleseismic events had characteristic wavelengths $\lambda = 60 - 80\,km.$. If we assume that the thickness of the crust $L =\sim 40km$ is the characteristic scale for this structure, the ratio between the characteristic wavelength (λ) and the size of the propagation discontinuity suggests that Mie scattering (Wu, 1989) is the dominant regime for the generation of the scattered field. In this regime, scattering occurs mostly in the forward direction with weak frequency dependence, in agreement with both observations and numerical models. Numerical modeling of the scattered field suggests two major physical conditions of the medium for the generation of this field. First, the lateral variation caused by the transition from oceanic to continental crust. Both observations and numerical models show that the origin of the scattered field occurs at the trench which marks the beginning of the subduction zone. Second, the thickness of the continental crust is relatively constant ($\sim 40km$) along the trajectory of the scattered field, and overlays the flat-subduction slab which favours the propagation of the scattered field as a trapped surface wave. It is important to note that the tectonic model used to generate the synthetic seismogram does not fully reproduce the tectonic conditions along the array. However, it successfully reproduces the major features of the scattered field and provides an insight into the factors that give rise to this field. By using the MASE array, we were able to track the scattered field for a distance of approximately $\sim 550km$. For this range, we did not observed a significant dispersion of the scattered field which travels a distance of approximately 7 times its characteristic wavelength. In addition, the waveform propagates with very little distortion along the array independently as it passes through different geological provinces. This result is expected given that the trench acts as a semi-linear source when excited by a plane incident body wave and that the continental crust produces a waveguide effect.

Our analysis included all earthquakes with $M_w > 7.0$, and two events with smaller magnitude in the Pacific Ocean (6.5) and the Scotia Sea (6.2) (See Fig. 3.2 and Table 3.1). These events satisfy two necessary conditions for the excitation of the trench as shown in our analysis: (1) They produce body phases with high incidence angle which can only be achieved by events at teleseismic distance and (2) they radiate significant low frequency seismic waves in the range $0 - 1Hz$. Smaller events occurred along the Pacific-Nazca ridge, which should in theory produce a similar scattered field. However, these events are usually shallow with low magnitude and shorter wavelengths. These characteristics do not to favour the generation of a detectable scattered field despite of the fact that they produce direct phases with an adequate incident angle.

3.9 Conclusions

We identified scattered surface waves generated by long-period teleseismic body waves incident on the impedance contrast at the subduction zone of Mexico. The scattered surface wave field could be analyzed because of the availability of data from a 100 station broadband array that showed spatially coherent moveout perpendicular to the trench. Tau-p diagrams and the f-k analysis showed that the slowness of the scattered field is independent of the relative location of the sources. Calculation of synthetic seismograms support the interpretation that a significant body-surface wave scattered field is generated under the following conditions.

1. The incident body waves arrive from the ocean side of the trench. No observable scattered field was detected for events with similar magnitude and distance to the array that were incident from the opposite side.

2. The wavelength of the incident field is comparable with the thickness of ocean-continent impedance contrast.

3. The geometry of the crust and subduction zone forms a waveguide structure. The MASE array lies on top of flat subduction zone. Such scattered phases are expected to be observed in other areas of the world with a similar geometry.

CHAPTER 4

Scattering of seismic waves in heterogenous media

4.1 Introduction

The Earth is composed of a very diverse mixture of rocks and minerals with different elastic properties. As minerals travel from the lower mantle to the surface and back, they experience a vary drastic change in the pressure and temperature conditions as well as surrounding elements. This diversity gives rise to a complex structure for propagation of seismic waves. In addition, the crust is highly affected by interaction with the atmosphere which causes erosion, weathering, and fracturing of the rock. As a consequence, seismic waves traveling through the lithosphere and specially in crust suffer from several degradation mechanism in their amplitudes and trajectories as they move apart from the source.

High frequency seismograms show a train of energy that follows each seismic phase. This signal known as coda is the result of the redistribution of energy by heterogeneities in the medium. Coda appears as continuous incoherent series of waves in the tail portion of the seismogram as a result of random fluctuations in the properties of the medium. Therefore, interpretation can only be achieved in a statistical way using stochastic models of the crust. Despite their random origin, coda waves have been successfully used to retrieve earthquake features such as magnitude, stress drop and relative location (Mayeda and Walter 1996; Suteau and Whitcomb 1979; Robinson et al. 2011); as well as Green's functions (Snieder 2004) and attenuation of the medium (Abubakirov and Gusev 1990, Margerin et al. 1999). Modeling of coda waves cannot be achieved in a deterministic way by means of the wave

equation given the complex composition of the lithosphere. Consequently, several empirical approaches have been developed to obtain a statistical description of coda.

4.2 Classical Models of Scattering

Pioneering work by Aki 1969, first recognized that coda is the result of scattering due to the random distribution of heterogeneities in the crust. In a later work, Aki and Chouet 1975 developed a theoretical model of single scattering that fit well the observed decay of coda energy using the Born approximation. Rautian and Khalturin 1978 recognized that early proportion of the coda is different at nearby stations, but they have common envelope for twice the time of the arrival of the S-wave for band-pass seismograms. Single scattering models assume that the mean free path is greater than the travel distance between the scattered and the receiver, this result lead to the development of multiple scattering models based on the analogous physical phenomena. Dainty and Toksoz 1981 proposed an extreme model of scattering using the diffusion equation, this model explains the slow decay observed in lunar records of impacts. Frankel and Clayton 1986 introduced an energy-flux model to explain the coda decay in 2D finite-difference simulations. Wu and Aki 1985; Zeng 1993 developed a model based on the radiative transfer theory that accounts for both intrinsic and scattering attenuation.

Attenuation of seismic waves is usually attributed to three major mechanisms: geometrical spreading, intrinsic attenuation and scattering attenuation. Geometrical spreading is caused by the waveform expansion as it propagates away from the source, it depends on the geometry of the medium of propagation and the travel distance r. If we assume that the source is a point source in an homogenous 3D space, waves propagate as spherical waveforms as they move away from the source with an energy decay proportional to r^{-2}. Another extreme case occurs for wave propagating in a 2D medium and for line sources, in this case the energy decay is proportional r^{-1}. Geometrical spreading is commonly assumed in most of

the models of propagation and does not depend on the physical properties of the medium. Validity of this assumption is discussed in the next section. The second component of attenuation is related to the properties of the medium and is commonly determined by an adimensional quantity called quality factor, Q. Knopoff 1964 define Q as the energy lost per cycle of oscillation. Aki 1980a proposed the following relationship to separate the different components of attenuation

$$\frac{1}{Q_t} = \frac{1}{Q_I} + \frac{1}{Q_{Sc}}. \tag{4.1}$$

Where Q_t is the total attenuation, Q_I is the intrinsic attenuation and Q_{Sc} corresponds to the attenuation due to redistribution of energy or scattering. Intrinsic attenuation accounts for the effects of the anelastic properties of the Earth that cause lost of energy through conversion of energy into heat (Jackson and Anderson 1970; Dziewonski 1979). Conversely, scattering attenuation, Q_{Sc}, does not remove energy from the overall wavefield, it is interpreted as redistribution of energy due to the heterogeneities in the medium. Some authors have attempted to quantify which of these two components have a larger influence on the total attenuation (Jacobson 1987; Frankel and Wennerberg 1987; Fehler et al. 1992).

Frankel and Wennerberg 1987 introduce an energy-flux model to determine independently the components of Q_t. Using finite differences simulations in a 2D medium, they observed that the the coda energy is mostly contained in a spherical volume behind the direct waveform. For a medium with no intrinsic attenuation, they showed that the amplitude of the coda envelope A_c follows the equation

$$Ac = d\left(\frac{3E_T}{4\pi}\right)^{-1/2}(vt)^{-3/2}\sqrt{1-\exp\frac{-\omega t}{2Q_S}}. \tag{4.2}$$

Where E_T is the elastic energy in the medium, d is the distance to the source, and v the shear wave velocity. This model predicts that the energy decay per unit volume is proportional to $t^{-3/2}$. Eq. (4.2) can be expanded to account for the effect of intrinsic attenuation by expressing the elastic energy as $E_T = E_0 e^{-\omega t/Q_I}$. Where E_0 is the elastic energy radiated by

the earthquake. Therefore, Eq. (4.2) can be rewritten as

$$Ac = d\left(\frac{3E_0}{4\pi}\right)^{-1/2}(vt)^{-3/2}\exp-\frac{\omega t}{2Q_I}\sqrt{1-\exp\frac{-\omega t}{2Q_S}}. \tag{4.3}$$

Seismic waves can travel either as P- or S- waves. Each time a seismic wave encounters a discontinuity in the medium, it generates new P- and S- scattered waves. Although S- to P- conversions are usually small as demonstrated by Aki 1980b, S- to S- conversion and P- to S- can build up a significant proportion of the scattered field. In addition, these models ignore the polarization and isotropic scattering is usually assumed. Sato 1994 and Margerin et al. 2000 improved existing models based on the transfer theory by including a more realistic radiation pattern for the scattered waves.

Another approach for modeling single scattering is based on the energy flux model. We can obtain simple expressions by assuming that J_0 is the energy-flux density of the incident wave, and J_1 the scattered energy flux due to a heterogeneity in the medium at a distance r from the source. Thus, the scattering potential of the medium is characterized by the ratio $d\sigma/d\Omega$. Where $d\sigma$ is the differential cross-section of the scatterer and $d\Omega$ is the solid angle element. Then, we can define the ratio between the incident and scattered energies as

$$\frac{d\sigma}{d\Omega} = \frac{J_1 r^2}{J_0}. \tag{4.4}$$

Then, for a volume filled with n scatters, the scattering coefficient is the product of the number density n times the differential scattering cross-section

$$g \equiv 4\pi n\frac{d\sigma}{d\Omega}. \tag{4.5}$$

Integration over all direction provides the total scattering coefficient g_0 that has dimensions of reciprocal length

$$g_0 = \frac{1}{4\pi}\oint g d\Omega = n\oint\frac{d\sigma}{d\Omega}d\Omega = n\sigma_0 = \ell^{-1} = {}^{Sc}Q^{-1}k. \tag{4.6}$$

Where ℓ is the mean free path and k is the wave number. Q is therefore a parameter that is distinctive of the local geological conditions, and its value can vary as much as one order

of magnitude. Herraiz and Espinosa 1987; Campillo et al. 1998; Fehler and Sato 2003; Romanowicz and Mitchell 2008 are good reviews of this topic.

4.3 Born Approximation

The Born approximation is widely used to model scattered fields in weakly heterogenous media. It is based on the assumption that the amplitude of the perturbed field is much smaller than the wavefield that induces it. Notice that this hypothesis violates the principle of conservation of energy, extra energy is added to generate the scattered field. Thus, the total wavefield field $\mathbf{u}$ can be written as

$$\mathbf{u} = \mathbf{u}^0 + \mathbf{u}^1. \tag{4.7}$$

Where $\mathbf{u^0}$ is the wavefield in the absence of heterogeneities, and $\mathbf{u}^1$ is the scattered field. Additionally, seismic wave velocity of the medium can be decomposed into two components: V_0 the mean velocity of the medium and the perturbed velocity δV.. Thus,

$$V(\mathbf{x}) = V_0 + \delta V(\mathbf{x}) = V_0[1 + \mu(\mathbf{x})]. \tag{4.8}$$

Where $\mu(\mathbf{x})$ is the fractional fluctuation of the velocity in the medium. We assume that $\langle V(\mathbf{x})\rangle = V_0$, and $|\mu| \ll 1$. By assuming that the randomness of the medium is homogenous, we define the autocorrelation function (ACF) as an ensemble average

$$R(\mathbf{x}) = \langle \mu(\mathbf{x})\mu(\mathbf{x}+\mathbf{x}')\rangle = \epsilon^2 N(r). \tag{4.9}$$

The ACF is a statistical measure of the magnitude and spatial scale of the irregularities in the medium. Common realizations of the ACF are the Gaussian $N_g(r) = e^{-r^2/a^2}$, and the exponential $N_e(r) = e^{-r/a}$ distributions. Where a is the measure of the length scale of the heterogeneity known as correlation distance.

Fourier transform of the ACF is called power spectral density function (PSDF). For a Gaus-

sian medium the PSDF is

$$P(k) = \int_{\infty}^{\infty} \epsilon^2 N(\mathbf{x}) e^{-i\mathbf{x}k} d\mathbf{x} = \epsilon^2 \sqrt{\pi^3} a^3 e^{-k^2 a^2/4} \tag{4.10}$$

whereas for the exponential case,

$$\begin{aligned} P(k) &= \frac{8\pi\epsilon^2 a^3}{(1+a^2k^2)^2} \\ &\propto (ak)^{-4} \text{ for } ak \gg 1. \end{aligned} \tag{4.11}$$

Let us consider a wave propagating in an homogenous space that encounters a cubical anomaly of side L. Aki and Richards 1980 (page. 472) showed that the loss of energy due to a cubic heterogeneity is

$$g_\pi = \frac{\Delta E}{E} = \frac{8\epsilon^2 k^4 a^3 L}{1+4k^2a^2}. \tag{4.12}$$

Where ϵ is the mean fluctuation of the medium. Figure 4.1 shows the change in the backscattering coefficient g_π as a function of the product ka. If a is constant, the loss of energy is proportional to k^4 for small wavenumber k and is constant for large wavenumbers. Note that the Mie scattering regime marks the transition between the infinite frequency approximation and the Rayleigh regime.

4.4 Validity of the models of scattering

Complete characterization of the scattered wavefield remains as an extremely challenging problem. Classic models of scattering have only solved this problem partially. Several authors have pointed out some of the major ambiguities and over-assumptions of these models. Padhy 2005 analyzed several published studies of attenuation, he highlighted the need for improved models of scattering with depth dependent distribution of scatters. Borehole studies in California explored the dependence of Q in boreholes and compare the attenuation with surface stations. Abercrombie 1997 computed the spectral ratios for Q_p and Q_s in

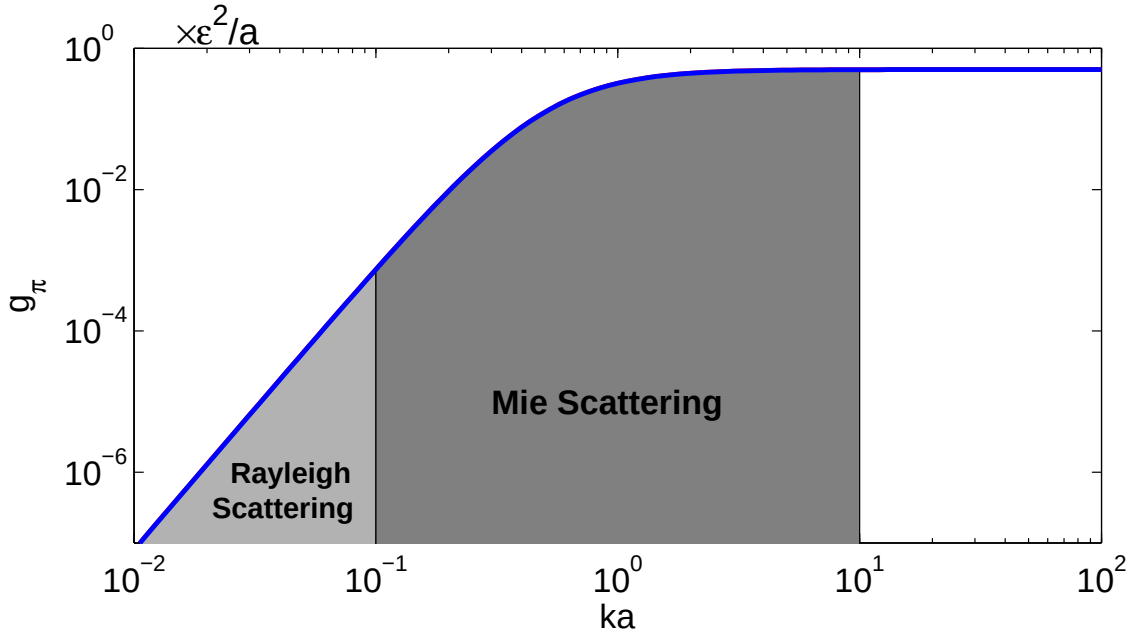

Figure 4.1: Backscattering coefficient g_π as a function of the wavenumber and the characteristic scale of the heterogeneity ka. In the Rayleigh scattering regime, the scattering coefficient is proportional to k^4.

Cajon Pass borehole and a nearby surface station. She found that 90% of the attenuation occurs in the upper 3km. In another study along the San Andreas fault in Parkfield, Abercrombie 2000 demonstrated that the northeast side of the fault has almost twice attenuation compare with the southwest side. Davis and Clayton 2007 investigated the hypothesis that scattering concentrates in the upper layers due to greater impedance contrast caused by either sedimentary or metamorphic layering in the upper few kilometers. They hypothesized that coda decay can be described by a frequency-dependent scattering Q_{Sc} and a frequency-independent intrinsic attenuation Q_I.

Recent papers by Morozov 2008; Morozov 2009 have prompted an intense debate (Xie and Fehler 2009; Xie 2010; Li and Lu 2010) about the interpretation of the quality factor Q and the frequency dependance of the geometrical spreading. Morozov questions the common

formulation of the quality factor as a frequency dependent power law,

$$Q(f) = Q_0 \left(\frac{f}{f_0} \right)^{\eta}. \tag{4.13}$$

Where Q_0 is the attenuation at frequency f_0 usually $1Hz$ and η is a number that describes the frequency dependance of Q. By assuming that the effects of the source and the receiver have been removed, the path factor can be written as

$$P(f,t) = G_0(t) e^{-\frac{\pi f t}{Q(f)}}. \tag{4.14}$$

$G_0(t)$ is the geometrical spreading factor. If $\eta \approx 1$ in Eq. (4.13), which is commonly reported in the literature. Substitution of $Q(f)$ in Eq. (4.14) eliminates the frequency dependance from $P(f,t)$. Another interesting observation lies on the additive nature of Q as suggested by Aki 1980b (Eq. (4.1)). Despite of the fact that intrinsic and scattering attenuation have completely different physical origin, the contribution to the total attenuation is often added. Laboratory experiments (Jackson 2000) suggest that for shallow depths ($< 100km$), intrinsic attenuation is approximately frequency independent while scattering attenuation is strongly frequency dependent. These results lead Morozov to propose a new formulation of attenuation that accounts for changes in geometrical spreading due to the structure of the earth and a frequency independent quality factor Q. By solving for the nominator in Eq. (4.14), the new model states that

$$\alpha(f) = -\frac{d}{dt} ln \left[\frac{P(f,t)}{G_0(t)} \right] = \gamma + \frac{\pi f}{Q_e}. \tag{4.15}$$

Eq. (4.15) corresponds to line whose intercept γ determines the correction factor to the geometrical spreading. The second term defines the quality factor Q_e that correspond to the effective attenuation caused by the medium itself. This set of parameters has arguably a better correlation with the tectonic setting as shown in Figure 4.2.

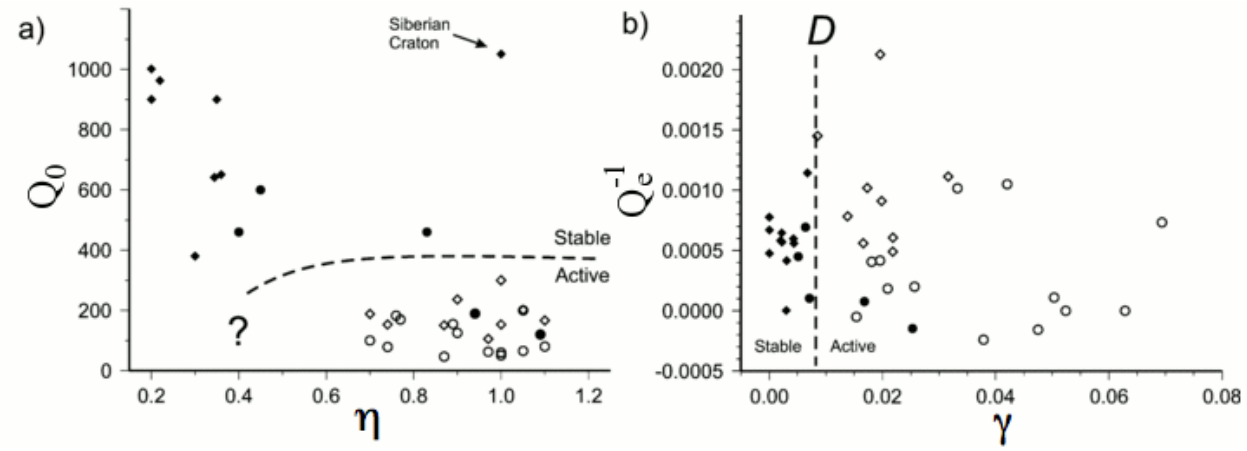

Figure 4.2: Comparison between the traditional formulation $Q(f) = Q_0(f/f_0)^\eta$ and the new model of attenuation $\alpha(f) = \gamma + \pi f/Q_e$. The dotted line indicates the separation between active and passive regions. Modified from Morozov 2008.

4.5 Coda Normalization Method

The coda normalization method removes the effect of either the source, the path or the site effects from the seismograms. Source radiation refers to analysis of the rupture that induces the seismic wavefield, it provides information about the focal mechanism (Choy and Boatwright 1995), size of the earthquake (Kanamori et al. 1993), and rupture propagation (Ishii et al. 2005). Site effects studies focus their attention in the analysis of the risk zones due to the near to the surface geological conditions. Studies of site effects include amplification of seismic waves due to reverberation in sedimentary basins (Singh and Pardo 1993) and focusing effects due to the geometry of the underlying layers (Davis et al. 2000). Path effects studies deal with the properties of the medium between the source (earthquake) and the receiver (seismometer). The coda normalization method eliminates the contribution of the site and source amplification/attenuation from the seismograms. It is based on the principle that energy is evenly distributed in a volume surrounding the station at a given fixed lapse time. This is a purely empirical conclusion and is not supported by any theoretical

model of wave propagation.

Envelope amplitudes vary with the distance to station and size of the event. Figure 4.3 shows the envelopes and locations of 58 events with different magnitudes recorded by the station MAXE. Hypocentral distances are constrained to a narrow range between $126\,km$ and $138\,km$ and magnitudes varies from $3.2 \leq M_w \leq 5.0$. The amplitudes of the envelopes are normalized by the mean coda amplitude at $45\,s$ as indicated by the arrow.

We can express the power of coda as the product of the source, propagation and site effects as (Sato and Fehler 2009, pp. 70),

$$\langle |\dot{u}_i^{coda} j(t;f)^2| \rangle \propto W_i^S(f) |N_j^S(f)|^2 \frac{\exp\left(-Q_c^{-1} 2\pi f t\right)}{t^n}. \tag{4.16}$$

Where $\dot{u}_i^{coda} j(t;f)^2$ is the coda wavefield recorded at twice the lapse time at the receiver j and source i; f is the central frequency at which the seismograms are filtered. $W_i^S(f)$ is the source radiation factor and $N_j^S(f)$ accounts for the site effects. The exponential term n is $(1, 2)$ depending on whether the dominant scattered wavefield is mostly made of surface, diffusive or body waves.

4.6 Multiple Lapse Time Window Method

The Multiple Lapse Time Window Method (MLTW) method was originally proposed by Hoshiba et al. 1991 to separate the contribution of intrinsic and scattering attenuation. It is based on the radiative transfer theory approach introduced by Wu and Aki 1985 and Zeng 1993. This method has been applied in numerous regions around the world such as central California, Long Valley, and Hawaii (Mayeda et al. 1992); Kanto-Tokai region Japan (Fehler et al. 1992); northern Chile (Hoshiba et al. 2001); West Greece (Tselentis 1998);South Korea (Chung et al. 2010); southern California (Jin et al. 1994); Cajon Pass, California (Adams and Abercrombie 1998); Turkey (Akinci and Eyidoğan 2000); Italy (Bianco et al. 2005); central Andes (Badi et al. 2009); Spain (Akinici et al. 1995); Canada (Feustel et al. 1996)

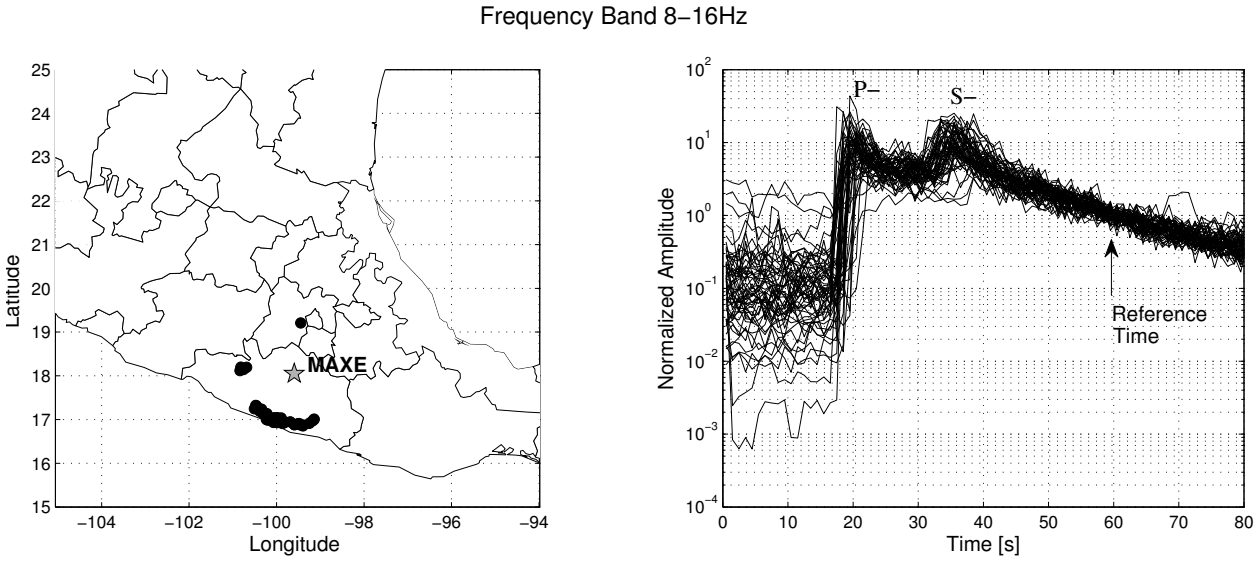

Figure 4.3: Coda normalization for the source. (left) Shows the location of 58 events at epicentral distances between $126\,km$ and $138\,km$ recorded by the MAXE station. (right) Envelopes of the seismograms filtered between $8-16\,Hz$, the arrow shows the time at what the coda energy is computed for normalization.

among other studies. This method consists basically in comparing the energy contained in three consecutive time windows $0-15s$, $15-30s$ and $30-45s$ after the S- wave arrival. The following assumption are made in order to compute synthetic energy envelopes:

i) A medium with uniform density n_0 of point-like scatters with effective cross-section σ_0 is assumed.

ii) Waves are considered incoherent.

iii) Scattering is isotropic.

iv) S waves radiate from a point source with a spherical geometrical spreading.

v) There is not conversion between S- wave and P- waves.

vi) There is no loss due to intrinsic absorption.

vii) The medium is considered to be infinite with constant velocity v.

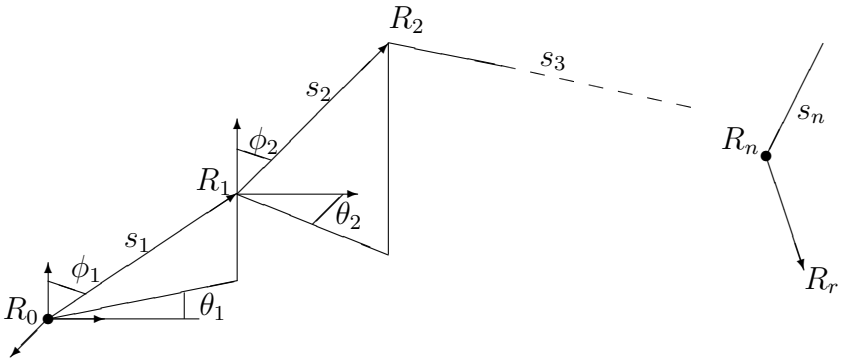

Figure 4.4: Schematic description of the variables used to generate the synthetic energy envelopes. $\mathbf{R}_0$ is the location of the source and the $\mathbf{R_n}$ location of the receiver. s_k, θ_k and ϕ_k are random variables in the ranges $[0, \infty)$, $[0, 2\pi]$ and $[0, \pi]$.

Synthetic energy curves are computed by shooting W_0 particles isotropically from the source located at $\mathbf{R}_0$, to the receivers located at $\mathbf{R_r}$ being the points $\mathbf{R_n}$ the location of the scatter points as shown schematically in Fig. 4.4. Each particle moves a distance s_k with a take off angle θ_k and azimuthal orientation ϕ_k. The subscript k denotes the order of scattering. Thus, s_k is a random variable with Poisson distribution and mean $\lambda = \ell \equiv g^{-1}$ (See Eq. (4.6)), and θ_k and ϕ_k are mutually independent random variables in the ranges $[0, 2\pi]$ and $[0, \pi]$, respectively. The position of each scatter point in 3D cartesian space is,

$$[\Delta x, \Delta y, \Delta z] = [s_k \sin(\phi_k)\cos(\theta_k), s_k \sin(\phi_k)\cos(\theta_k), s_k \cos(\phi_k)]. \tag{4.17}$$

To guarantee that the scattering vector $\mathbf{r}_k$ is evenly distributed on the surface of the sphere for each scattered point. The functions $\cos(\phi_k)$ and $\sin(\phi_k)$ are evaluated in the following

way,

$$\theta_k = 2\pi U_1, \tag{4.18}$$

$$\cos(\phi_k) = 2U_2 - 1, \tag{4.19}$$

$$\sin(\phi_k) = \sqrt{1 - \cos(\phi_k)}. \tag{4.20}$$

Where U_1 and U_2 are evenly distributed random variables in the range $[0, 1]$. Each particle contributes to the total energy at any given scatterer point $\mathbf{R}_n$. Therefore, the total S-wave energy arriving at the receiver $\mathbf{R}_r$ is the sum of the probability that each particle has of crossing a unit area around the receiver perpendicular to the vector $\mathbf{R}_r - \mathbf{R}_n$. This probability is expressed as,

$$\begin{aligned} &P(s \geq |\mathbf{R}_r - \mathbf{R}_n|, \theta_0 \leq \theta \leq \theta_0 + \Delta\theta, \phi_0 \leq \phi \leq \phi_0 + \Delta\phi) \\ &= \frac{\Delta\theta}{2\pi}\frac{\sin\phi}{2}\delta\phi(1 - (1 - \exp(-g|\mathbf{R}_r - \mathbf{R}_n|))) \\ &= \frac{1}{4\pi|\mathbf{R}_r - \mathbf{R}_n|^2}\exp(-g|\mathbf{R}_r - \mathbf{R}_n|), \end{aligned} \tag{4.21}$$

since

$$1 = |\mathbf{R}_r - \mathbf{R}_n|^2 \sin\phi\Delta\theta\Delta\phi = \text{unit area}.$$

Notice that Equation (4.21) leads to probabilities larger than one for small values of $|\mathbf{R}_r - \mathbf{R}_n|$. In the limit, when $|\mathbf{R}_r - \mathbf{R}_n|$ becomes smaller than $\sqrt{1/4\pi}$, the probability function converges to $P(s, \theta, \phi) = 0.5$. As the particle approaches the receiver, the exponential becomes $\exp(-g|\mathbf{R}_r - \mathbf{R}_n|) \to 1$. Therefore the particle can only move either in any direction to the receiver or away from it with equal probability. So as $\Delta r \to 0$, integrating the differential form of expression of Eq. (4.21)

$$dP = \frac{d\theta}{2\pi}\frac{\sin\phi}{2}d\phi\exp(-g\Delta r), \tag{4.22}$$

thus,

$$P = \frac{\Delta\theta}{2\pi}\frac{\cos\phi_2 - \cos\phi_1}{2}\exp(-g\Delta r). \tag{4.23}$$

In the limit $\Delta r \to 0$,

$$P = \frac{\Delta\theta}{2\pi}\frac{\cos(0) - \cos(\pi)}{2} = \frac{1}{2} \tag{4.24}$$

The sum of all segments s_k gives the total travel distance of the mth particle

$$D_m = s_1 + s_2 + s_3 + \ldots + |\mathbf{R}_r - \mathbf{R}_n|. \tag{4.25}$$

The travel time is obtained by simply dividing total distance by the velocity of the medium as $t_k = D/v$. The probabilities obtained using Eq. (4.21) at any given time t_k are summed up into time intervals $[t, t + \Delta t)$ to generate the energy density curve for a large enough number of particles. We assume that each particle has unit energy and that the total energy radiated by the source is equal to W_0. This formulation guarantees that the total energy in the system is conserved. We can separate the total energy into two components: the direct energy $E_d(r, t)$, and the scattered energy $E_s(r, t)$. At any distance r, addition of these two terms over the lapse time is equal to W_0.

$$W_0 = W_0 e^{-gtv} + \int_0^t 4\pi r^2 E(r, t) dr. \tag{4.26}$$

The first terms is the contribution of the direct energy decreased by the scattering coefficient g at time t, whereas the second term accounts for scattering energy contained in the volume delimited by the wavefront. Figure 4.5 shows the numerical evaluation of the Eq. (4.26) for a medium with S- wave locity of $v = 3.5\,km/s$; and a source of 5×10^5 particles; for two different scattering coefficients $g = 0.1\,km^{-1}$, and (2) $g = 0.01\,km^{-1}$. Notice that the sum of both energies, direct and scattered, is constant and equal to W_0. This demonstrates the conservation of energy as shown by Hoshiba 1991.

The scattered energy E_s can be decomposed into different order of scattering or partitions k. Consequently, the total scattered energy W_{sn} due to n- order scattered wave becomes

$$W_s(t) = W_{s1}(t) + W_{s2}(t) + W_{s3}(t) + \ldots. \tag{4.27}$$

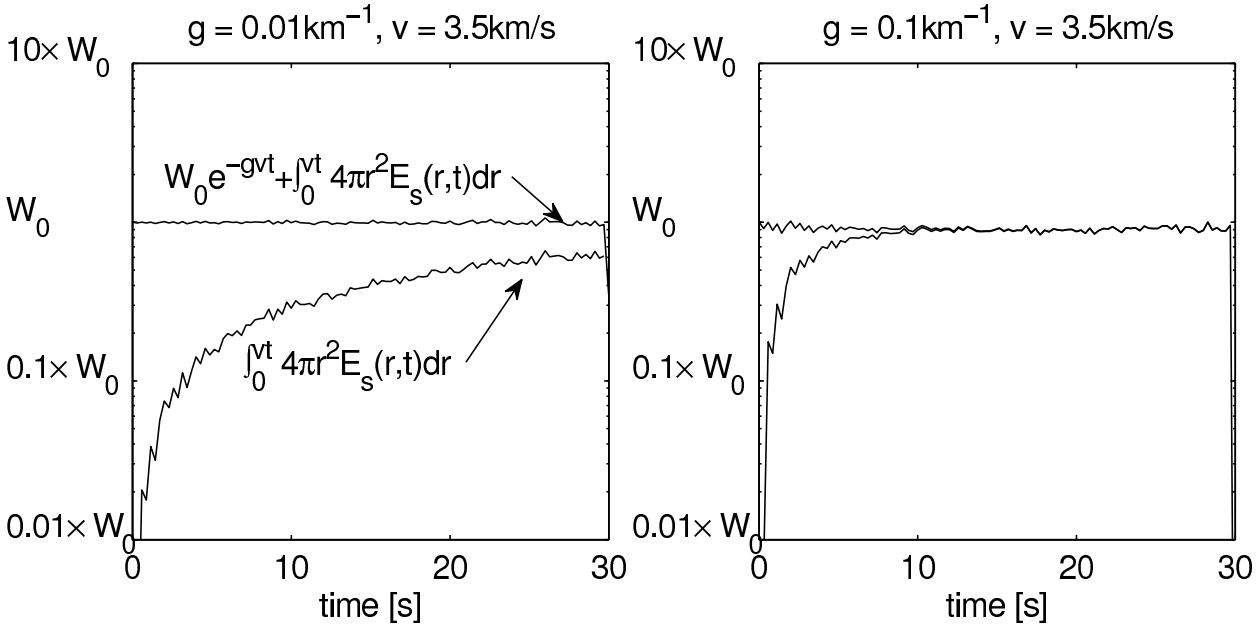

Figure 4.5: Conservation of energy law. Numerical simulation of Eq. (4.26) for two media with S- wave velocity of $3.5\,km/s$ and two scattering coefficients $g = 0.1\,km^{-1}$ (right) and $g = 0.01\,km^{-1}$ (left). The x-axis is the lapse time in seconds. Based on Hoshiba 1991.

The individual contribution W_{sn} for each order of scattering can be expressed as the product of the power n of the normalized distance gvt and an exponential factor

$$W_s n(t) = W_0 A_n (gvt)^n \exp(-gvt). \tag{4.28}$$

By conservation of energy the sum of the direct energy W_d and the scattered energy W_s is equal to the total energy released by the source W_0,

$$W_0 = W_d(t) + W_s(t). \tag{4.29}$$

By combination of Equations (4.27) and (4.29), and substitution into Eq. (4.28). We obtain the following expression,

$$W_0 = W_0(1 + A_1(gvt) + A_2(gvt)^2 + A_3(gvt)^3 + \dots) \times e^{-gvt}. \tag{4.30}$$

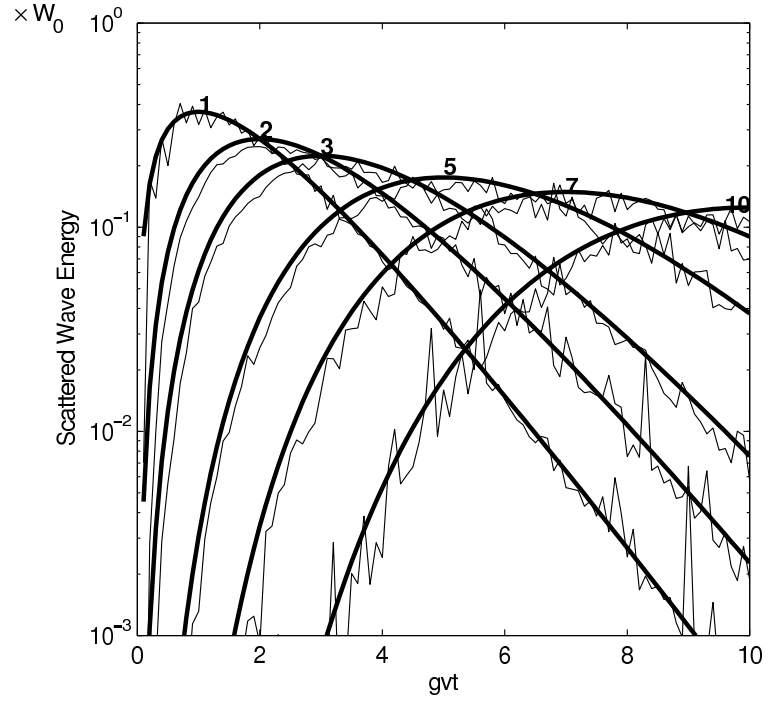

Figure 4.6: Scattered wave energy for different orders of scattering n. Solid lines show the theoretical solution $W_0(gvt)^n \exp(-gvt)/n!$, light lines were obtained by a Monte Carlo simulation with scattering coefficient $g = 0.0\,km^{-1}$, x- axis is the normalized travel distance gvt, numbers on top of each solid line indicate the order of scattering. After Hoshiba 1991.

Expansion of the exponential term e^{-gvt} in a Taylor series shows that the coefficients A_n equals $A_n = 1/n!$. Figure 4.6 shows the partition of energy for scattering order of $n = [1, 2, 3, 5, 7, 9]$. Fine lines were obtained from the numerical simulation shown in Figure 4.5; for a scattering coefficient of $g = 0.1\,km^{-1}$. Solid lines correspond to the theoretical solution Eq. 4.28. Notice that the maximum contribution for a given order of scattering occurs at $gvt = n$. This result shows that the dominant order of scattering n is directly correlated with the normalize distance gvt.

4.7 Separation of intrinsic and scattering attenuation based on multiple scattering theory.

Wu and Aki 1985 introduced the analytical models of energy density distribution of scattered waves based on radiative transfer theory. The total energy density is given by the sum of the direct energy in stationary state plus the contribution of the resulting scattered energy. Let $E_t(r)$ be

$$4\pi r^2 E_t(r) = \exp\left[-Le^{-1}r\right] + 4\pi r^2 \frac{v}{W_0} \int_{r/v}^{r/v+T_0} E_s(r,t) \exp\left(-(1-B_0)Le^{-1}\right) dt \qquad (4.31)$$

The first term is the contribution of the direct energy while the second term accounts for the scattered energy due to the heterogeneities in the medium. The exponential term includes the intrinsic absorption which is omitted in the Monte Carlo simulations. The factor $4\pi r^2$ corresponds to the geometrical spreading correction factor for spherical wavefronts. Thus, the energy density E_n is evaluated for three consecutive windows at $0-15\,s$, $15-30\,s$ and $30-45\,s$ after the arrival of the S- wave . For given hypocentral distance r and frequency f, the energy density becomes

$$E_n(r,f) = \int_{r/v+(n-1)\cdot D}^{r/v+n\cdot D} v \cdot E(r,t)dt. \qquad (4.32)$$

Where $n = 1,2,3$ indicates the time window interval of width $D = 15s$. The technique to separate the scattering and intrinsic attenuation consists basically in fitting theoretical density curves with a set energy measurements at discrete distances r and frequencies f using Eq (4.32). Synthetic envelopes are computed using Monte Carlo simulations as explained in the previous section for media with different scattering coefficients g. Two new variables, seismic albedo and extinction length, are introduced in order to scale the simulations.
The seismic albedo is the ratio of the scattering attenuation to the total attenuation,

$$B_0 = \frac{Q_{Sc}^{-1}}{Q_{Sc}^{-1} + Q_i^{-1}} = \frac{g}{g + \frac{\omega}{Q_i v}} = \frac{Q_{Sc}^{-1}}{Q_{tot}^{-1}}. \qquad (4.33)$$

Extreme cases occur when the intrinsic attenuation $Q_i^{-1} \equiv 0$, then $B_0 = 1$. This shows that all attenuation is due to redistribution of energy in the medium. Oppositely, when $B_0 = 0$ indicates that all loses are consequence of the conversion of energy into heat ($Q_{Sc}^{-1} \equiv 0$).

The extinction length can be interpreted as the distance at which the S- wave energy decays e^{-1}. Hence,

$$Le^{-1} = (Q_{Sc}^{-1} + Q_i^{-1}) \cdot \frac{\omega}{v} = \left(g + \frac{\omega}{Q_i^{-1} v} \right)^{-1}. \tag{4.34}$$

These two parameters are used to scale the simulations.

The first step consist in computing synthetic energy density envelopes $E_s(r,t)$ as shown at the beginning of this section for different media with a constant scattering coefficient $\overline{g}$. Let denote the values use in the simulation by an over-bar. Them we can normalize and compute the energy curves given a pair (Le^{-1}, B_0) by normalizing the variables involved in the integral (4.31),

$$\overline{Le}^{-1} = \overline{g} \cdot \left(\frac{1}{B_0} \right), \tag{4.35}$$

$$\overline{r} = \frac{B_0}{Le\overline{g}} \cdot r, \tag{4.36}$$

$$\overline{h} = \overline{Le^{-1}} \cdot (1 - B_0) = \overline{g} \frac{1 - B_0}{B_0}, \tag{4.37}$$

and

$$\overline{T_1} = \frac{B_0 v}{L_e \overline{g}\, \overline{v}} \cdot T_1, \tag{4.38}$$

$$\overline{T_2} = \frac{B_0 v}{L_e \overline{g}\, \overline{v}} \cdot T_2, \tag{4.39}$$

$$\overline{T_3} = \frac{B_0 v}{L_e \overline{g}\, \overline{v}} \cdot T_3. \tag{4.40}$$

Table 4.1: Simulation parameters.

Scattering Coefficient $\overline{g}[km^{-1}]$	Order of scattering n	Number of particles W_0
0.010	20	5×10^5
0.015	20	5×10^6
0.020	20	5×10^6
0.030	20	5×10^6
0.050	20	5×10^6
0.100	20	5×10^6
0.200	100	2×10^6
0.500	100	1×10^6

Thus, density energy curves for the each window can be written as,

$$4\pi r^2 E_1(r) = \exp(-\overline{Le}^{-1} \cdot \overline{r}) + 4\pi\overline{r}^2 \frac{\overline{v}}{W_0} \int_{\overline{r}/\overline{v}}^{\overline{r}/\overline{v}+\overline{T}_1} E_s(\overline{r},\overline{t}) \exp(-\overline{h}\overline{v}\overline{t}) d\overline{t}, \quad (4.41)$$

$$4\pi r^2 E_2(r) = 4\pi\overline{r}^2 \frac{\overline{v}}{W_0} \int_{\overline{r}/\overline{v}+\overline{T}_1}^{\overline{r}/\overline{v}+\overline{T}_2} E_s(\overline{r},\overline{t}) \exp(-\overline{h}\overline{v}\overline{t}) d\overline{t}, \quad (4.42)$$

$$4\pi r^2 E_2(r) = 4\pi\overline{r}^2 \frac{\overline{v}}{W_0} \int_{\overline{r}/\overline{v}+\overline{T}_2}^{\overline{r}/\overline{v}+\overline{T}_3} E_s(\overline{r},\overline{t}) \exp(-\overline{h}\overline{v}\overline{t}) d\overline{t}. \quad (4.43)$$

The first term in Eq. (4.41) adds the contribution of the direct energy. Notice that the simulations neglect any direct energy arriving at the receiver. The exponential term in the integrand, $\exp(-\overline{h}\overline{v}\overline{t})$, introduces the intrinsic absorption omitted in the simulations. Simulations are constrained to a spatial range of $0 \leq \overline{r} \leq 100\,km$, and time $\overline{t} \leq 50\,s$. The probability that a given particle m at time $\overline{t} = D_m/v$ is calculated Eq. (4.21) and the cumulative probability added into bins of $\Delta t = 0.0292$. Table 4.1 shows the parameters used to generate synthetic energy envelopes.

Figure 4.7 shows the energy curves for four pairs (B_0, Le^{-1}) computed from the simulations in a scaled distance of $0 \leq r \leq 250\,km$. We assume an infinite medium with S-wave velocity

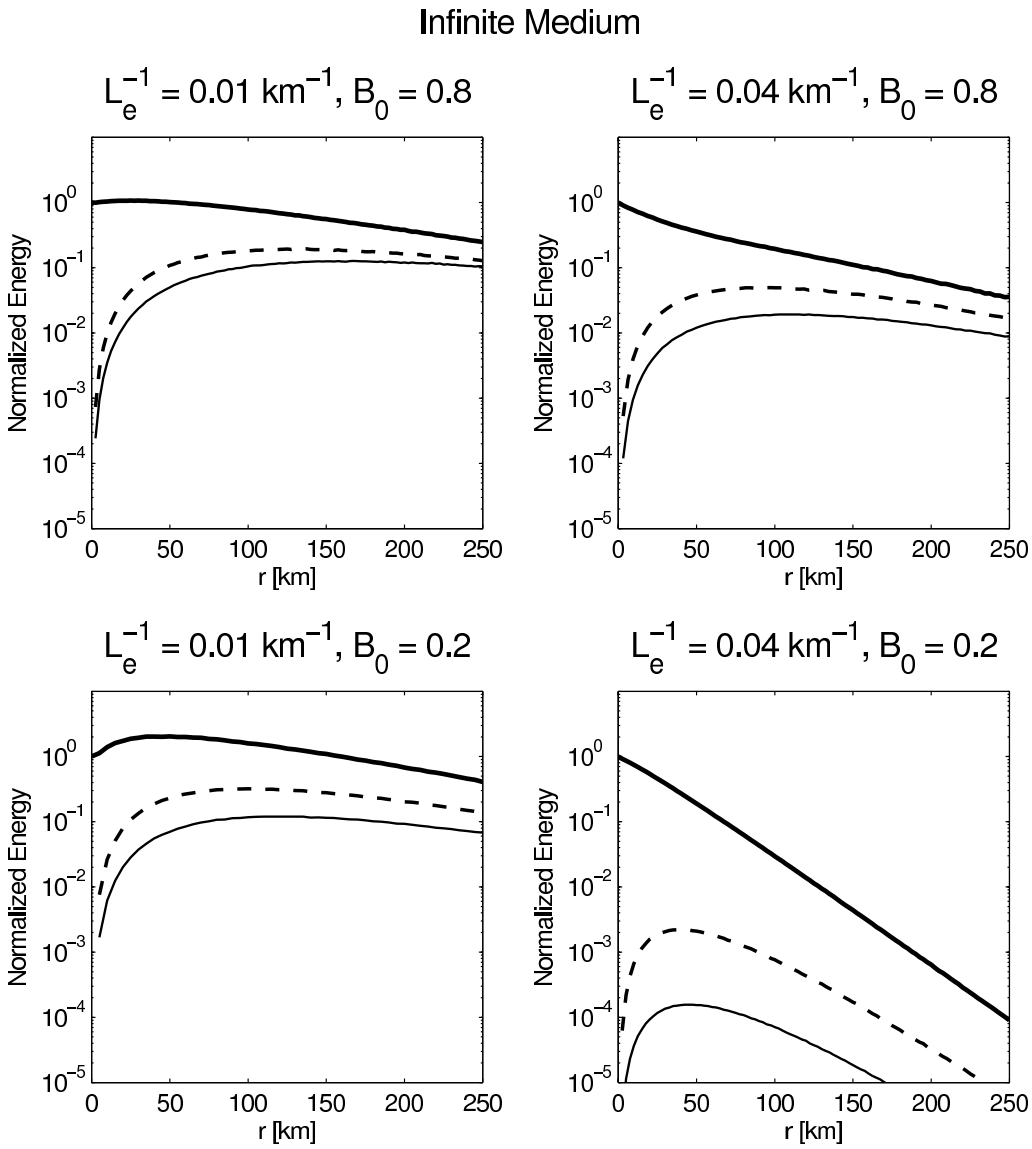

Figure 4.7: Theoretical energy curves for four combinations of seismic albedo B_0 and extinction lengths Le^{-1}. Thick lines correspond to the energy in first window $0 - 15\,s$ after the arrival of the S-wave composed manly of direct arrivals; dashed lines indicate the energy in the second window $15 - 30\,s$; thin lines give the energy in the last window composed mainly of scattered waves. An infinite medium with S-wave velocity of $4km/s$ is assumed in the simulations.

of $4.0\,km/s$. Thick lines indicate the normalized energy density as a function of distance for the first window $0-15\,s$. The first window is manly dominated by direct energy and forward scattered waves. Dashed lines corresponds to the normalized energy density of the second window at $15-30\,s$. Thin lines show the energy in the last window $30-45\,s$ dominated by incoherent coda waves. Observe that the decay with distance is mostly determined by the total attenuation or extinction length Le^{-1}, while the seismic albedo B_0 rules the separation between each curve. The set of parameters (B_0, Le^{-1}) that best fits the observed data is used as a proxy to calculate the independent contribution of Q_{Sc}^{-1} and Q_i^{-1} to the total attenuation,

$$g = B_0 \cdot Le^{-1}, \tag{4.44}$$

$$Q_{Sc}^{-1} = \frac{vB_0}{Le \cdot \omega}, \tag{4.45}$$

$$Q_i^{-1} = \frac{v(1-B_0)}{Le \cdot \omega}. \tag{4.46}$$

Scaling of the simulations allows us to generate a continuous model of attenuation. The next step consists of computing empirical energy curves from real data from either a single station or an array of stations. The basic approach consists in first correcting the data using the coda normalization method explained in Section 4.5. Normalized energies for each window then become (Fehler et al. 1992),

$$ {}_NEI_1(f)_{kj} = \frac{EI_1(f)_{kj}}{W_k^S(f)|N_j^S(f)|^2}, \qquad {}_NEI_2(f)_{kj} = \frac{EI_2(f)_{kj}}{W_k^S(f)|N_j^S(f)|^2}, \text{ and}$$

$$ {}_NEI_3(f)_{kj} = \frac{EI_3(f)_{kj}}{W_k^S(f)|N_j^S(f)|^2}. \tag{4.47}$$

Where $W_k^S(f)$ accounts for the source correction due to the event k, and $|N_j^S(f)|^2$ removes the site effect at j. Source correction factors were found by normalizing the coda envelope by the mean coda amplitude in a $5s$ window at fixed time $45\,s$ after the origin of the event. This factor normalizes the differences in magnitude among different events. Relative site amplification factors are obtained by comparing the coda amplitude from a reference event at different stations. For a sufficient large number of stations and events, we obtain average

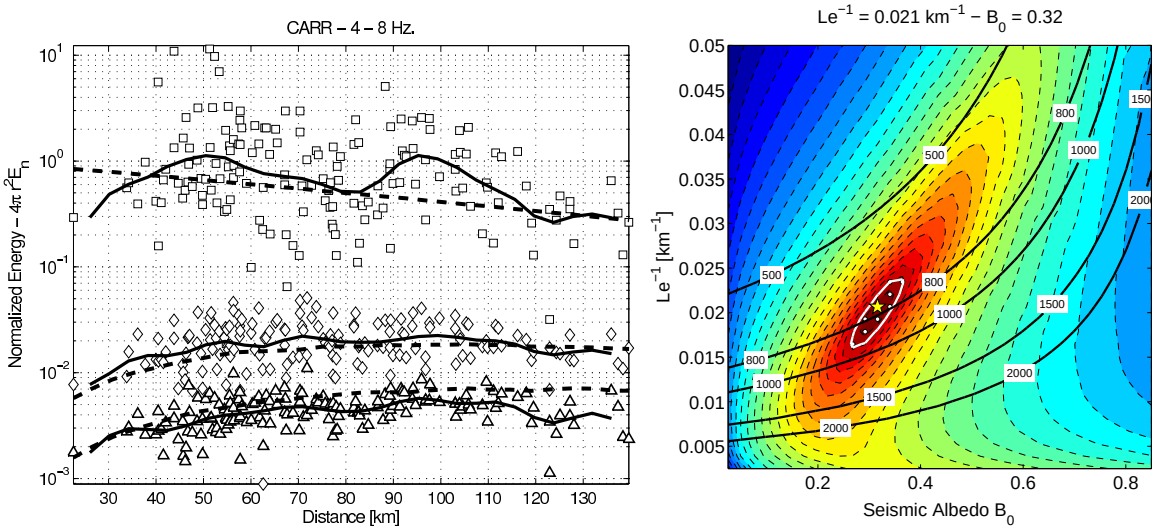

Figure 4.8: Curve fitting using the MTLW method. (left) Estimates of normalized energy density for station CARR in the band of $4-8\,Hz$. Squares, diamonds and triangles correspond to the windows $0-15\,s$, $15-30\,s$ and $30-45\,s$, respectively. Tick lines indicate the running mean average in a window of $15km$ with an overlap of 50%. Dashed line shows the theoretical set of curves that best fit the observations. (right) Map of residuals. Contours show the the misfit between the data and the model for parameters B_0 and Le^{-1}. Labeled contours indicate lines of constant intrinsic attenuation Q_i. The star indicates the optimum, dashed area shows the 95% confidence level.

normalized energy densities $\langle {}_N EI_{1,2,3}\rangle_d$ by taking a running mean on sliding space windows of $15km$. Figure 4.8 shows an example of the MLTW method for one station CARR in Guerrero, Mexico. The left panel shows the normalized energy density for 162 events in a radius of $140\,km$. For this example only events shallower than $20\,km$ are considered. Each seismogram was tapered and filtered with a $4-$ pole Butterworth filter with central frequency of $6\,Hz$ and bandwidth of $\pm 2\,Hz$. Estimates for the $0-15\,s$, $15-30\,s$ and $30-45\,s$ are indicated with squares, diamonds and triangles, respectively. Solid lines are obtained by averaging the data points into 30 bins with an overlap of 50%. Dashed lines are obtained

from the Monte Carlo simulations for the set of parameters (B_0, Le^{-1}) that best fit the data. The right panel shows the residuals obtained using

$$\text{Residual} = \log_{10} \sum_{k=1}^{N} \left[\log_{10} \left(\frac{4\pi r_{kj}^2 E I_n(f)_k j}{E^{S\,Coda}(f)_{jk}} \right) - \log_{10} \left(\frac{4\pi r_{kj}^2 E I_n^{\text{Theory}}(B_0, Le^{-1})}{C_j} \right) \right]^2 . \tag{4.48}$$

Where n indicates the time window, r_{kj} is the hypocentral distance between the receiver j and the event k. $E^{S\,Coda}(f)_{jk}$ is the source normalization factor that corresponds to the mean coda amplitude in a $10\,s$ window at $45\,s$ from the time of the event. C_j is the offset due to the gain of the instrument and the unknown site amplification factor in cases of single station studies.

We normalized the residual by dividing each grid point by the minimum sum square of residuals. Each curve consists of 30 data points, resulting in a total of 90 data points with a 50% overlap. Using the F distribution for two random variables with 45 degrees of freedom, we limit the 90% confidence interval by excluding the normalized residuals exceeding 1.47. The star in the right panel of Figure 4.8 shows the best solution found by grid search while circles mark the 90% confidence interval of the solution. For this particular case, we found a extinction length of $Le^{-1} = 0.0108 \pm 0.0042 km^{-1}$, meaning that the S- wave decays e^{-1} in $92.6 \pm 36 km$. The seismic albedo indicates that $32 \pm 4\%$ of the total attenuation is due to redistribution of energy in the medium, and the remaining 79% is caused by conversion of energy into heat or intrinsic absorption. The scattering coefficient is the ratio between the seismic albedo B_0 and the extinction length Le as shown in Eq. (4.44). In this case, the solution yields to a scattering coefficient of $g = 2.2 \pm 1 \times 10^{-3}\, km^{-1}$. Finally, the predicted values for attenuation at $6Hz$ are: $Q_{tot}^{-1} = 1 \pm 0.33 \times 10^{-3}$ for total attenuation, $Q_i^{-1} = 0.79 \pm 0.31 \times 10^{-3}$ for intrinsic attenuation, and $Q_{Sc}^{-1} = 0.21 \pm 0.1 \times 10^{-3}$ for scattering attenuation. These results show that the contribution of scattering attenuation is greater compared to the intrinsic absorption. However, we will later show that at lower frequencies intrinsic attenuation dominates.

4.8 Scattering in layered media

In the former section, we assumed an infinite medium filled with evenly distributed scatters. Yoshimoto 2000 suggested an alternative methodology to compute synthetic energy envelopes for layered media. He introduced a procedure known as the Direct Simulation Monte Carlo Method (DSMC). This model is based on kinetic gases theory and considers the effect of gradient in the velocity of the medium. The scattering coefficient g is assumed to be constant, and perturbations in the velocity field are not considered. Particles are isotropically shot from the source at (x_0, y_0, z_0) with a take off angle from the downward vertical θ and azimuth ϕ.

$$\begin{aligned} \theta &= \arccos(1 - 2U_1), \\ \phi &= 2\pi U_2. \end{aligned} \tag{4.49}$$

Where U_1 and U_2 are uniform random variables in the range $[0, 1]$. Eq. (4.49) ensures that particles are evenly distributed on the surface of a imaginary sphere around the source. Once particles leave the source, their trajectories are calculated according to the ray theory. At each time step Δt, particles move a distance $v(z)\Delta t$. The parameter Δt is chosen under the condition $\Delta t \ll (gv(z))^{-1}$ to ensure convergence of the numerical solution. The next position of the particles is constrained to plane $x' - z$ (see Figure 4.9) by keeping the azimuthal angle ϕ unchanged. Thus, the spatial increment after time Δt is

$$(\Delta x, \Delta z) = v(z)\Delta t \cdot [\sin\theta, \cos\phi]\,. \tag{4.50}$$

The new take off angle θ is calculated by adding the corresponding change $\Delta\theta$ due to the structure of the medium,

$$\Delta\theta = \frac{dv(z)}{dz}\Delta t \sin\theta. \tag{4.51}$$

Eq. (4.50) and (4.51) determine the position of the particle until it reaches a scattering point. The probability that a given particle scatters after at each time interval Δt is

$$gv(z)\Delta t \sim 1 - \exp(-gv(z)\Delta t). \tag{4.52}$$

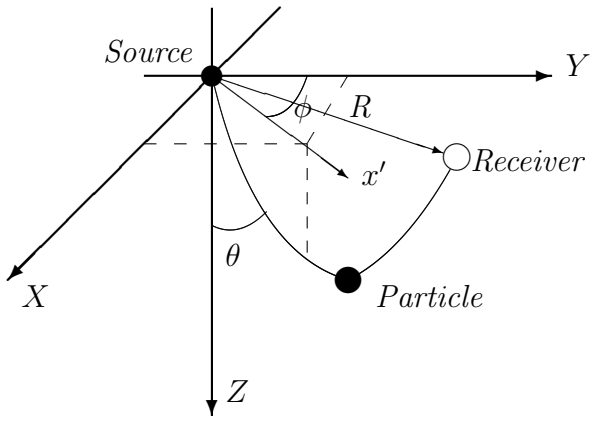

Figure 4.9: Scheme of the DSMC method. Particles are isotropically shot from the source with a take off angle θ and azimuth ϕ, R is the distance from the source to the receiver.

Therefore, the occurrence of scattering along the trajectory of propagation is determined by the inequality,

$$gv(z)\Delta t > U_3. \tag{4.53}$$

Where U_3 is a uniform random variable $[0, 1]$. The new direction of propagation is calculated from Equations (4.49). The energy density is estimated by counting the number of particles reaching a toroidal volume ΔV of radius R beneath the receiver. Hence, the energy density as a function of time is

$$E(t) = \frac{n(t)}{N\Delta V} = \frac{n(t)}{N\pi^2 r^2 R}. \tag{4.54}$$

Where $n(t)$ is the number of particles inside the volume ΔV at time t, N is the total number of particles shoot from the source, R is the epicentral distance from the source to the receiver (notice that the source does not necessarily lies on the surface), and r is a small radius around the receiver $\sim 1\,km$. Figure 4.10 shows the ray paths for a few selected particles traveling in a two-layer medium with a gradient in the upper layer shown in the left panel. Note the bending of the ray paths in the upper layer due to the positive gradient in velocity and leaking towards the second layer for particles with high incident angles.

Figure 4.11 shows a set of synthetic envelopes generated using the DMCS method for different scattering coefficients $g = 0.01, 0.015, 0.5, 0.1\,km^{-1}$. The velocity model used to

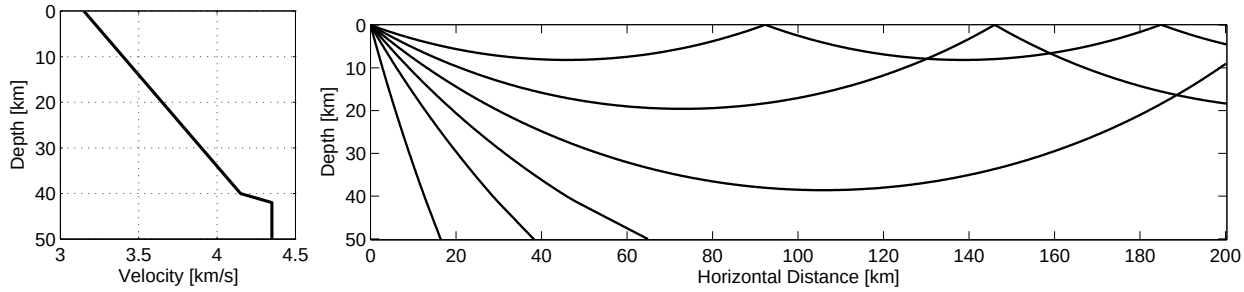

Figure 4.10: Particles trajectories for a layered medium. (left) two layer velocity model of the crust and upper mantle. (right) particle trajectories.

generate these envelopes is shown in the left panel in Fig. 4.10. Each subplot shows the synthetic envelopes for 20 receivers with epicentral distances between $5-100km$, spaced every $5km$. The source was located at $2\,km$ from the source. Scattering coefficients $g = 0.01\,km^{-1}$ and $g = 0.015\,km^{-1}$ correspond to weakly scattering media. At this scattering range, coda shows a similar behavior than actual recorded seismograms. Coda time decay is independent of distance and converges to an asymptotic value regardless of the location of the receiver. High scattering coefficients ($g = 0.05, 0.1\,km^{-}1$) indicate a strong scattering medium, with mean free path of the order of $\sim 10km$. Observe a rapid decay of direct waves with distance, coda waves dominate most of the record. Figure 4.12 shows the vertical distribution of particles for different models. Model 1 is used to illustrate the hypothetical case of a two-layer medium analog to the crust overlying the upper mantle. Model 1' is a modified version that includes a low velocity layer analog to a sedimentary layer on the top of the crust. Model 1" considers a negative gradient on top of the crust-mantle transition zone. Models 2 and 3 correspond to depth independent velocity models. The right side shows the vertical distribution of the particles for a receiver located at hypocentral distance of $80km$ in a medium with scattering coefficient of $g = 0.02\,km^{-1}$. Stagnation of particles towards the surface is the result of the positive gradient in the top layer. Layering in the medium can cause an overestimation of the scattering coefficient g compared to an homogeneous velocity

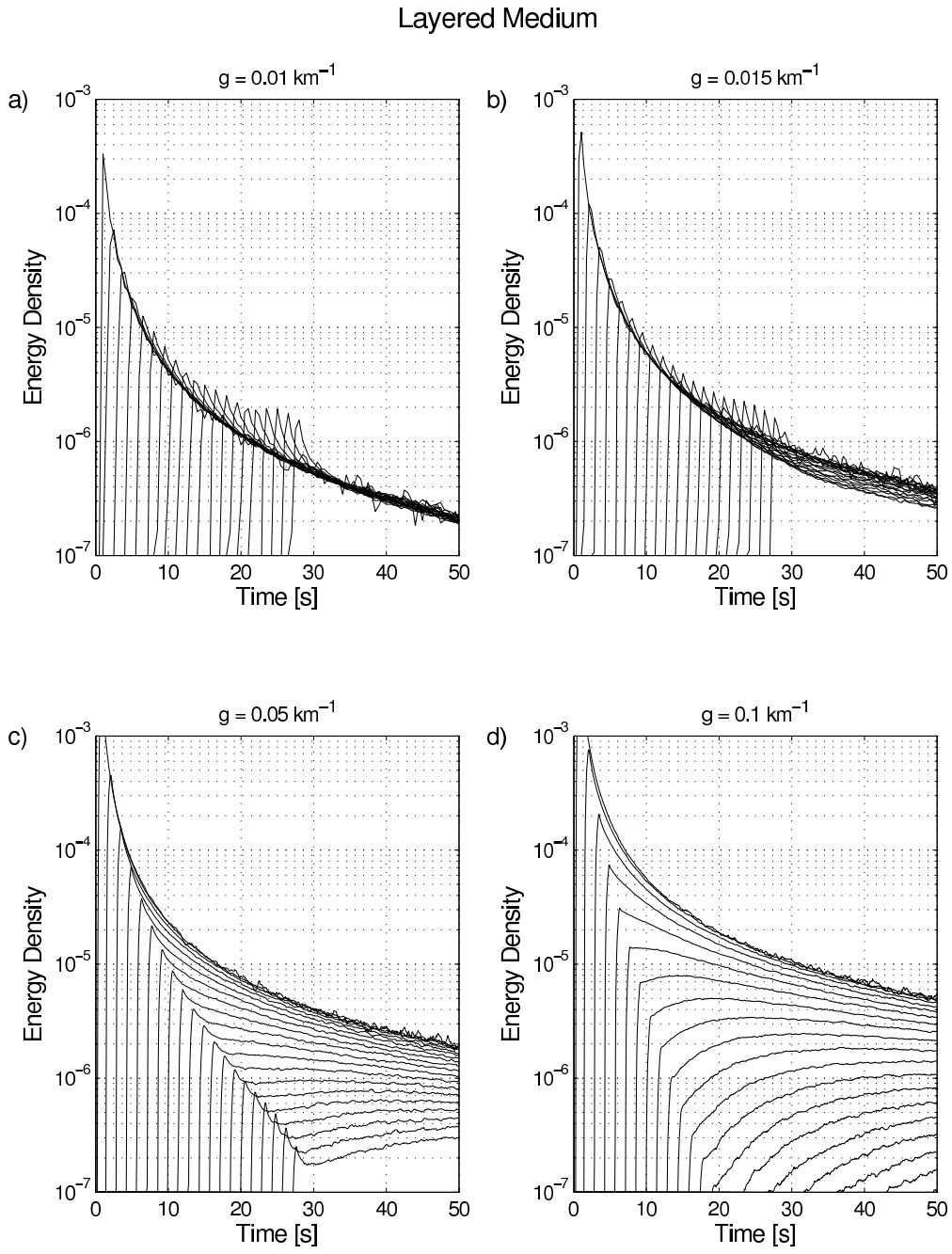

Figure 4.11: Synthetic energy density envelopes for a layered medium using the Direct Monte Carlo Simulation method (Yoshimoto 2000). Each subplot contains synthetic envelope for 20 receivers located every 5 km from the source up to 100 km.

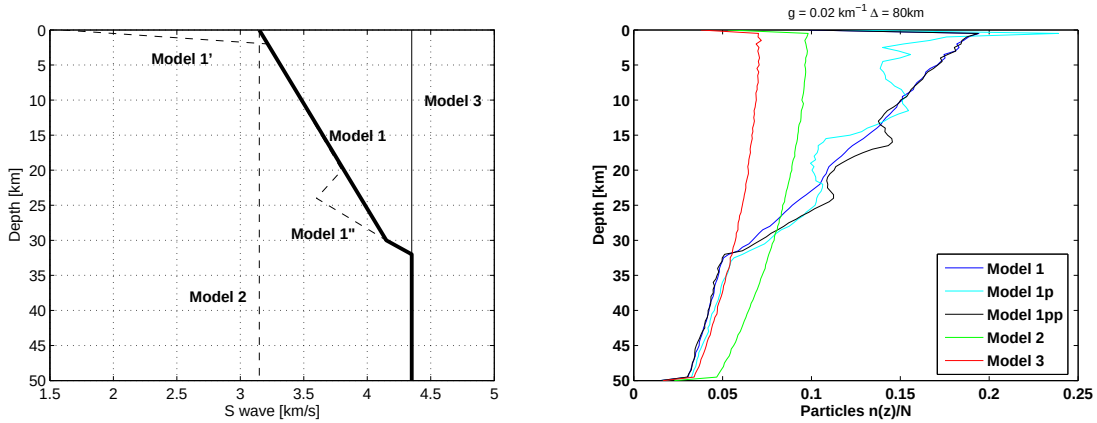

Figure 4.12: Vertical distribution of particles for different velocity models. (left) shows the velocity models as a function of depth. Model 1 corresponds to a two-layer model medium with a gradient in the top layer.

medium as shown by Yoshimoto 2000.

4.9 Conclusions

Modeling propagation of seismic waves in random media persists as a highly controversial subject. Disagreement between different groups lies mainly in the fact that completely different models of attenuation fit the observed data equally well. Through the years different authors investigated the nature of the scattered fields based on very diverse assumptions. Initial models of scattering suggested that first order backscattering seismic waves give rise to the series of incoherent waves that follow P- and S- waves. Subsequent models introduced multiple scattering; and isotropic and forward modes of propagation. Alternative theories had remarkable success fitting the data using empirical models based on diffusion and radiative transfer theories. Despite the apparent arbitrary description of the scattered fields, some major features of coda waves are widely accepted. For example, there is a general consensus that at twice the lapse time, coda wave energy is homogeneously distributed in a

volume underneath the station. Moreover, coda waves are believed to be formed mainly of shear waves. In addition, distinction of the different components of attenuation remains an intricate problem given the heterogenous nature of the crust at different scales.

The goal of this chapter is to introduce the basic ideas behind the scattering model. In the following chapter, we will adopt the Multiple Time Lapse Window method to obtain separate estimates of the contribution that heterogeneities in the medium have to the total attenuation. In particular, we will discuss the applicability that this method in the Middle America region.

CHAPTER 5

Attenuation measurement in the Middle America Region

5.1 Abstract

Attenuation in the Middle America Region is one of the highest found in the literature (Margerin et al. 1998). Separation of intrinsic and scattering attenuation from the total attenuation is carried out using the Multiple Time lapse window method (MTLW) in ten frequency bands between $0.75 \leq f \leq 20 Hz$. Events are classified into four different groups according to the depth: 1) $0 \leq d \leq 100\,km$; 2) $0 \leq d \leq 20\,km$; 3) $0 \leq d \leq 40\,km$, and 4) $20 \leq d \leq 100km$. Unlike previous studies, we focus our interpretation in the frequency and depth dependance of the results. As shown in Chapter 3, the flat subducting slab plays an important role in the propagation of low frequency body waves $f \leq 1.0\,Hz$. In this Chapter, we analyze the attenuation at higher frequencies and the possible effects that the tectonic setting has at higher frequencies ($> 1\,Hz$) (shorter wavelengths). We compare the normalized energy curves with theoretical curves obtained for two types of 'synthetic' media. 1) An infinite medium with a constant velocity and homogenous distribution of scatters, and 2) a two layer media emulating a $40\,km$ crust with a velocity gradient and even distribution of scatters overlying a infinite half space representing a transparent mantle. In addition, we explore the consequences of assuming a spherical geometrical spreading and the preferential mode of propagation of the scattered waves.

Table 5.1: Previous studies.

Region	Range	$Q(f)$	Reference
Oaxaca	$0.7 < f < 1.7 Hz$	$Q_{Lg} = 208 f^{0.4}$	Canas et al. 1988
Chiapas	$0.7 < f < 1.7 Hz$	$Q_{Lg} = 211 f^{0.4}$	Canas et al. 1988
Guerrero	$0.1 < f < 40 Hz$	$Q_S = 278 f^{0.92}$	Castro et al. 1990
Guerrero	$0.2 < f < 10 Hz$	$Q_S = 273 f^{0.66}$	Ordaz and Singh 1992
Oaxaca	$1.0 < f < 25 Hz$	$Q_P = 22 f^{0.97}$	Castro and Mungia 1993
Oaxaca	$1.0 < f < 25 Hz$	$Q_S = 56 f^{1.01}$	Castro and Mungia 1993
TMVB	$1.6 < f < 8 Hz$	$Q_{Lg} = 226 f^{0.486}$	Ottemöller et al. 2002
Guerrero	$1.6 < f < 8 Hz$	$Q_{Lg} = 193 f^{0.872}$	Ottemöller et al. 2002
Oaxaca	$1.6 < f < 8 Hz$	$Q_{Lg} = 228 f^{0.895}$	Ottemöller et al. 2002

5.2 Introduction

Numerous studies have investigated the attenuation in southern and central Mexico (Canas et al. 1988, Castro et al. 1990, Ordaz and Singh 1992, Castro and Mungia 1993, Castro et al. 1994, Ottemöller et al. 2002). Table 5.1 summarizes some studies of attenuation carried out in the Middle America Region. Canas et al. 1988 studied the seismic attenuation of Lg waves in southern Mexico using the coda Q method for a low frequency band around $1\,Hz$. Castro et al. 1990 calculated the attenuation of $S-$ waves along the subduction zone. This study considers changes in the geometrical spreading as a function of frequency. Ordaz and Singh 1992 investigated the attenuation in the Mexico City basin. Their results demonstrated large amplification factors in the hill zone of Mexico city. They estimated the quality factor of $Q_S = 273 f^{0.66}$ for southern Mexico. Castro and Mungia 1993 calculated the attenuation for $P-$ and $S-$ waves for the Oaxaca region. In a later paper, Castro et al. 1994 compared results of attenuation between the Oaxaca and Guerrero region. Their results show that attenuation in Oaxaca is between 3.7 to 5.0 times stronger than the

attenuation in Guerrero in the range of $1-30\,Hz$. Ottemöller et al. 2002 analyzed the lateral variation of Lg waves. They concluded that propagation of Lg become inefficient in the Gulf of Tehuantepec and along the costal plains of the Gulf of Mexico. Contrary to Castro et al. 1994, they found that attenuation is higher in Oaxaca compare with Guerrero. Garcia et al. 2009 found changes in the attenuation between inland paths and along the Pacific coast. They suggested that the structure of the subduction zone causes changes in the geometrical spreading. For trajectories along the coast, they defined the geometrical spreading as

$$G(r) = \begin{cases} r^{-1}, & \text{for} \quad r < 50\,km \\ (50r)^{0.5}, & \text{for} \quad r \geq 50\,km \end{cases} \tag{5.1}$$

and for inland paths the geometrical spreading becomes,

$$G(r) = \begin{cases} r^{-1}, & \text{for} \quad r < 50\,km \\ 1/50, & \text{for} \quad 50 \leq r < 150\,km \\ (50r)^{0.5}, & \text{for} \quad r \geq 150\,km. \end{cases} \tag{5.2}$$

Using 2D numerical simulations, Cruz-Jimenez et al. 2009 analyzed the influence of the TMVB and the geometry of the subduction zone for trajectories perpendicular to the trench in Colima and Guerrero.

5.3 Data

Separation of scattering and intrinsic attenuation is carried out along two profiles: 1) perpendicular to the trench for 25 stations from the MASE array, and 2) along the trench for permanent stations. The local seismological service (SSN) reported a total of 1354 local events during the period 2005-2007. The magnitudes of these events range between $2.9 \leq M_w \leq 5.4$. Figure 5.1 shows the location of the stations analyzed and the local seismicity color-coded as a function of depth. Note the irregular distribution of the seismicity along the trench. In the southeast along the Isthmus of Tehuantepec, seismicity extends from

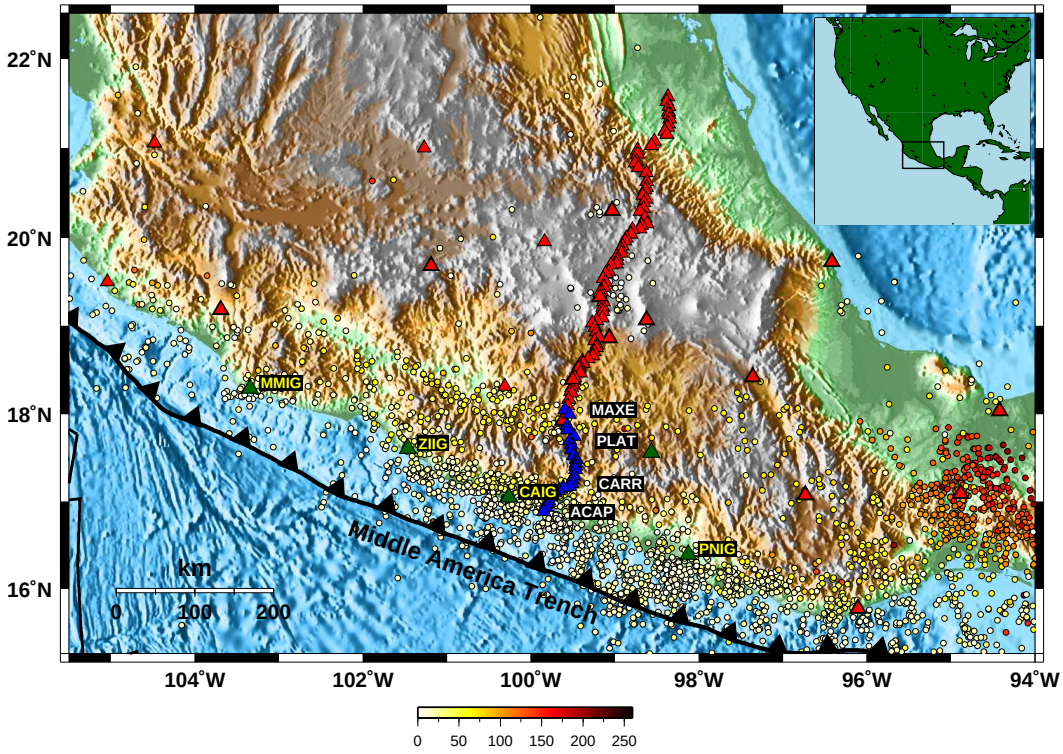

Figure 5.1: Map of seismic stations and seismicity in Mexico. Blue triangles show the location of the MASE array; green triangles indicate the location of the permanent local stations used in this study. Red triangles indicate stations not used in this study due to the sparse seismicity or poor quality data. Circles indicate the seismicity between 2005-2007 color coded as a function of depth. Notice the distribution of seismicity along the trench from shallow seismicity in central and western Mexico to deep events to the southeast.

the trench to $\sim 300\,km$ inland. This area corresponds to the dipping section of the slab, seismicity progressively deepens from the the trench up to $250\,km$. The central part of the trench shows higher seismicity in a narrow band of $\sim 100\,km$ towards the trench where most of the seismicity occurs in the upper $\sim 60\,km$. This region corresponds to the flat part of the subducting slab. Red triangles indicate stations from either the MASE array or the permanent network that were not used in this study due to the sparse seismicity in a

radius of $140\,km$. Only seismic records with a signal to noise ratio higher than three and hypocentral distance between $40 \leq e_{hypo} \leq 140\,km$ are used in this study.

5.4 Separation of the intrinsic and scattering attenuation along and perpendicular to the coast

We compute independent estimates of intrinsic and scattering attenuation using the Multiple Time Lapse Window method described in Chapter 4. The frequency dependance of Q is obtained by iteration of the MTLW method for different frequencies. Figure 5.2 illustrates the computation of energy density windows. The first step consists of applying a bandpass filter at different frequencies. We used a 4-pole Butterworth filter with central frequencies f_c=[0.75, 1.0, 1.5, 2.0, 3.0, 4.5, 6.0, 9.0, 12.0, 15.0]Hz. Corner frequencies are estimated as function of the central frequency as $f_{high,low} = (1 \pm 1/3) f_c$. The envelope of the seismogram is obtained by sampling the maximum absolute value in n windows of width $T_w = 1/f_{low}$. Then, we compute the normalized energy density for three $15s$ consecutive time windows after the theoretical S- wave arrival. Each envelope is normalized by dividing the coda mean amplitude in a $5s$ window at fixed time, in this case, $45s$. As discussed in Chapter 4, this removes the site and source effects making it possible to compare events with different magnitude, and stations located on different lithologies. The following figures show the step by step analysis of the MASE array assuming an infinite medium for events shallower than $40km$.

Figure 5.3 shows the frequency dependance of the seismic albedo B_0 and the extinction length Le^{-1} for 25 stations perpendicular to the trench. Seismic albedos between stations ACAP and PETA show consistent values among all stations at different frequencies. Low frequencies show higher seismic albedo, meaning that attenuation is mostly dominated by the effect of heterogeneities in the crust while attenuation at higher frequency is mostly due to conversion of energy into heat and anelastic deformation of the rocks. Between stations

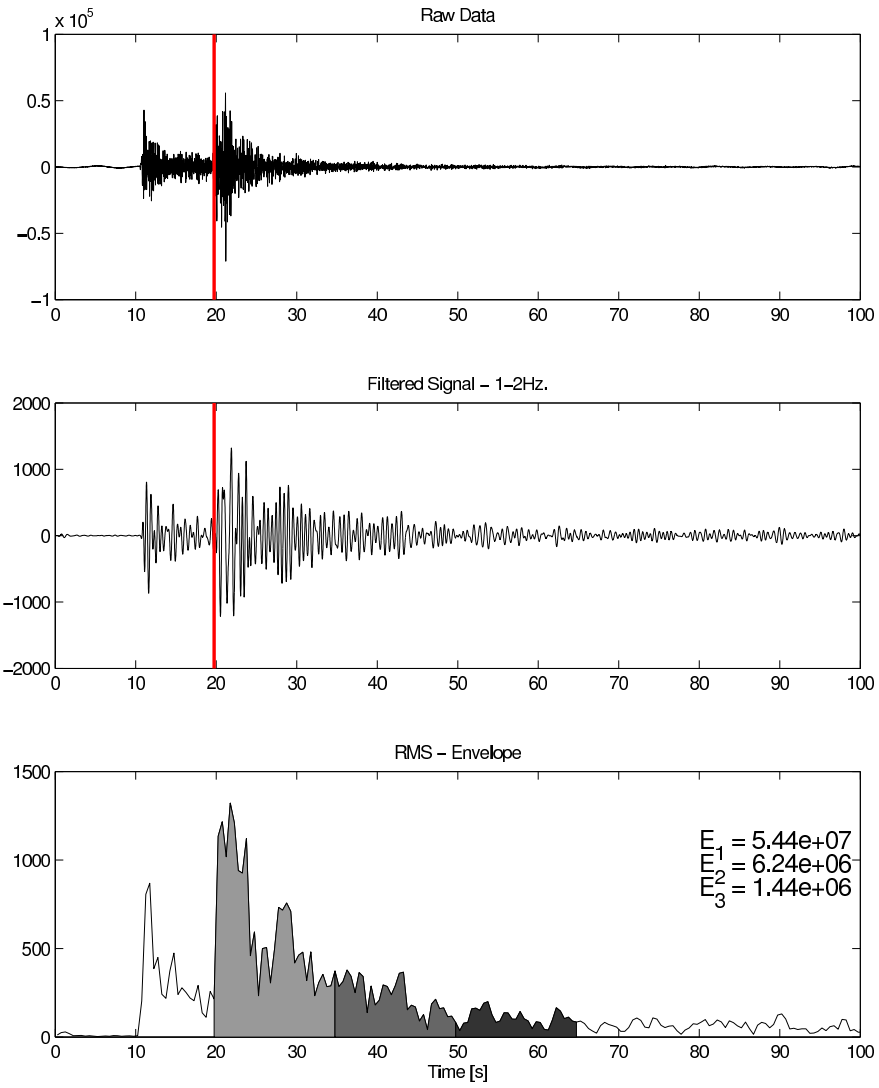

Figure 5.2: Example of the normalized energy analysis. (Top) shows the raw data for an arbitrary station, the vertical line indicates the S-wave arrival. (Middle) Filtered data between $1-2\,Hz$. Each seismograms is filtered using a 4-pole Butterworth with bandwidth $2f_{central}/3$. (Bottom) Root mean square amplitude of the filtered signal. Shaded areas indicate the intervals of integration for each of the consecutive time windows.

UICA and MAXE, estimation at low frequencies ($0.75Hz$ and $1.0Hz$) become unstable. This is likely caused by a low signal to noise ratio due to a change in the near surface lithologies.

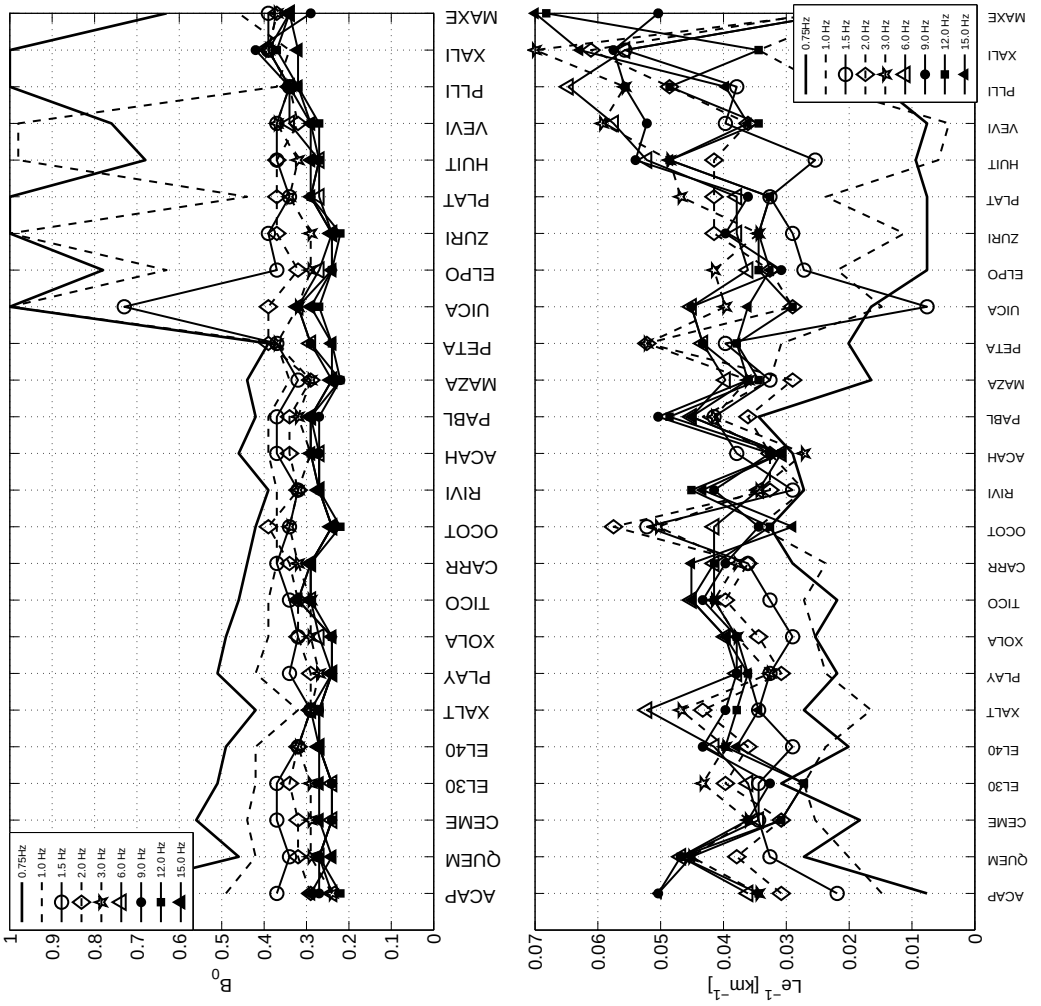

Figure 5.3: (Left) Seismic albedo B_0 as a function of frequency for the MASE array. Each line denotes a different frequency. (Right) Extinction length Le^{-1} as a function of frequency. Stations are sorted by latitude, ACAP is the closest to the coast.

On the other hand, the extinction length shows a low frequency dependance regardless of the location of the station.

Figure 5.4 shows the intrinsic Q_{In}^{-1} and scattering attenuation Q_{Sc}^{-1} for the same set of stations. Notice that intrinsic attenuation at low frequencies ($0.75 \leq f_{central} \leq 3.0\,Hz$) remains relatively constant. Conversely, scattering attenuation at higher frequencies ($> 3\,Hz$) de-

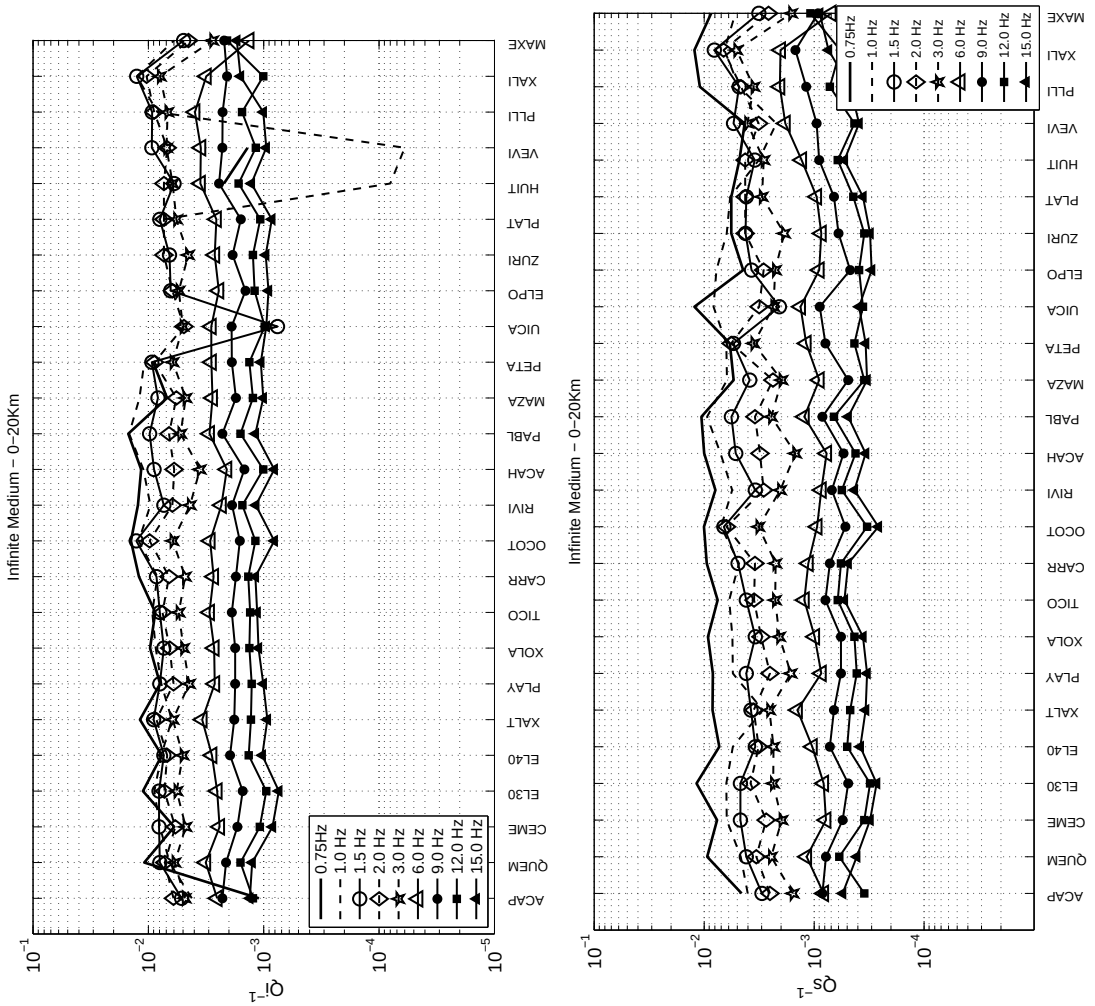

Figure 5.4: (Left) Intrinsic attenuation Q_{In}^{-1} as a function of frequency for the MASE. Each line corresponds to a different frequency. (Right) Scattering attenuation Q_{Sc}^{-1} as a function of frequency. Stations are sorted by latitude, station ACAP is the closest to the coast.

creases as frequency increases. In both cases, attenuation varies smoothly between stations. In general, most parts of the spectrum are dominated by intrinsic attenuation as shown in Figure 5.5. Notice the change in frequency dependance between low and high frequencies. Average results for all stations perpendicular to the trench are shown in Figure 5.6. Interestingly, frequency dependence of the variables B_0, Le^{-1} and g disappears for frequencies larger

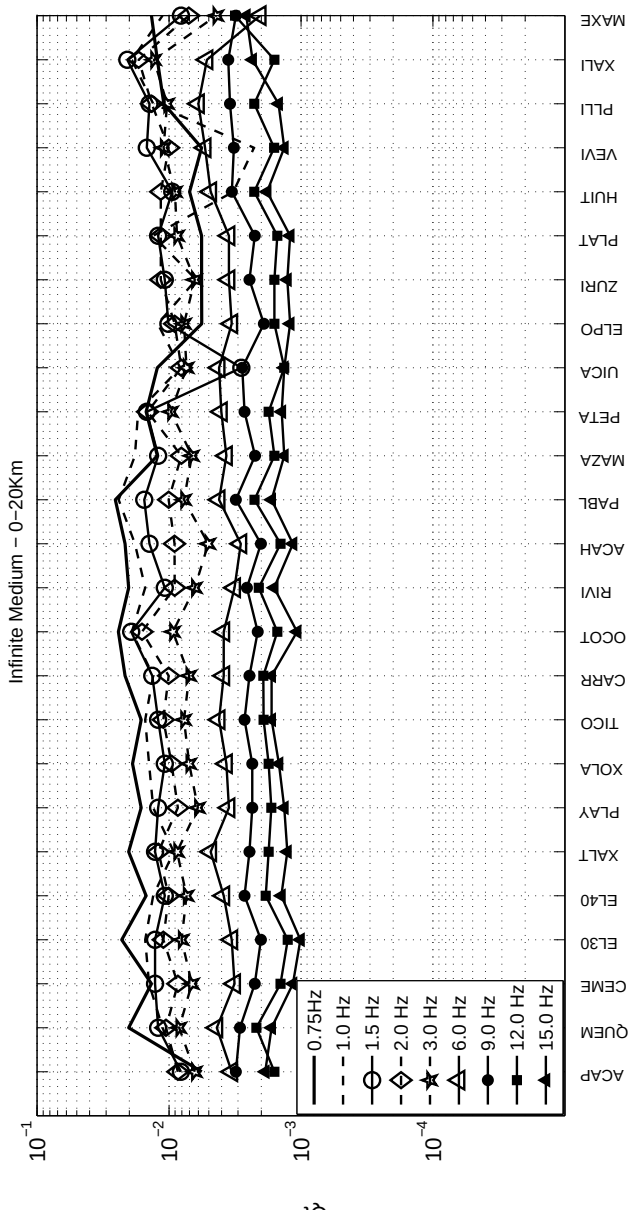

Figure 5.5: Total attenuation Q_{Tot}^{-1} as a function of frequency. Each line corresponds to a different frequency. Stations are sorted by latitude, stationACAP is the southern most station of the array.

than $3\,Hz$ as shown in the left panel. The right panel shows the average attenuation curves. Notice the almost flat trend of the intrinsic attenuation in the range $0 \leq f \leq 3.0\,Hz$ and the change in frequency dependance at the $3\,Hz$ mark for scattering and total attenuation. Stations along the coast have a slightly lower scattering attenuation as demonstrated in Fig. 5.7. Processing of the data for the permanent network installed perpendicular to the MASE array using the same criteria (selection of events and inversion parameters) reflects a change in the scattering attenuation regime. The solid line corresponds to the average results for the MASE array (Figs. 5.4 and 5.5). For intrinsic and scattering attenuation, both profiles, perpendicular and parallel to the trench, fit the data remarkably well with exception of the ZIIG station at $0.75\,Hz$. This is likely due to the fact that this station recorded a fewer number of events and that signal to noise ratios are usually lower at low frequencies.

5.5 Depth dependance of the attenuation

Figure 5.8 summarizes the different results of attenuation along the MASE array for two different models of the crust, and four different ranges. Each component of the attenuation is indicated by a different marker: circles for total attenuation; triangles for intrinsic attenuation; and squares for scattering attenuation. We used the model $Q(f) = Q_0 f^{\eta}$ in the range of $3 \leq f \leq 15\,Hz$, where Q_0 is the extrapolated attenuation at $1\,Hz$. Different colors indicate the selection of the events as a function of depth. Black markers were obtained by analysis events occurring in the upper crust ($0 \leq d \leq 20\,km$); red markers indicate events with crustal depths ($0 \leq d \leq 40\,km$); blue markers correspond to depth range of ($0 \leq d \leq 100\,km$) and green markers exclude shallows events ($20km \leq d \leq 100km$). Solid markers indicate the model used to compute the synthetic envelope corresponding to an infinite medium with an even distribution of scatters. Open circles denote the results using a two layered model representing a $40\,km$ thick crust with a velocity gradient and event distribution of scatters overlying an infinite half space representing transparent mantle. Notice

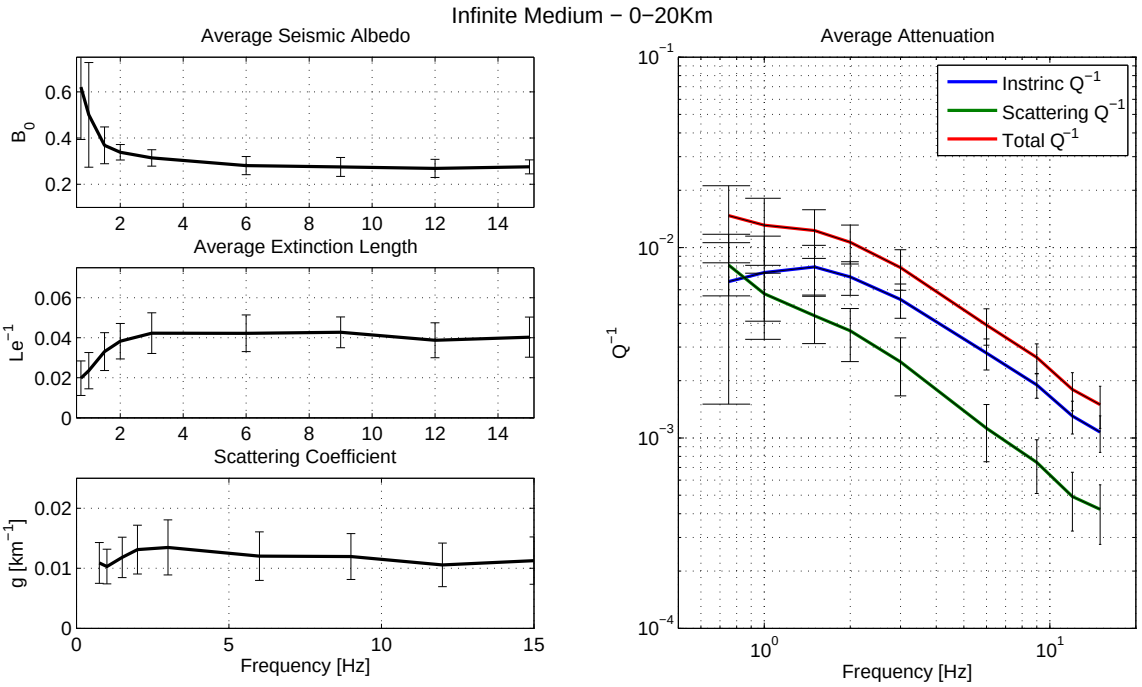

Figure 5.6: Average results for the MASE array. (left-top) seismic albedos B_0 as a function of frequency; (left-middle) extinction length Le^{-1} and scattering coefficient g. The right panel shows the average attenuation Q_{Tot}^{-1}, Q_{In}^{-1} and Q_{Sc}^{-1} for all stations.

that by using a layered media for the inversion leads to higher values of scattering attenuation ${}_{Sc}Q_0$ (higher albedos) and lower estimates for intrinsic (${}_{Int}Q_0$) and total attenuation (${}_{Tot}Q_0$). Classification of the events reveals lower values of the parameter η for crustal events ($depth \leq 40\,km$). Therefore, we suggest that an additional mechanism such as change in the geometrical spreading for crustal events can explain this discrepancy.

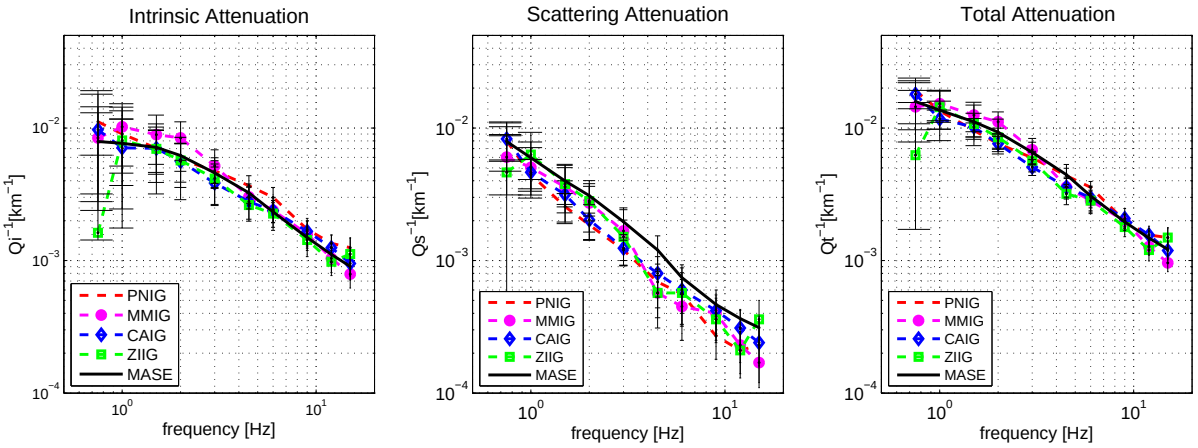

Figure 5.7: Comparison between the attenuation along the MASE array and stations along the coast. (left) Intrinsic attenuation Q_{In}^{-1}, (middle) scattering attenuation Q_{Sc}^{-1}, (top) total attenuation Q_{Tot}^{-1}.

5.6 The role of assuming the intrinsic attenuation and geometrical spreading

Results in the previous sections shows that total attenuation is frequency dependent in the range of $1 < f < 10\,Hz$ with a decreasing frequency dependance towards both ends ($f \leq 1\,Hz \cap f \geq 10\,Hz$). This observation is in agreement with borehole observations using the same method (Adams and Abercrombie 1998). However, laboratory experiments propose that Q_i is approximately frequency independent (Knopoff 1964; Jackson 2000). Margerin et al. 1999 applied a simple layered model to the set of stations along the coast of Mexico and concluded that a weak quality factor of $Q_i = 1000$ can adequately fit the observation of coda attenuation Q_c in the frequency range of $0 \leq f \leq 15\,Hz$. Their analysis suggested that leakage of energy into the mantle at low frequencies $\sim Hz$ heavily affect the coda attenuation, while high frequencies are mostly determined by the intrinsic attenuation. Nonetheless, this model overlooks the effect that the flat subducting slab has on low frequencies as demonstrated by Dominguez et al. 2011. One of the major assumptions of the MTLW is that the

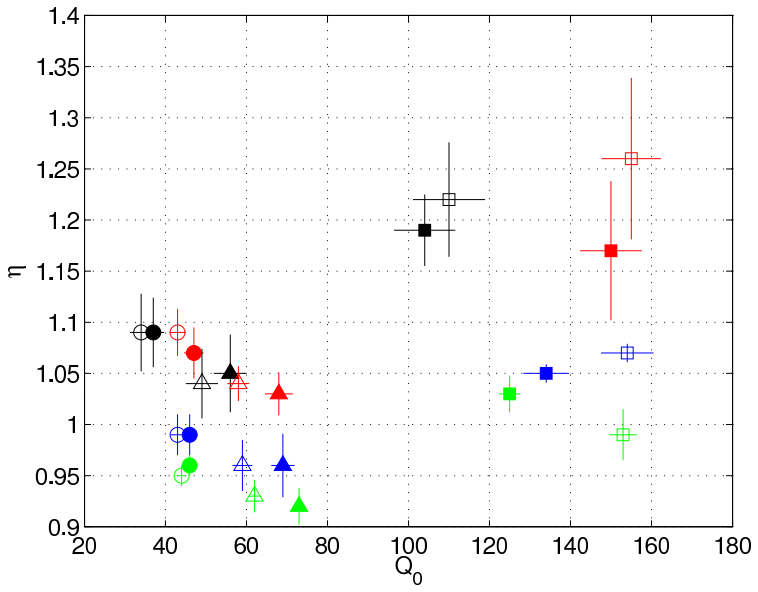

Figure 5.8: Summary of results using the MTLW for different depth ranges for the model $Q(f) = Q_0 f^{\eta}$ for frequencies $3 \leq f \leq 15\,Hz$. Solid markers indicate the results obtained using an infinite medium while open markers correspond to a two-layer model. Depth ranges are color-coded: Black $0 \leq depth \leq 20\,km$; red $0 \leq depth \leq 40\,km$; blue $0 \leq depth \leq 100\,km$; and green $20 \leq depth \leq 100\,km$. Type of attenuation is indicated by the shape of the markers: Total attenuation $Q_{Tot}(Q_0, \eta)$ circles; intrinsic attenuation $Q_{Int}(Q_0, \eta)$ triangles; and scattering attenuation $Q_{Sct}(Q_0, \eta)$ squares.

geometrical spreading is proportional to r^2. Although this condition is satisfied in the simulations, observed data shows a particularly complex geometrical spreading as pointed out by Morozov 2008. As wavefronts approach the surface, impedance contrast, faulting and sedimentary basins can dramatically change the mode of propagation. To test this hypothesis, we choose the station CAIG from the permanent network and assume that the geometrical spreading exponent of the data can freely vary while keeping the intrinsic attenuation constant at $Q_i = 1000$ as suggested by Margerin et al. 1999. Therefore, Eq. 4.31 can be

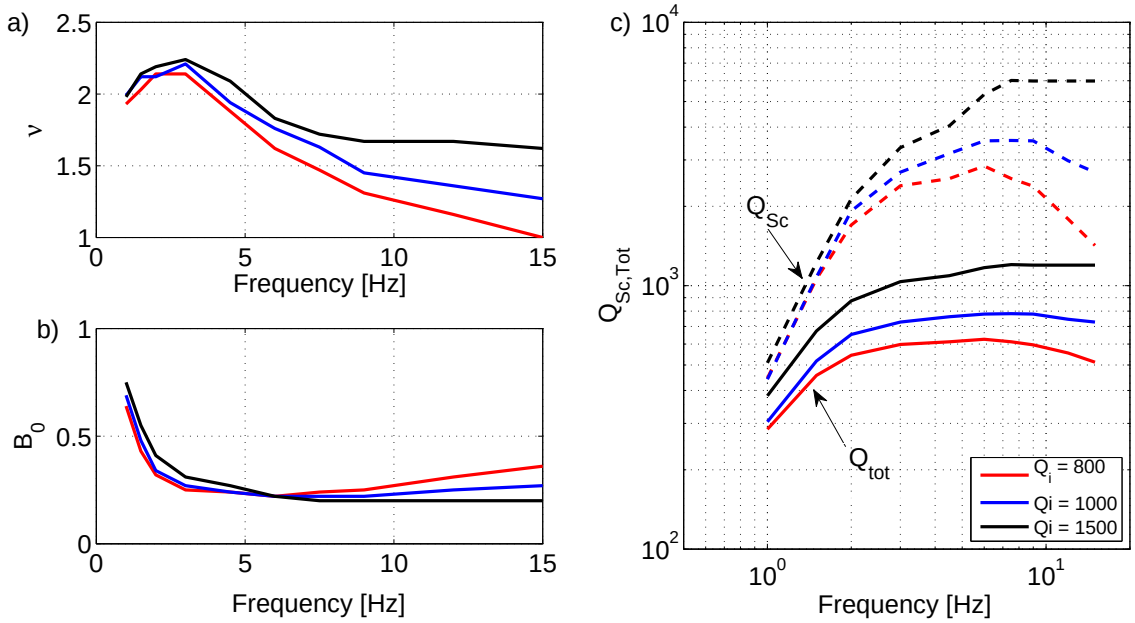

Figure 5.9: Results obtained for the station CAIG using a modified version of the MTLW method. a) Shows the predicted geometrical spreading exponent η that best correct the data. b) Shows the seismic albedo. c) Summarizes the results for total attenuation Q_{tot} solid lines, and scattering attenuation Q_{Sc} dotted lines.

rewritten as

$$\pi(2r)^{\nu}E_t(r) = \exp\left[-\left(g + \frac{\omega}{Q_i^{fix}v}\right)r\right] + 4\pi r^2 \frac{v}{W_0}\int_{r/v}^{r/v+T_0} E_s(r,t)\exp\left(-\frac{\omega t}{Q_i^{fix}}\right)\,dt. \quad (5.3)$$

Where η is the geometrical spreading factor and Q_i^{fix} is the a priori solution for the intrinsic attenuation. Thus, the space of solution is determined by the pair (B_0, ν). By allowing the geometrical attenuation to be variable, we relax the constraints on the extinction length while keeping the seismic albedo relatively unaltered. Figure 5.9 shows the results of inverting the data for station CAIG using the model in Eq. 5.3. We assume three values of frequency independent intrinsic quality factor $Q_{In}^{fix} = \{800, 1000, 1500\}$. In all cases the solution converges to fit the data independently of the selection of Q_{In}^{fix} in the range of $1 \leq f \leq 6\,Hz$. At higher frequencies ($f \geq 6\,Hz$), the solution diverges, resulting in poorer fits.

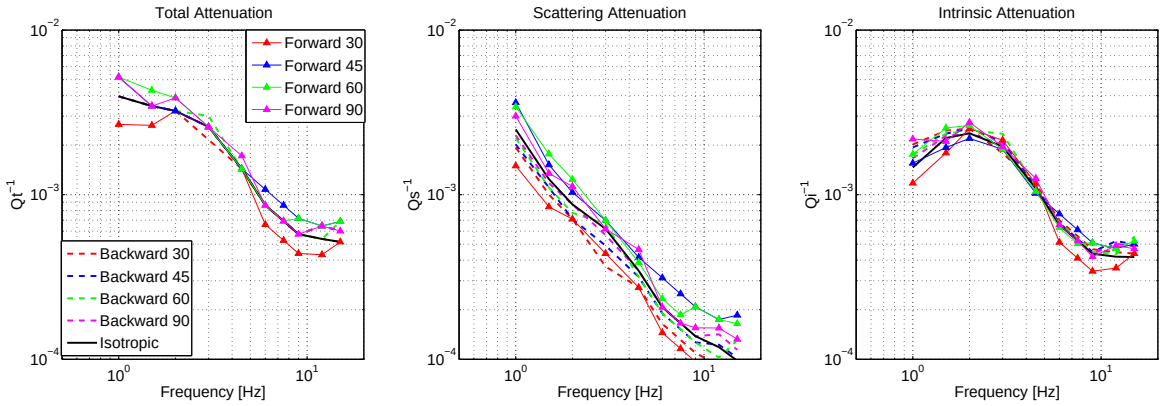

Figure 5.10: Separation of intrinsic and scattering attenuation using different models of scattering for station CAIG. (left) Intrinsic attenuation Q_{In}^{-1}, (middle) scattering attenuation Q_{Sc}^{-1}, (top) total attenuation Q_{Tot}^{-1}.

Assuming that the intrinsic attenuation is constant in the range of $800 \leq Q_{In} \leq 1500$ leads to geometrical spreading factors larger than 2 for frequencies lower than $f \leq 4.5\,Hz$. On the other hand, for greater frequencies, $f \geq 4.5\,Hz$, geometrical spreading decays towards more cylindrical-like modes. This suggests that, at these frequencies, trapping into upper layers better explains the coda decay.

5.7 The role of assuming the preferential mode of propagation

The present models of coda based on the radiative transfer theory assumes that scattering is isotropic and lies in the Rayleigh regime. First scattering models (Aki 1969; Aki and Chouet 1975) described coda as the result of backscattering in the medium. Nonetheless, we will show in the next Chapter that coda waves coming immediately after the main body phase are made of mostly of forward scattered waves. Therefore, the common backscattering propagation mode is likely constrained to a minimum source-receiver distance as a function of the wavelength. Figure 5.10 shows the results of separating intrinsic and scatter-

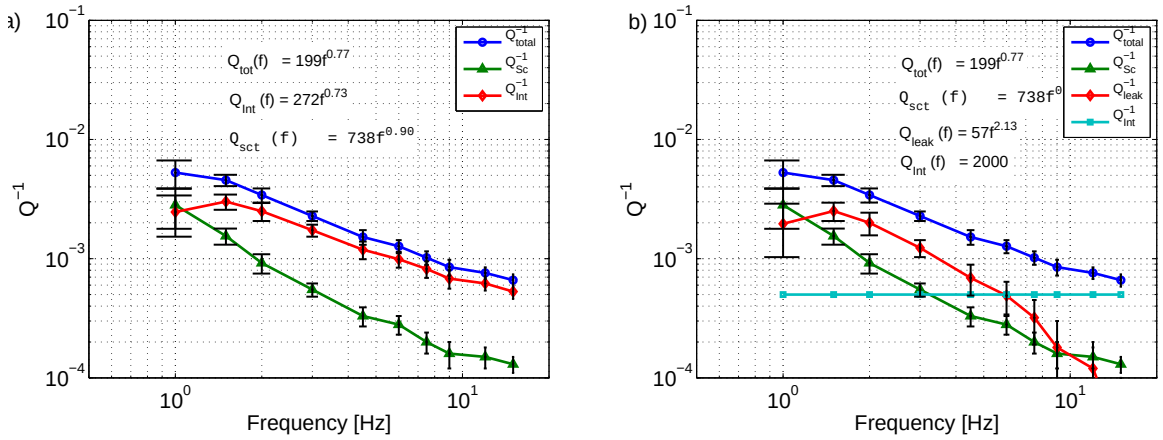

Figure 5.11: Reinterpretation of the results for station CAIG. a) Results for the direct application of the MLTW method. b) Results assuming that the intrinsic attenuation is independent of frequency and leakage of energy towards the mantle according to Eq. 5.4.

ing attenuation using alternative non-isotropic models of propagation. Synthetic envelopes were obtained as shown in Section 4.6 with the only difference that scattering angles are not longer uniformly distributed on a spherical surface but in a Gaussian volume centered at the incident angle. We consider two extreme cases, when the particles follow forward and backward trajectories. We observe that the selection of the model has little influence in the estimates of intrinsic and total attenuation. Narrow angles of either forward or backward scattering lead to lower scattering attenuation Q_{Sc}^{-1} values compared to the isotropic case. The opposite occurs for wide scattering angles. Interestingly, intrinsic attenuation curves Q_{Int}^{-1} shows a 'S' shape form regardless of the selection of the model. We prepose that this effect can be explained by leakage of energy towards the mantle at low frequencies, and trapping of higher frequencies towards the surface.

5.8 Reinterpretation of the results

Application of the MTLW yields low values of intrinsic attenuation with a high frequency dependance. As suggested by (Margerin et al. 1999) and (Davis and Clayton 2007), the intrinsic quality factor should be of the order of $Q_{In} \sim 1000$ and frequency independent. A possible way to reconcile this observation is by adding an additional exponential decay to the second term of the Eq. 4.31 to account for energy losses caused by leakage towards the mantle. Therefore, a modified model of the MTLW can be rewritten as,

$$4\pi r^2 E_t(r) = \exp\left[-\left[g + \frac{\omega}{v}\left(\frac{1}{Q_{Int}} + \frac{1}{Q_{leak}}\right)\right] r\right] + 4\pi r^2 \frac{v}{W_0} \int_{r/v}^{r/v+T_0} E_s(r,t) e^{-(Q_{Int}^{-1}+Q_{leak}^{-1})\omega t}\, dt. \tag{5.4}$$

This model states that leakage of energy is included into the the estimates of the intrinsic attenuation. Therefore, we reinterpreted our results by keeping the geometrical spreading constant and assuming the intrinsic attenuation. Figure 5.11 shows the results obtained by reinterpreting station CAIG. The left panel shows the results obtained by direct application of the MTLW while the right panel shows the reinterpretation of the results assuming that the intrinsic attenuation is $Q_i = 2000$. We observed strong leakage of energy at frequency between $1 \leq f \leq 4.5\,Hz$ which becomes negligible at higher frequencies $f \geq 4.5\,Hz$.

5.9 Conclusions

Analysis of the scattering properties of the Middle America region at high frequencies ($> 1Hz$) shows consistent results in both directions of propagation perpendicular and parallel to the trench. We applied the MLTW method to two orthogonal profiles. The first profile consists of twenty five temporary stations aligned perpendicular to the trench. The second profile extends along the coast and is consists of four permanent stations. For the array of temporary stations, the solution space (B_0, Le^{-1}) shows consistent results between stations ACAP and PETA at all frequencies. At low frequencies ($\leq 3\,Hz$), the northernmost stations

(UICA to MAXE) show higher values in the estimates of seismic albedo and lower values for the extinction. These difference can be explained through two possible mechanisms: 1) a change in the near surface lithology, and 2) bias of the results due to low signal to noise ratios. For the northern stations, short range events ($d \leq 70\,km$) show smaller magnitudes compared to the thrust events in the vicinity of the trench. This results in lower signal to noise ratios in addition to the higher attenuation expected at low frequencies.

Differences in attenuation are more prevalent in the estimation of the scattering attenuation Q_{Sc}^{-1} between the profile perpendicular and the profile along the coast. For the stations along the coast, scattering attenuation is smaller compared to the profile perpendicular of the trench. This can be explained by the wedge-type shape of the crust near to the trench that causes changes in either the mode of propagation or the distribution of heterogeneities. The selection of the synthetic model used in the calculation of the energy curves produces small variations in the estimates of the parameter Q_0. The two-layer model results in higher values of ${}_{Tot}Q_0$ compared to the infinite medium. The opposite case occurs for the estimates of ${}_{Int}Q_0$ and ${}_{Sc}Q_0$ where the infinite model gives rise to slightly higher values. These differences are not statistically significant for the intrinsic and total attenuation parameters, but have a stronger influence for the estimates of seismic albedo and consequently scattering attenuation. On the other hand, estimates of the parameter η lie above unity (e.g. $\eta \approx 1.2$) in the case of the scattering attenuation for crustal events ($depth \leq 40\,km$). While for the rest of the cases, the estimates of η are close to unity. As suggested by Morozov 2009, this is an indicator that attenuation factor is frequency independent. This is supported by the fact that the variables (B_0, Le^{-1}) converge to constant values for frequencies above $3\,Hz$.

Examination of the role of assuming the intrinsic attenuation and geometrical spreading shows the limitations of the MLTW method. By fixing the intrinsic attenuation and solving by the geometrical spreading yield to high values of the geometrical spreading factor $\eta \geq 2$. This is physically possible if the velocity increases as a function of depth which causes bending of the rays towards the surface, but leads to underestimate results at higher

frequencies. This suggests that the common assumption of spherical geometrical spreading may be constrained to a specific range of frequencies and distances. Another alternative model to reconcile these observations is by considering the leaking of energy towards the mantle. Reinterpretation of the results shows that leakage has an important contribution to the total attenuation for frequencies between $1 \leq f \leq 15\,Hz$. Lastly, the fact that the classification of the events into different depth ranges produces small variations in the results suggest that the near surface attenuation dominates the average value of Q over the crustal volume. This is in agreement with the hypothesis that most of the attenuation and scattering is concentrated towards the surface.

CHAPTER 6

Evaluation of seismic scattering using an alternative seismic network

6.1 Introduction

Modeling of scattered waves in the crust has been highly controversial in the past 40 years. From the initial models of back- scattering proposed by Keiiti Aki in 1969; to the recent models of scattering based on kinetic theory of gases. Different groups have relied on a priori assumptions about the medium, the mode of propagation and the physics of the rocks. These constraints have leaded to a large variety of models with significant differences in the phenomenological basis with an apparent success fitting the data. Perhaps one of the major hurdles to achieve a unifying theory lies in the sparse nature of the current seismic networks. A novel experiment deployed by Nodal Seismic provides an unprecedented set of data to analyze scattered wavefields at high frequencies and short wavelengths. A set of 5000 seismic instruments, spaced every $100\,m$, was installed for a period 6 months in the Long Beach area in southern California to mainly image the geological structure of the area for oil exploration purposes. Nonetheless, our interest focuses on the examination of coda waves and their statistical and physical properties. In the first instance, we compute the frequency-wavenumber diagrams as a function of time to detect the sources of coda and their evolution in time. In addition, we analyze the entropy of the network as seismic waves propagate through the array. Entropy marks the transition between the coherent direct body

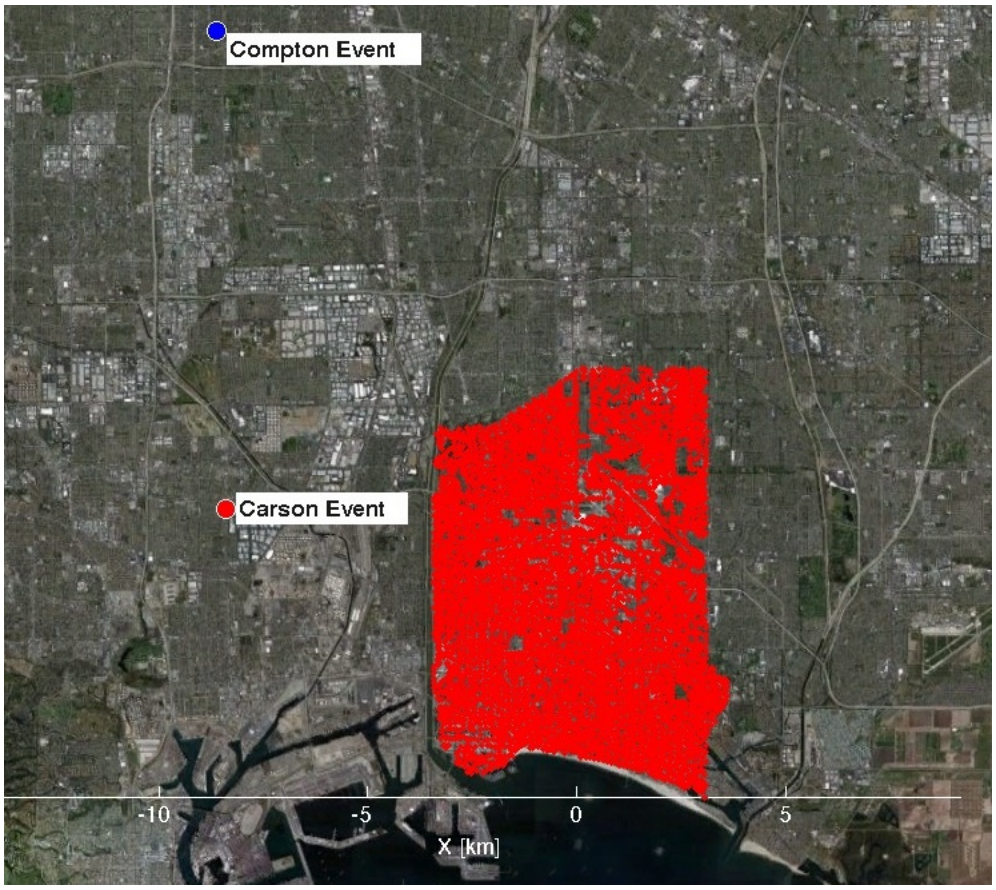

Figure 6.1: Location of the stations deployed in Long Beach (red dots) and the Mw = 2.5 Carson event and the Mw = 3.4 Compton event.

waves and the onset of coda waves. This result suggests that the seismic record is mostly dominated by forward scattered body waves for a time comparable to the arrival of the *S*-wave before the transition to omnidirectional coda waves occurs.

6.2 Data

Seismic records from two local events are analyzed. The first event occurred on Friday, May 13, 2011 at 9:19:00 PM (Local Time), in the city of Carson (Hereafter Carson Event) west of the seismic array. The magnitude and depth reported by USGS are Mw=2.5 and

10km, respectively. The second event occurred NW of the network on Monday, June 6, 2011 at 0:09:10 AM (Local Time) in the city of Compton (Hereafter Compton event). The magnitude and depth reported by USGS are Mw=3.4 and 24.4 km. The Carson event is one order of magnitude smaller than Compton and occurred at quieter time of the day, Friday night. Nonetheless, urban noise is clearly observed in either case. Additionally, each event had significant differences in depth (10 and 24 km). Therefore, they are used to examine the crustal structure and near surface effects caused by faulting and layering. The number of stations processed in each analysis varies between 150-5000 according to the frequency of interest. Data was downsampled from 500 Hz to 100 Hz to accelerate the processing. Figure 6.1 shows the location of the stations and the events analyzed.

6.3 *fk* analysis

The frequency wavelength (*fk*) analysis (Rost and Thomas 2002) is a common tool in seismology used to determine the orientation and apparent slowness/velocity of the incident field. This technique consists basically in stacking the seismic records at different reduced times depending on the relative location of the station and a set of test values for the apparent slowness and azimuth. Thus, the stacked signal is calculated as,

$$y(t) = \frac{1}{N}\sum_{i=1}^{N} x_n(t - \mathbf{u}\cdot\mathbf{r_n}). \tag{6.1}$$

Where N is the total number of seismogram (stations), and n indicates the receiver index. $\mathbf{r_n}$ is the relative location of the stations where the origin is set to the center of the array. $\mathbf{u}$ is the apparent slowness defined as,

$$\mathbf{u} = \frac{1}{v}(cos(\theta), sin(\theta)). \tag{6.2}$$

Where v is the apparent velocity and θ is the azimuth. The amplitude of the stacked signal $y(t)$ is maximum when the individual records align coherently for a specific pair (v, θ).

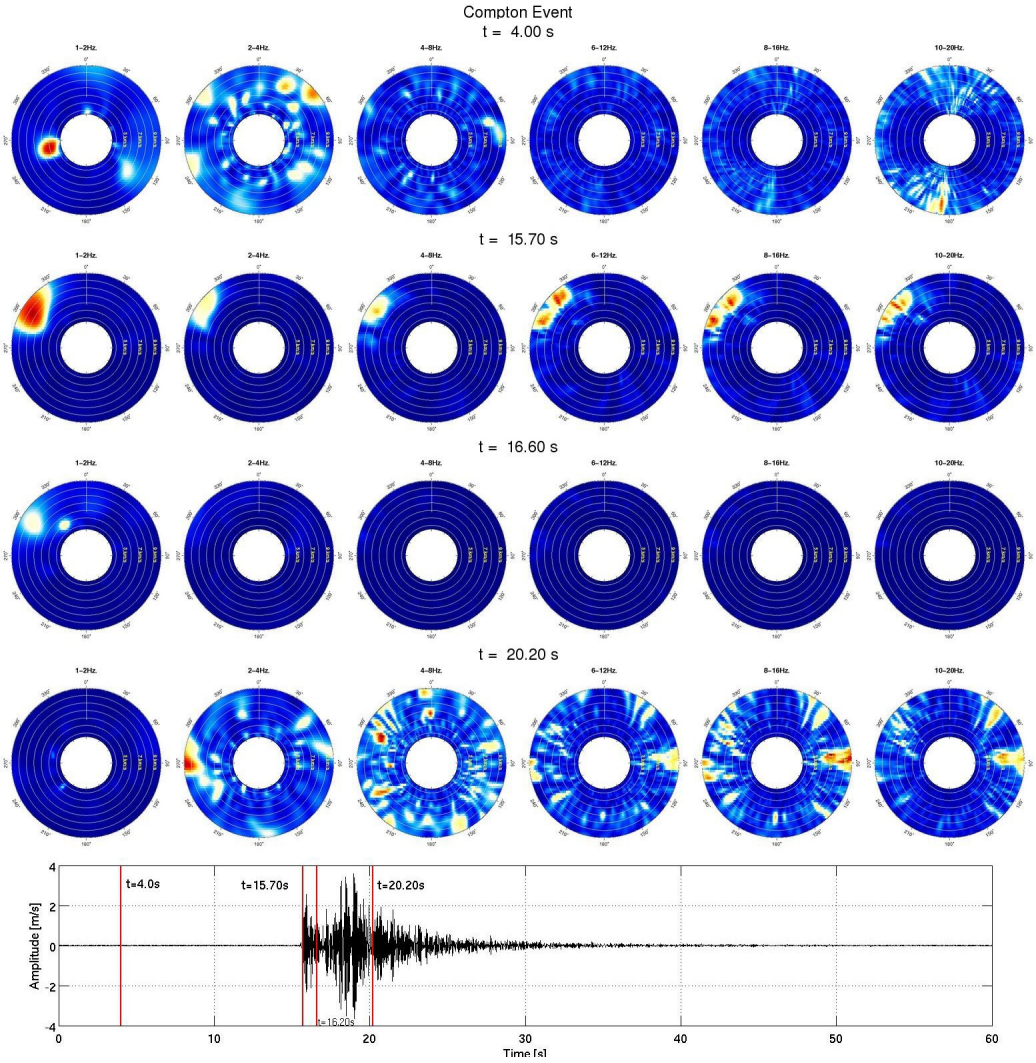

Figure 6.2: Snapshots of the *fk* analysis for the Compton event. Rows show the *fk* analysis at constant time for different frequencies (columns). The bottom panel shows a sample seismogram for a station located roughly in the middle of the array indicating the times at which the *fk* analysis is computed.

Stacking is carried out in a limited 3s window to examine the time variation of the seismic wavefield. Hence, the energy of the stacked signal is computed as,

$$E(t) = \int_{t}^{t+D} y^2(t)dt \tag{6.3}$$

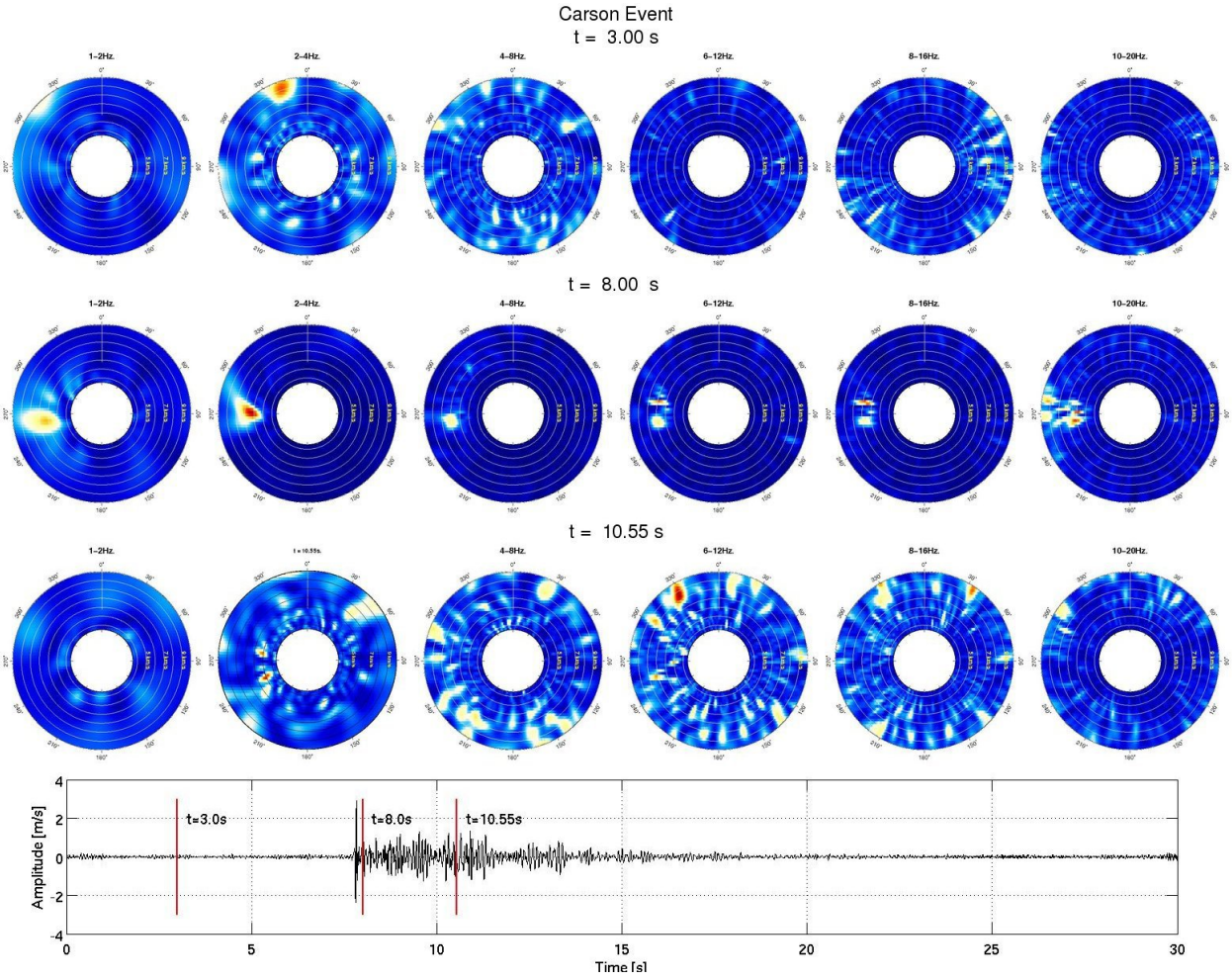

Figure 6.3: Snapshots of the *fk* analysis for the Carson event. Rows show the *fk* analysis at constant time for different frequencies (columns). The bottom panel shows a sample seismogram for a station located roughly in the middle of the array indicating the times at which the *fk* analysis is computed.

where D is the width of the time window. Therefore, the parameter $E(t)$ is a measure of the strength of the stacked signal. Interestingly, two strong signals come up in the *fk* analysis for the Compton event at $16.60s$ (Fig. 6.2). An anomalous signal is clearly seen in the frequency band $1-2Hz$, and $2-4Hz$. The strongest arrival detected shows an apparent velocity of $\sim 8km/s$ and an azimuth of $\sim 300°$. A secondary wave appears slightly later in time with

a slower apparent velocity $\sim 5km/s$ and azimuth $\sim 320°$. The first signal corresponds to the arrival of the S- waves however the second signal appears unexpectedly. Two possible scenarios can explain this phase. An aftershook event that might have occurred within a few seconds after the main event which signal is mostly hidden by the main event. Other possibility is the existence of a steep dipping structure that diffracted a significant part of the direct energy. Near horizontal angles of diffraction may explain the change in apparent velocity as well as the azimuthal direction. A similar anomalous signal is not observed for the Carson event (See Fig. 6.3). In this case the transition between direct and coda waves occurs within a few seconds after the arrival of the S- as suggested by the entropy analysis described in the next section.

6.4 Entropy Analysis

Entropy is a measure of the randomness of the system. It appears in a variety of fields such as information theory, statistical mechanics and thermodynamics. Until now, very little research had been done analyzing the entropy of a seismic network. Thanks to the high spatial density of the network, it is possible to analysis the entropy transitions of the seismic wavefield as it moves through the array. I use the definition of entropy $H(x)$ often found in information theory studies,

$$H(x) = -\sum_{i=1}^{n} p(x_i) \log_b p(x_i). \tag{6.4}$$

In this case, x is the state and $p(x)$ is the probability of a given state. Entropy is maximum when the probably of any state x_i is equally probable. Seismograms are discrete representations of the velocity of the wavefield as a function of time. In order to explore the entropy of the network, I will consider two possible states ($n = 2$) of the seismograms either positive or negative (the zero state is neglected). In this first approximation, the amplitude information will be lost as a result of the binarization of the signal. The next step consists in

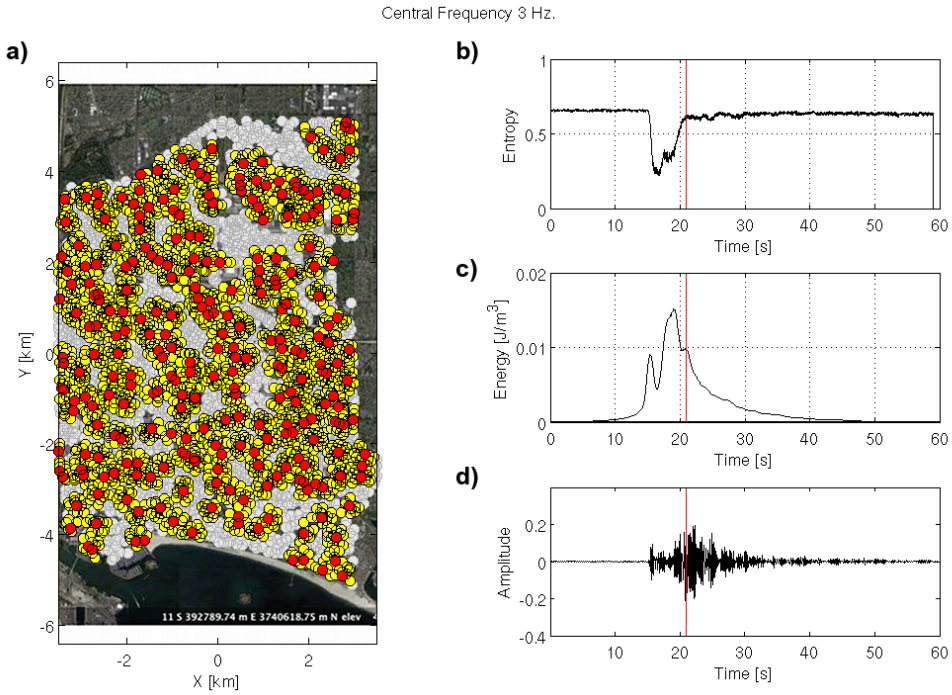

Figure 6.4: Entropy-energy analysis. a) Shows the map and classification of the stations. Red circles show the central stations; stations in yellow indicate the neighbor stations in a radius of 250 m; gray circles are station not used in this computation. b) Shows the average energy computed using Eq. 6.3; c) is the energy of the window; and d) is a sample seismogram randomly chosen from the network. The red line marks the transition from coherent arrivals to noise-like random state.

subdividing the array into sub-networks. Figure 6.4 shows the entropy-energy analysis for the Compton event in the band $1-4\,Hz$ (central frequency $3Hz$). Fig. 6.4a shows the map of the stations and the classification of the stations. Red circles indicate what I define as central stations; yellow circles are the neighbor stations in a radius of 250m from the central station; and gray circles are stations not used in this calculation. Each neighborhood has on average 14-16 stations. Then, we determine the entropy by estimating the probability of each state by simply counting the number of positive/negative states and dividing by the

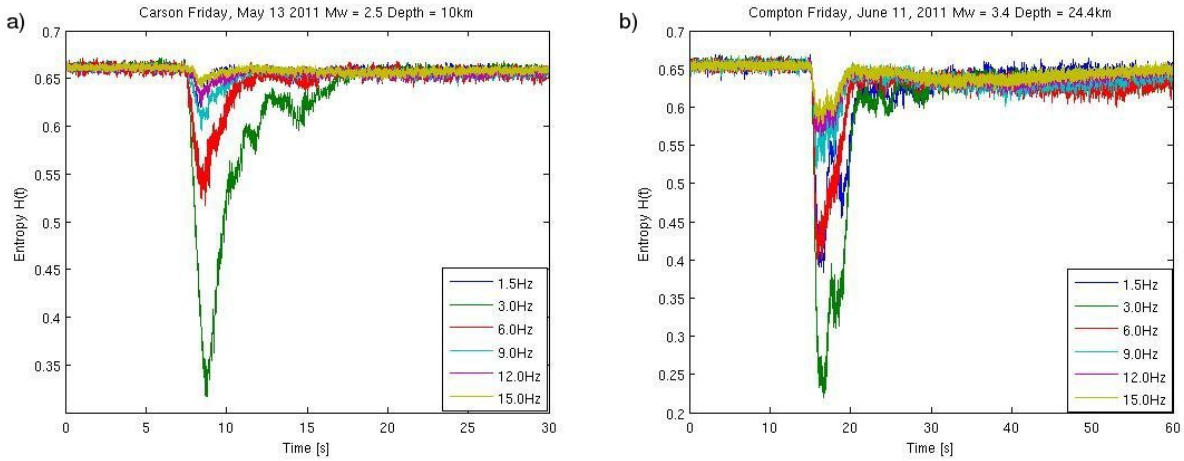

Figure 6.5: Entropy as a function of time for different frequency bands. a) Carson event, and b) Compton event.

number of stations in the neighborhood. This calculation is repeated in each neighborhood and then averaged for the entire array. Figures 6.4b,c,d show the entropy, the average energy and a sample seismogram randomly chosen, respectively. Finally, Figure 6.5 shows the entropy analysis at different frequencies: 1.5, 3.0, 6.0, 9.0, 12.0 and 15 Hz for both events. The number of stations used at each calculation is increased for high frequencies to ensure a stable result. I observed that the largest entropy drop for both events occurs at 3.0 Hz, this value is probably related to a natural frequency of the Long Beach basin. Perhaps the most interesting result so far lies in the fact that the entropy comes back to noise level at about twice the lapse time (arrival of the S- wave). This marks the transition point at which seismic waves become incoherent and the beginning of coda waves. Note that the energy levels are still above the noise levels while the noise and coda entropy become indistinguishable. This conclusion is reproducible for both events despite the fact that the Carson event is one order of magnitude smaller than the Compton event.

6.5 Conclusions

Analysis of the scattered wavefield in Long Beach suggest that the coda contains coherent waves until twice the lapse time after which isotropic scattering is the major contributor to the coda wave field. The *fk* diagrams show the distribution and evolution in time of the incoming energy at frequencies between $1 \leq f \leq 20\,Hz$. Shortly after the pass of the *P*- and *S*- waves, body waves lose their coherency and coda waves take over the spectrum mostly at intermediate frequencies $2 \leq f \leq 12\,Hz$. Interestingly, the *fk* analysis of the Compton event shows a strong secondary phase soon after the *S*- wave arrival at low frequencies $1 \leq f \leq 4\,Hz$. This phase is likely linked to the geometry of the basin and the fault zone North of the array. A similar phase is not observed for the Carson event that suggests that a strong path effect modifies the NW-SE trajectory. On the other hand, the entropy-energy analysis reveals the transition point between direct coherent body waves and incoherent coda waves. Entropy is used as an indicator of the randomness of the wavefield and coherency between nearby stations. A drastic drop in entropy occurs when direct body phases propagate through the array. As coda waves build up, entropy returns to the level prior to the earthquake despite the fact that the energy contained in the wavefield is significantly above the noise level. For both events, entropy shows a strong frequency dependence that peaks around $3\,Hz$.

CHAPTER 7

Conclusions

This work examines the scattering properties of the Middle America Region. In particular, I focus on the effect that the tectonic setting has on the propagation of seismic waves. To accomplish this goal, I explored the scattering effects in a broadband sense ($0 \leq f \leq 20\,Hz$). Using teleseismic events, I analyzed the influence that lateral and vertical discontinuities have on the propagation of low frequency body waves ($0 \leq f \leq 1\,Hz$). In addition, analysis of the envelopes of local events provided insight into the scattering properties of the crust at higher frequencies ($1 \leq f \leq 15\,Hz$). The principal criterion for this apparent arbitrary classification lies on the selection of the ratio between the wavelength and the characteristic length of the discontinuities of interest, ka. For teleseismic events, dimensional analysis suggests that changes in the mode of propagation of teleseismic body waves lies on the Mie scattering regime. This regime is characterized by scattering in the forward direction due to changes in the properties of the medium with characteristic scale comparable to the wavelength of the incident field ($0.1 \lesssim ka \lesssim 10$). In the next case, for local events, heterogeneities in the crust have in general a characteristic length significantly smaller than the dominant wavelength ($0.01 \lesssim ka \lesssim 0.1$) . Under these conditions, scattering at higher frequencies due to small heterogeneities lies primarily in the Rayleigh regime whose preferential mode of propagation of the scattered wavefield is isotropic.

Chapter 2 presented the motivation to explore the scattering properties of the Middle America region. In this chapter, I highlight the major geological and geophysical findings in this area, and the current challenges faced by the seismological community. The main distinctive

feature of this area from the tectonic point of view is commonly related to the flat subducting geometry of the slab. Not only the seismic activity of the area is highly influenced by this 'atypical' geometry, but also the propagation of seismic waves is dramatically affected.

In Chapter 3, I documented the effect that the transition between the continental-oceanic crust and the flat subducting slab has on the propagation of seismic waves. Analysis of the seismic records using tau-p and *fk* transforms revealed a secondary field that branches off specific body phases that hit the trench from the ocean side at wide angles. This observation is not seen ubiquitously, trapping of body waves occurs under a specific combination of incident angles and distance to the trench. A total of seven teleseismic events with magnitudes larger than $Mw \geq 7.0$ occurred in the southern hemisphere which showed clearly visible scattered fields following the phases *SS*, *SP*, and *PS*. These events lie within a distance range of 70 to 112° from the trench and a backazimuth of $150 - 250°$. These conditions result in favorable incident angles which excite the trench acts as a quasi-linear source that generates trapped surface waves that propagate with little attenuation. This conclusion is supported by numerical simulations which reproduced the major propagating features of the scattered field.

Chapter 4 provides a review of the models of scattering at high frequencies and discusses the separation of intrinsic and scattering attenuation. It is widely accepted that coda waves are the result of the randomness in the elastic properties of the crust, but their numerical representation is an active area of current research. Despite of the fact that several models have successfully modeled several features of the seismic envelope and coda decay, a unified model that can reproduce the statistical characteristic of the coda waves is still missing. I describe in detail one of the proposed methods for the separation of intrinsic and scattering attenuation known as Multiple Lapse Time Window (MLTW) method (Hoshiba et al. 1991). This method assumes that the envelopes of the seismograms can be reproduced synthetically by assuming that the crust is filled up with point-like scatters which radiate energy isotropically when excited by an incident field.

In Chapter 5, I presented independent estimates of intrinsic and scattering attenuation for two perpendicular profiles in Mexico. Results obtained by direct application of the MLTW method, suggest that for frequencies higher than $f \geq 3\,Hz$, $\sim 30\%$ of the total attenuation is the due to the redistribution of energy in the crust. At lower frequencies, attenuation estimates show a significant frequency dependence in the estimates of total attenuation and seismic albedo (ratio between scattering and total attenuation) with a relatively frequency independent intrinsic Q_i^{-1}. By assuming a spherical geometrical spreading, we obtained intrinsic attenuation curves with a strong frequency dependance for frequencies $f \geq 3\,Hz$. This result is counterintuitive, several studies (Davis and Clayton 2007; Margerin et al. 1999; Morozov 2008; Jackson et al. 2008) suggest that intrinsic attenuation is frequency independent in the frequency range of $1 \leq f \leq 20\,Hz$. Therefore, I analyzed the consequences of assuming frequency independent intrinsic attenuation. In the first instance, we assume that the intrinsic attenuation is frequency independent and that the geometrical spreading can vary as function of frequency, we obtained high values of the the geometrical spreading factor ($\eta > 2$) in the frequency range of $1 \leq f \leq 3Hz$ and a steady decay towards a cylindrical mode of propagation ($\propto r$) at higher frequencies $f \geq 3\,Hz$. In order to reconcile the discrepancies among different models of scattering and the MLTW, we proposed adding an additional exponential decay to the scattering component of the energy to account for the energy leakage into the mantle. This extra term allows us to keep the intrinsic attenuation frequency independent and to consider the layered structure of the media. Moreover, classification of the events according to the depth showed consistent results regardless of the selection of the events. This result suggests that most of the attenuation by scattering is mainly generated in the upper part of the crust which it is in agreement with boreholes studies in southern California and Japan (Adams and Abercrombie 1998; Kinoshita 2008). Lastly, convergence of the exponential factor η towards the unit suggests a possible bias of the frequency dependance of the results.

In Chapter 6, I analyzed a proxy set of data for the evaluation of earthquake coda waves at frequencies between $1 \leq f \leq 15\,Hz$. The vast majority of seismic studies are commonly limited by sparse instrumentation. Nonetheless, an oil exploration project deployed in Long Beach, California provides one the most dense seismic arrays ever available to the seismological community. Data for two local events from an array of $\sim 5,000$ stations spaced every $\sim 100\,m$ show the evolution in time of the scattered wavefield. The beamforming analysis of the data shows the transition between the forward scattered direct phases and the rising of coda waves. An interesting path effect observed in the analysis of the Compton event (a $Mw = 3.4$ event occurred $24\,km$ Northwest of the array) shows a strong secondary field that rises after the arrival of the S- wave. This phase has a lower apparent velocity ($5\,km/s$) compared to the incident field ($9\,km/s$) and has a slightly different incident back azimuth ($\delta\theta \approx 10°$). This secondary wavefield is analogous to the trapped crustal phase observed in Mexico but at a much smaller scale length. Similarly, it is extremely dependent on the trajectory of the incident field and is likely due to trapping in a near to the surface low velocity structure such as the basin. After forward scattered waves pass through the network isotropic coda waves develop as a result of scattering from small-scale heterogeneities in the medium. Entropy analysis of the network suggests that the wavefield becomes incoherent at roughly twice the time of the arrival of the S- wave. Interestingly, entropy levels of the coda waves are very similar to the entropy before the event even though the energy of the coda waves is significantly greater than the noise.

Analysis of the scattering properties in central Mexico and Long Beach, California, provided a vast set of data to test several of the models of scattering. Mexico shows that low frequency body waves from teleseismic events are greatly affected by the geometry of the subducting slab and the transition between the ocean and the continent at the trench. It is also found that discrepancies between the proposed models of intrinsic attenuation cannot be resolved by simply changing the geometrical spreading. This result implies that the layering nature of the tectonic region needs to be included in order to determine the intrinsic attenuation.

In addition, the Long Beach seismic experiment questions the hypothesis that coda waves build up immediately after the arrival of the direct waves. A transition between the forward coherent scattering and isotropic random scattering model is more likely to occur after a lapse time beyond the arrival of the body waves.

Summarizing, results obtained in this work shows the scattering effects of the Middle America Region at different length scales. Forward scattering (Mie Regime) was clearly observed at two distinctive scale lengths: 1) At continental level in the case of scattered waves from the Middle America trench trapped in the crust, 2) at a local scale in the case of forward scattered waves in Long Beach and trapping near the surface. This conclusion has important implications for the modeling of coda waves using Radiative theory models which usually assume that coda waves built up immediately after the arrival of the S- waves, and that the preferential mode of propagation is isotropic even for early parts of the coda. In addition, analysis of the factors that determine the attenuation suggest that trapping and leakage of energy trade-off in the estimates of attenuation. High frequencies ($f \gg 1\,Hz$) near the surface are more likely to get trapped at low velocity layers while low frequencies ($f \sim 1\,Hz$) traveling towards the mantle get absorbed into the mantle. Estimates of seismic risk rely on the correct estimation of the attenuation in a given area. This work developed an alternative model of attenuation which reconciles the present models of scattering using radiative transfer theory, and laboratory experiments. Additionally, seismic observations presented here cast light on the missing elements that could be included in future work for the implementation of enhanced models of propagation in heterogenous media.

Bibliography

Abercrombie, R. E. (1997). Near-surface attenuation and site effects from comparison of surface and deep borehole recordings. *Bull. Seism. Soc. Am. 87*(3), 731–744.

Abercrombie, R. E. (2000). Crustal attenuation and site effects at Parkfield, California. *J. Geophys. Res-Sol Earth 105*(B3), 6277–6286.

Abers, G. A., K. Fischer, M. Protti, and W. Strauch (2007). The TUCAN broadband seismimeter experiment: Probing mantle meeting in the nicaragua-costa rica subduction zone. *IRIS Newsl. 1*, 10–12.

Abubakirov, I. and A. Gusev (1990). Estimation of scattering properties of lithosphere of Kamchatka based on Monte-Carlo simulation of record envelope of a near earthquake. *Phys. Earth Planet. In. 64*, 52–67.

Adams, D. A. and R. E. Abercrombie (1998). Seismic attenuation above 10 Hz in southern California from coda waves recorded in the Cajon Pass borehole. *J. Geophys. Res. 103*(B10), 24,257–24,270.

Aki, K. (1969). Analysis of seismic coda of local earthquakes as scattered waves. *J. Geophys. Res. 74*(2), 615–631.

Aki, K. (1980a). Attenuation of shear-waves in the lithosphere for frequencies from 0.05 to 25 Hz. *Phys. Earth Planet. In. 21*, 50–60.

Aki, K. (1980b). Scattering and attenuation of shear-waves in the lithosphere. *J. Geophys. Res. 85*(B11), 6496–6504.

Aki, K. and B. Chouet (1975). Origin of coda waves - source, attenuation, and scattering effects. *J. Geophys. Res 80*(23), 3322–3342.

Aki, K. and P. G. Richards (1980). *Quantitative Seismology - Theory and methods*, Volume 1 and 2. W. H. Freeman.

Akinci, A. and H. Eyidoğan (2000). Scattering and anelastic attenuation of seismic energy in the vicinity of north anatolian fault zone, eastern Turkey. *Phys. Earth Planet. In. 122*(3-4), 229 – 239.

Akinici, A., E. Del Pezzo, and M. J. Ibáñez (1995). Separation of scattering and intrinsic attenuation in southern Spain and western Anatolia (Turkey). *Geophys. 121*, 337–353.

Alaniz-Álvarez, S. A., S. A. Nieto-Samaniego, and L. Ferrari (1998). Effect of strain rate in the distribution of monogenetic and polygenetic volcanism in the Transmexican volcanic belt. *Geology 26*(7), 591–594.

Anderson, J. G., P. Bodin, J. N. Brune, J. Prince, S. Singh, R. Quaas, and M. Onate (1986). Strong ground motion from the Michoacan, Mexico, earthquake. *Science 233*(4768), 1043–1049.

Anderson, J. G. and R. Quaas (1988). The Mexico earthquake of September 19, 1985-Effect of magnitude on the character of strong ground motion: An example from the Guerrero, Mexico strong motion network. *Earthquake Spectra 4*(3), 635–646.

Aranda-Gómez, J. J., J. F. Luhr, T. B. Housh, G. Valez-Moreno, and G. Chávez-Cabello (2007). Late Cenozoic intraplate-type volcanism in central and northern Mexico. In S. A. Alaniz-Álvarez and S. A. Nieto-Samaniego (Eds.), *Geology of Mexico: Celebrating the Centenary of the Geological Society of Mexico*, Number 422. The Geological Society of America.

Astiz, L. and H. Kanamori (1984). An earthquake doublet in Ometepec, Guerrero, Mexico. *Phys. Earth Planet. In. 34*, 24–45.

Atwater, T. (1970). Implications of plate tectonics for the Cenozoic tectonic evolution of western North America. *Geol. Soc. Am. Bull. 81*, 3513–3536.

Atwater, T. and J. Stock (1998). Pacific North America plate tectonics of the Neogene southwestern United States: An update. *Int. Geol. Rev. 40*(5), 375–402.

Audet, C. J., M. G. Bostock, N. I. Christensen, and S. M. Peacock (2009). Seismic evidence for overpreassured subducted oceanic crust and megathrust fault scaling. *Nature 457*, 76–68.

Badi, G., E. Del Pezzo, M. Ibáñez, M. J., F. Bianco, N. Sabbione, and M. Araujo (2009). Depth dependent seismic scattering attenuation in the Nuevo Cuyo region (southern central Andes). *Geophys. Res. Lett. 36*, L24307.

Bandy, W. L., V. Kostoglodov, and C. Mortera-Gutierrez (1998). Southwest migration of the instantaneous Rivera-Pacific Euler pole since 0.78 Ma. *Geofis. Int. 37*(3), 153–169.

Bandy, W. L. and C. A. Mortera-Gutierrez (1995). The subducted Rivera-Cocos plate boundary: Where is it, what is it, and what is its relationship to the Colima rift? *Geophys. Res. Lett. 22*(22), 3075–3078.

Bard, P. Y. (1988). The Mexico earthquake of September 19, 1985–A theoretical investigation of large and small scale amplification effects in the Mexico City valley. *Earthquake Spectra 4*(3), 609.

Bianco, F., E. Del Pezzo, L. Malagnini, and A. Akinici (2005). Separation of depth-dependent intrinsic and scattering seismic attenuation in the northeastern sector of the Italian Peninsula. *Geophys. J. Int. 161*, 130–142.

Billen, M. (2009). Soaking slabs. *Nature Geoscience 2*, 744–746.

Burbach, G. V., C. Frohlich, W. D. Pennington, and T. Matsumoto (1984). Seismicity and tectonics of the subducted cocos plate. *J. Geophys. Res. 89*(B9), 7719–7735.

Campa, M. and P. Coney (1983). Tectono-stratigraphic terranes and mineral-resource distributions in Mexico. *Can. J. Earth Sci. 20*(6), 1040–1051.

Campillo, M., L. Margerin, and K. Aki (1998). *Seismology*, Chapter 7, pp. 87–99. New aspects of electromagnetic and acustic wave diffusion. Springer.

Canas, J. A., J. J. Egozcue, and L. Pujadas (1988). Seismic attenuation in southern Mexico using the coda Q method. *Bull. Seism. Amer. 78*(5), 1807–1817.

Cao, L. . and I. Jackson (1996). Seismic-frequency laboratory measurements of shear mode viscoelasticity in crustal rocks I: competition between cracking and plastic flow in thermally cycled Carrara marble. *Phys. Earth Planet. In. 94*, 105–119.

Castro, R. R., J. G. Anderson, and S. K. Singh (1990). Site response, attenuation and source spectra of S-waves along the Guerrero, Mexico, subduction zone. *Bull. Seism. Soc. Am. 80*(6), 1481–1503.

Castro, R. R. and L. Mungia (1993). Attenuation of P and S waves in the Oaxaca, Mexico, subduction zone. *Phys. Earth Planet. In. 76*, 179–187.

Castro, R. R., L. Mungia, C. J. Rebollar, and J. G. Acosta (1994). A comparative analysis of the quality factor Q for the regions of Guerrero and Oaxaca. *Geofisica Int. 33*, 373–383.

Chen, T. and R. W. Clayton (2009). Seismic attenuation structure in central Mexico: Image of a focused high attenuation zone in the mantle wedge. *J. Geophys. Res. 114*, B07304.

Choy, G. L. and J. L. Boatwright (1995). Global patterns of radiated seismic energy and apparent stress. *J. Geophys. Res. 100*(B9), 18,205–18,228.

Chung, T., K. Yoshimoto, and S. Yun (2010). The separation of intrinsic and scattering seismic attenuation in South Korea. *Bull. Seism. Amer. 100*(6), 3183–3193.

Cloos, M. (1993). Lithospheric buoyancy and collisional orogenesis - subduction of oceanic plateaus, continental margins, island arcs, spreading ridges, and seamounts. *Geol. Soc. Am. Bull. 105*(6), 715–737.

Cotte, N., A. Walpersdorf, V. Kostoglodov, M. Vernolle, J. A. Santiago, and M. Campillo (2009). Anticipating the next large silent earthquake in Mexico. *Eos*

Trans. AGU 90(21), 181.

Couch, R. and S. Woodcock (1981). Gravity and structure of the continental margins of southwestern Mexico and northwestern Guatemala. *J. Geophys. Res. 86*, 1829–1840.

Cruz-Jimenez, H., F. J. Chávez-Gracía, and T. Furumura (2009). Differences in attenuation of ground motion perpendicular to the Mexican subduction zone between Colima and Guerrero: An explanation based on numerical modeling. *Bull. Seism. Soc. Am. 99*(1), 400–406.

Dainty, A. and M. Toksoz (1981). Seismic codas on the Earth and the Moon - a comparison. *Phys. Earth Planet. In. 26*(4), 250–260.

Damon, P. E. and E. Montesinos (1978). Late Cenozoic volcanism and metallogenesis over an active benioff zone in Chiapas, Mexico. *Arizona Geol. Soc. Dig. 11*, 158–168.

Davies, J. H. and F. Von Blanckenburg (1995). Slab breakoff: A model of lithosphere detachment and its test in the magmatism and deformation of collisional orogens. *Earth Planet. Sci. Lett. 129*, 85–102.

Davis, P. M. and R. W. Clayton (2007). Application of the telegraph model to coda Q variations in southern California. *J Geophys Res-Sol Ea 112*(B9), B09302.

Davis, P. M., J. L. Rubinstein, K. H. Liu, S. S. Gao, and L. Knopoff (2000). Northridge earthquake damage caused by geologic focusing of seismic waves. *Science 289*, 1746–1750.

DeMets, C. and S. Traylen (2000). Motion of the Rivera plate since 10 Ma relative to the Pacific and North American plates and the mantle. *Tectonophysics 318*(1-4), 119–159.

DeMets, C. and D. Wilson (1997). Relative motions of the Pacific, Rivera, North American, and Cocos plates since 0.78 Ma. *J. Geophys. Res-Sol Ea. 102*(B2), 2789–2806.

Dickinson, W. R. and T. F. Lawton (2001). Carboniferous to Cretaceous assembly and fragmentation of Mexico. *Geol. Soc. Am. Bull. 113*(9), 1142–1160.

Dominguez, L. A., F. J. Sanchéz-Sesma, and P. M. Davis (2011). Scattering of teleseismic body waves by the lateral crustal heterogeneity at the Pacific trench of Mexico. *Bull. Seism. Amer. 101*(3), 1281–1290.

Dziewonski, A. M. (1979). Elastic and anelastic structure of the Earth. *Rev. Geophys. 17*(2), 303–312.

Eissler, H., L. Astiz, and H. Kanamori (1986). Tectonic setting and source parameters of the September 19, 1985 Michoacan, Mexico earthquake. *Geophys. Res. Lett. 13*(6), 569–572.

Ekström, G. and A. M. Dziewonski (1986). A very broad band analysis of the Michoacan, Mexico, earthquake of September 19, 1985. *Geophys. Res. Lett. 13*(6), 605–608.

Esteva, L. (1988). The Mexico Earthquake of September 19, 1985-Consequences, lessons, and impact on research and practice. *Earthquake Spectra 4*(3), 413–426.

Fedotov, S. A. (1981). Magma rates in feeding conduits of different volcanic centres. *J. Volcanol. Geoth. Res. 9*, 379–394.

Fehler, M., M. Hoshiba, H. Sato, and K. Obara (1992). Separation of scattering and intrinsic attenuation for the Kanto-Tokai region, Japan, using measurements of S-wave energy versus hypocentral distance. *Geophys J Int 108*, 787–800.

Fehler, M. and H. Sato (2003). Coda. *Pure appl. geophys. 160*, 541–554.

Ferrari, L. (2004). Slab detachment control on mafic volcanic pulse and mantle heterogeneity in central Mexico. *Geology 32*(1), 77–80.

Ferrari, L., M. López-Martínez, G. Aguirre-Díaz, and G. Carrasco-Núñez (1999). Space-time patterns of Cenozoic arc volcanism in central Mexico: from the Sierra Madre Occidental to the Mexican Volcanic Belt. *Geology 27*(4), 303–306.

Ferrari, L., M. Lopez-Martinez, and J. Rosas-Elguera (2002). Ignimbrite flare-up and deformation in the southern Sierra Madre Occidental, western Mexico: Impli-

cations for the late subduction history of the Farallon plate. *Tectonics 21*(4), 10.1029/2001TC001302.

Ferrari, L., C. Petrone, and L. Francalanci (2001). Generation of oceanic-island basalt-type volcanism in the western Trans-Mexican volcanic belt by slab rollback, asthenosphere infiltration, and variable flux melting. *Geology 29*(6), 507–510.

Ferrari, L., T. Tagami, M. Eguchi, M. Orozco-Esquivel, C. Petrone, J. Jacobo-Albarran, and M. Lopez-Martinez (2005). Geology, geochronology and tectonic setting of late Cenozoic volcanism along the southwestern Gulf of Mexico: The Eastern Alkaline Province revisited. *J. Volcanol. Geoth. Res. 146*(4), 284–306.

Feustel, A. J., C. I. Trifu, and T. I. Urbancic (1996). Rock-mass characterization using intrinsic and scattering attenuation estimates at frequencies from 400 to 1600 Hz. *Pure and Applied Geophysics 147*(2), 289–304.

Franco, S. I., V. Kostoglodov, K. M. Larson, V. C. Manea, M. Manea, and J. A. Santiago (2005). Propagation of the 2001-2002 silent earthquake and interplate coupling in the Oaxaca subduction zone, Mexico. *Earth Planets and Space 57*, 973–985.

Frankel, A. and R. Clayton (1986). Finite-difference simulations of seismic scattering - implications for the propagation of short-period seismic-waves in the crust and models of crustal heterogeneity. *J Geophys Res-Sol Ea 91*(B6), 6465–6489.

Frankel, A. and L. Wennerberg (1987). Energy-flux model of seismic coda - Separation of scattering and intrinsic attenuation. *Bull. Seism. Soc. Am. 77*(4), 1223–1251.

Furumura, T. and S. Singh (2002). Regional wave propagation from Mexican subduction zone earthquakes: The attenuation functions for interplate and inslab events. *Bull. Seism. Soc. Am. 92*(6), 2110–2125.

Gaite, B., A. Iglesias, A. Villaseñor, M. Herraiz, and J. F. Pacheco (2012). Crustal structure of Mexico and surrounding regions from seismic ambient noise tomography. *Geo-*

phys. J. Int. 188(3), 1413–1424.

Gao, S., H. Liu, P. M. Davis, and L. Knopoff (1996). Localized amplification of seismic waves and correlation with damage due to the Northridge earthquake: Evidence for focusing in Santa Monica. *Bull. Seism. Soc. Am. 86*, S209–S230.

Garcia, D., S. K. Singh, M. Herraiz, M. Ordaz, J. F. Pacheco, and H. Cruz-Jimenez (2009). Influence of subduction zone structure on coastal and inland attenuation in Mexico. *Geophys. J. Int. 179*(1), 215–230.

Gephart, J. W. (1994). Topography and subduction geometry in the central Andes: Clues to the mechanics of a noncollisional orogen. *J. Geophys. Res. 99*(B6), 12,279–12,288.

Gómez-Tuena, A., L. Mori, N. E. Rincón-Herrera, F. Ortega-Gutiérrez, J. Solé, and A. Iriondo (2011). The origin of a primitive trondhjemite from the Trans-Mexican Volcanic Belt and its implications for the construction of a modern continental arc. *Geology 36*, 471–474.

Gorbatov, A. and Y. Fukao (2005). Tomographic search for missing link between the ancient Farallon subduction and the present Cocos subduction. *Geophys. J. Int. 160*, 849–854.

Green II, H. W., W.-P. Chen, and M. R. Brudzinski (2010). Seismic evidence of negligible water carried below 400-km depth in subducting lithosphere. *Nature 467*, 828–831.

Grigoriu, M., S. E. Ruiz, and E. Rosenblueth (1988). The Mexico earthquake of September 19, 1985-Nonstationary models of seismic ground acceleration. *Earthquake Spectra 4*(3), 551–568.

Guadez, M. C., A. Zelt, M. B. Magnani, and A. Lavander (2006). BOLIVAR: Crustal structure of the caribbean-south america plate boundary at 70w. Eos Trans. AGU, Abstract T43D-1677.

Gutscher, M. A. (2002). Andean subduction styles and their effect on thermal structure

and interplate coupling. *J. S. Am. Earth Sci. 15*, 3–10.

Gutscher, M. A., R. Maury, J. P. Eissen, and E. Bourdon (2000). Can slab melting be caused by flat subduction? *Geology 28*, 535–538.

Gutscher, M. A., W. Spakman, and H. Bijwaard (2000). Geodynamics of flat subduction Seismicity and tomographic constraints from the Andean margin. *Tectonics 19*(5), 814–833.

Hacker, B. R., G. A. Abers, and S. M. Peacock (2003). Subduction factory - 1. Theoretical mineralogy, densities, seismic wave speeds, and H_2O contents. *J. Geophys. Res. 108*(B1), 2029.

Hauksson, E. and L. M. Jones (1995). The 1994 Northridge earthquake sequence in California: Seismological and tectonic aspects. *J. Geophys. Res. 100*(12), 335.

Herraiz, M. and A. Espinosa (1987). Coda waves - a review. *Pure and Applied Geophysics 125*(4), 499–507.

Hoshiba, M. (1991). Simulation of multiple-scattered coda wave excitation based on the energy conservation law. *Phys. Earth Planet. In. 67*, 123–136.

Hoshiba, M., A. Rietbrock, H. Scherbaum, F. Nakahara, and C. Haberland (2001). Scattering attenuation and intrinsic absorption using uniform and depth dependent model - Application to full seismogram envelope recorded in northern Chile. *J. Seismol. 5*, 157–179.

Hoshiba, M., H. Sato, and M. Fehler (1991). Numerical basis of the separation of scattering and intrinsic absorption from full seismogram envelope: a Monte-Carlo simulation of multiple isotropic scattering. *Pap. Meteorol. Geophys 42*(2), 65–91.

Houston, H. and H. Kanamori (1986). Source characteristics of the 1985 Michoacan, Mexico earthquake at periods of 1 to 30 seconds. *Geophys. Res. Lett. 13*(6), 597–600.

Husker, A. and P. M. Davis (2009). Tomography and thermal state of the Cocos plate subduction beneath Mexico City. *J. Geophys. Res. 114*, B04306.

Husker, A., V. Kostoglodov, V. M. Cruz-Atienza, D. Legrand, N. M. Shapiro, J. S. Payero, M. Campillo, and E. Huesca-Pérez (2012). Temporal variations of non-volcanic tremor (NVT) locations in the Mexican subduction zone: Finding the NVT sweet spot. *Geochem. Geophy. Geosyst. 13*, Q03011.

Iglesias, A., R. W. Clayton, X. Pérez-Campos, S. Singh, J. Pacheco, D. García, and C. Valdés-González (2010). S wave velocity structure below central Mexico using high-resolution surface wave tomography. *J. Geophys. Res. 115*, B06307.

Ishii, M., P. M. Shearer, H. Houston, and J. E. Vidale (2005). Extent, duration and speed of the 2004 Sumatra-Andaman earthquake imaged by the Hi-Net array. *Nature 435*, 933–936.

Jackson, D. D. and D. L. Anderson (1970). Physical mechanisms of seismic-wave attenuation. *Rev. Geophys. 8*(1), 1–63.

Jackson, I. (1993). Progress in the experimental-study of seismic-wave attenuation. *Annu. Rev. Earth Pl. Sc. 21*, 375–406.

Jackson, I. (2000). *Laboratory measurements of seismic wave dispersion and attenuation: Recent progress* (S. Karato ed.), Volume 117, pp. 265–289. AGU, Washington, D.C.

Jackson, J., D. McKenzie, K. Priestley, and B. Emmerson (2008). New views on the structure and rheology of the lithosphere. *J. Geol. Soc. London 165*, 453–465.

Jacobson, R. S. (1987). An investigation into the fundamental relationships between attenuation, phase dispersion, and frequency using seismic refraction profiles over sedimentary structures. *Geophysics 52*(1), 72–87.

Jin, A., K. Mayeda, A. David, and K. Aki (1994). Separation of intrinsic and scattering attenuation in southern California using TERRAscope data. *J Geophys Res 99*(B9),

17,835–17,848.

Jödicke, H., A. Jording, L. Ferrari, J. Arzate, K. Mezger, and L. Rüpke (2006). Fluid release from the subducted Cocos plate and partial melting of the crust deduced from magnetotelluric studies in southern Mexico: Implications for the generation of volcanism and subduction dynamics. *J. Geophys. Res. 111*, B08102.

Jung, H., H. W. Green II, and L. F. Dobrzhinetskaya (2004). Intermediate-depth earthquake faulting by dehydration embrittlement with negative volume change. *Nature 428*, 545–549.

Kanamori, H., P. C. Jennings, S. Singh, and L. Astiz (1993). Estimation of strong ground motions in Mexico City expected for large earthquakes in the Guerrero seismic gap. *Bull. Seism. Soc. Am. 83*(3), 811–829.

Keppie, J. D. (2004). Terranes of Mexico revisited: A 1.3 billion year odyssey. *Geology Review 46*, 765–794.

Kim, Y., C. R. W., and M. N. Jackson (2010). Geometry and seismic properties of the subducting Cocos plate in central Mexico. *J. Geophys. Res. 115*, B06310.

Kinoshita, S. (2008). Deep-Borehole-Measured Qp and Qs attenuation for two Kanto sediment layer sites. *Bull. Seism. Soc. Am. 98*(1), 463–468.

Knopoff, L. (1964). Q. *Reviews of Geophysics 2*(4), 625–660.

Kostoglodov, V., W. L. Bandy, J. Domínguez, and M. Mena (1996). Gravity and seismicity over the Guerrero seismic gap, Mexico. *Geophys. Res. Lett. 23*(23), 3385–3388.

Kostoglodov, V., A. Husker, N. Shapiro, J. S. Payero, M. Campillo, N. Cotte, and R. W. Clayton (2010). The 2006 slow slip event and nonvolcanic tremor in the Mexican subduction zone. *Geophys. Res. Lett. 37*, L24301.

Kostoglodov, V., S. Singh, J. A. Santiago, and S. I. Franco (2003). A large silent earthquake in the Guerrero seismic gap, Mexico. *Geophys. Res. Lett. 30*(15), 1807.

Lallemand, S. and A. Hueret (2005). On the relationships between slab dip, back-arc stress, upper plate absolute motion, and crustal nature in subduction zones. *Geochem. Geophy. Geosy. 6*, Q09006.

Larson, K. M., V. Kostoglodov, S. Miyazaki, and J. A. Santiago (2007). The 2006 aseismic slow slip event in Guerrero, Mexico: New results from GPS. *Geophys. Res. Lett. 34*, L13309.

Lassiter, J. C. and J. F. Luhr (2001). Osmium abundance and isotope variations in mafic Mexican volcanic rocks: Evidence for crustal contamination and constraints on the geochemical behavior of osmium during partial melting and fractional crystallization. *Geochem. Geophy. Geosy. 2*, 2000GC000116.

León Soto, G., J. F. Ni, S. P. Grand, E. Sandvol, R. W. Valenzuela, M. Gúzman Spaziale, J. M. Gómez Gónzalez, and T. Domínguez Reyes (2009). Mantle flow in the Rivera–Cocos subduction zone. *Geophys. J. Int. 179*, 1004–1012.

Lermo, J., M. Rodriguez, and S. K. Singh (1988). The Mexico earthquake of September 19, 1985– Natural period of sites in the valley of Mexico from microtremor measurements and strong motion data. *Earthquake Spectra 4*, 805–814.

Li, L. and J. Lu (2010). Ambiguity between the residual geometrical spreading and scattering attenuation. *Pure and Applied Geophysics 167*, 1579–1580. 10.1007/s00024-010-0234-6.

Lindsay, G. (1914). A study of longitudinal vibration of waves. *Phys. Rev. 3*, 397–438.

Lowry, A., K. M. Larson, V. Kostoglodov, and R. Bilham (2001). Transient fault slip in Guerrero, southern Mexico. *Geophys. Res. Lett. 28*(19), 3753–3756.

Luhr, J. F. (1997). Extensional tectonics and the diverse primitive volcanic rocks in the western Mexican volcanic belt. *Can. Mineral. 35*, 473–500.

Macías, J. L. (2007). Geology and eruptive history of some active volcanoes of Mexico. In

S. A. Alaniz-Álvarez and S. A. Nieto-Samaniego (Eds.), *Geology of Mexico: Celebrating the Centenary of the Geological Society of Mexico*, Number 442. The Geological Society of America.

Mammerickx, J. and K. Klitgord (1982). Northern East Pacific Rise: Evolution from 25 m.y. B.P. to the present. *J Geophys Res 87*(NB8), 6751–6759.

Manea, M., V. Manea, L. Ferrari, and V. Kostoglodov (2005). Tectonic evolution of the Tehuantepec Ridge. *Earth Planet. Sci. Lett. 238*, 64–77.

Manea, V. and M. Gurnis (2007). Subduction zone evolution and low viscosity wedges and channels. *Earth Planet. Sci. Lett. 264*, 22–45.

Manea, V. C. and M. Manea (2011). Flat-slab thermal structure and evolution beneath central Mexico. *Pure Appl. Geophys. 168*, 1475–1487.

Manea, V. C., M. Manea, V. Kostoglodov, C. A. Currie, and G. Sewell (2004). Thermal structure, coupling and metamorphism in the Mexican subduction zone beneath Guerrero. *Geophys. J. Int. 158*, 775–784.

Manea, V. C., M. Manea, V. Kostoglodov, and G. Sewell (2005). Thermo-mechanical model of the mantle wedge in Central Mexican subduction zone and a blob tracing approach for the magma transport. *Phys. Earth Planet. In. 149*, 154–186.

Margerin, L., M. Campillo, and N. Shapiro (1999). Residence time of diffuse waves in the crust as a physical interpretation of coda Q: Application to seismograms recorded in Mexico. *Geophys J Int 138*, 343–352.

Margerin, L., M. Campillo, and B. V. Tiggelen (1998). Radiative transfer and diffusion of waves in a layered medium : New insight into coda Q. *Geophys. J. Int. 134*, 596–612.

Margerin, L., M. Campillo, and B. V. Tiggelen (2000). Monte Carlo simulation of multiple scattering of elastic waves. *Journal of Geophysical Research 105*(B4), 7873–7892.

Marquez, A., R. Oyarzun, C. De Ignacio, and M. Doblas (2001). Southward migration of volcanic activity in the central Mexican Volcanic Belt: Asymmetric extensions within a two-layer crustal stretching model. *J. Volcanol. Geoth. Res. 112*(1-4), 175–187.

Marquez, A., R. Oyarzun, M. Doblas, and S. Verma (1999). Alkalic (ocean-island basalt type) and calc-alkalic volcanism in the Mexican volcanic belt: A case for plume-related magmatism and propagating rifting at an active margin? *Geology 27*, 51–54.

Marquez, A., S. Verma, F. Anguita, R. Oyarzun, and J. Brandle (1999). Tectonics and volcanism of Sierra Chichinautzin: extension at the front of the Central Trans-Mexican Volcanic belt. *J. Volcanol. Geoth. Res. 93*(1-2), 125–150.

Mayeda, K., S. Koyanagi, M. Hoshiba, K. Aki, and Y. Zeng (1992). A comparative study of scattering, intrinsic, and coda Q^{-1} for Hawaii, Long Valley, and central California between 1.5Hz and 15.0Hz. *J. Geophys. Res-Sol Earth 97*(B5), 6643–6659.

Mayeda, K. and W. R. Walter (1996). Moment, energy, stress drop, and source spectra of the western United States earthquakes from regional coda envelopes. *J. Geophys. Res. 101*(B5), 11,195–11,208.

McKenzie, C. K., G. P. Stacey, and M. T. Gladwin (1982). Ultrasonic characteristics of a rock mass. *Int. J. Rock Mech. Min. Sci. and Geochem. 19*, 25–30.

Mendoza, C. and S. H. Hartzell (1989). Slip distribution of the 19 September 1985 Michoacan, Mexico, earthquake: Near-source and teleseismic constraints. *Bull. Seism. Soc. Am. 79*(3), 655–660.

Miller, D. K. (1998). Lessons learned from the Northridge earthquake. *Engineering Structures 29*(4-6), 249–260.

Moore, G., C. Marone, I. Carmichael, and P. Renne (1994). Basaltic volcanism and extension near the intersection of the Sierra Madre volcanic province and the Mexican Volcanic Belt. *Geological Society of America Bulletin 106*(4), 382–394.

Morán-Zenteno, D., M. Cerca, and J. D. Keppie (2007). The Cenozoic tectonic and magmatic evolution of southwestern Mexico: Advances and problem of interpretation. In S. A. Alaniz-Álvarez and S. A. Nieto-Samaniego (Eds.), *Geology of Mexico: Celebrating the Centenary of the Geological Society of Mexico*, Volume 422, pp. 71–91. Geological Society of America.

Morán-Zenteno, D., P. Corona-Chavez, and G. Tolson (1996). Uplift and subduction erosion in southwestern Mexico since the Oligocene: Pluton geobarometry constraints. *Earth Planet. Sci. Lett. 141*, 51–65.

Morozov, I. (2004). Crustal scattering and some artifacts in receiver function images. *B Seismol Soc Am 94*(4), 1492–1499.

Morozov, I. and H. Zheng (2006). Effects of trench-zone scattering on receiver functions over a subduction zone: A 3-d finite-difference modelling study. *Tectonophysics 420*(1-2), 317–332.

Morozov, I. B. (2008). Geometrical attenuation, frequency dependence of Q, and the absorption band problem. *Geophys J Int 175*(1), 239–252.

Morozov, I. B. (2009). Thirty years of confusion aroung "Scattering Q"? *Seismol. Res. Lett. 80*(1), 5–7.

Muller, R. D., M. Sdrolias, C. Gaina, and W. R. Roest (2008). Age, spreading rates, and spreading asymmetry of the world's ocean crust. *Geochem. Geophy. Geosy. 9*, Q04006.

Nieto-Samaniego, S. A., G. Silva-Romo, M. H. Eguiza-Castro, and C. C. Mendoza-Rosales (2006). Latest Cretaceous to Miocene deformation events in the eastern Sierra Madre del Sur, Mexico, inferred from the geometry and age of major structures. *Geol. Soc. Am. Bull. 118*(1/2), 238–252.

Nixon, G. T. (1982). The relationship between Quaternary volcanism in central Mexico and the seismicity and structure of subducted ocean lithosphere. *Geol. Soc. Am.*

Bull. 93(6), 514–523.

Ogawa, Y., M. Mishina, T. Goto, H. Satoh, N. Oshiman, T. Kasaya, Y. Takahashi, T. Nishitani, S. Sakana, M. Uyeshima, Y. Takashi, Y. Honkura, and M. Matsushima (2001). Magnetotelluric imaging of fluids in intraplate earthquake zones, NE Japan back arc. *Geophys. Res. Lett. 28*(19), 3741–3744.

Okal, E. A. and J. C. Borrero (2011). The 'tsunami earthquake'of 1932 June 22 in Manzanillo, Mexico: Seismological study and tsunami simulations. *Geophys. J. Int. 187*(3), 1443–1459.

Ordaz, M. and S. K. Singh (1992). Source spectra and spectral attenuation of seismic-waves from Mexican earthquakes, and evidence of amplification in the hill zone of Mexico-City. *Bull. Seism. Soc. Am. 82*(1), 24–43.

Ottemöller, L., N. M. Shapiro, S. K. Singh, and J. F. Pacheco (2002). Lateral variation of Lg wave propagation in southern Mexico. *J. Geophys. Res. 107*(B1), 10.1029/2001JB000206.

Pacheco, J. and S. Singh (2010). Seismicity and state of stress in Guerrero segment of the Mexican subduction zone. *J. Geophys. Res. 115*, B01303.

Padhy, S. (2005). A scattering model for seismic attenuation and its global applications. *Phys. Earth Planet. In. 148*, 1–12.

Pardo, M. and G. Suarez (1995). Shape of the subducted Rivera and Cocos plates in southern Mexico - Seismic and tectonic implications. *J. Geophys. Res-Sol Ea. 100*(B7), 12357–12373.

Payero, J. S., V. Kostoglodov, N. Shapiro, T. Mikumo, A. Iglesias, X. Pérez-Campos, and R. W. Clayton (2008). Nonvolcanic tremor observed in the Mexican subduction zone. *Geophys. Res. Lett. 35*, L07305.

Pérez-Campos, X., R. W. Clayton, A. Iglesias, T. Chen, Y. Kim, D. Melgar-Moctezuma,

C. Valdés-González, and J. F. Pacheco (2008). VEOX: A new seismic line in Mexico to reveal Cocos behavior. *Eos. Trans. AGU*, Abstract T23B–2039.

Pérez-Campos, X., Y. Kim, A. Husker, P. M. Davis, R. W. Clayton, A. Iglesias, J. Pacheco, S. Singh, V. C. Manea, and M. Gurnis (2008). Horizontal subduction and truncation of the Cocos Plate beneath central Mexico. *Geophys. Res. Lett. 35*, L18303.

Radiguet, M., F. Cotton, M. Vernolle, M. Campillo, B. Valette, V. Kostoglodov, and N. Cotte (2011). Spatial and temporal evolution of a long term slow slip event: The 2006 Guerrero slow slip event. *Geophys. J. Int. 184*, 816–828.

Ramírez-Herrera, M., V. Kostoglodov, and J. Urrutia-Fucugauchi (2011). Overview of recent coastal tectonic deformation in the Mexican subduction zone. *Pure Appl. Geophys. 168*, 1415–1433.

Rautian, T. and V. Khalturin (1978). The use of the coda for determination of the earthquake source spectrum. *Bull. Seism. Amer. 68*(4), 923–948.

Robinson, D., M. Sambridge, and R. Snieder (2011). A probabilistic approach for estimating the separation between a pair of earthquakes directly from their coda waves. *J. Geophys. Res-Sol Earth 116*, B043309.

Romanowicz, B. and J. Durek (2000). Seismological constraints on attenuation in the Earth: A review. In S. I. Karato (Ed.), *Earth's deep interior: Mineral physics and Tomography from the atomic to global scale*. AGU, Washington, D.C.

Romanowicz, B. and B. Mitchell (2008). *Q in the earth from crust to core* (G. Schubert ed.), Volume 1, pp. 731. Elsevier, New York.

Rondenay, S., M. Bostock, and J. Shragge (2001). Multiparameter two–dimensional inversion of scattered teleseismic body waves 3. Application to the Cascadia 1993 data set. *J. Geophys. Res 106*(30), 795–30.

Rosenblueth, E., M. Ordaz, F. J. Sánchez-Sesma, and S. Singh (1989). The Mexico earth-

quake of September 19, 1985-Design spectra for Mexico's Federal District. *Earthquake Spectra 5*(1), 273–291.

Rost, S. and C. Thomas (2002). Array seismology: Methods and applications. *Rev. Geophys. 40*(3), 1008.

Rubinstein, B., N. Hilairet, E. Balan, and M. Lazzeri (2010). Non-volcanic tremor: A window into the roots of fault zones. In S. Cloetingh and J. Negendank (Eds.), *New Frontiers in Integrated Solid Earth Sciences*, pp. 287–314. Springer, Dordrecht, Netherlands.

Sánchez-Sesma, F. J., S. Chávez-Perez, M. Suárez, M. A. Bravo, and L. E. Pérez-Rocha (1988). The Mexico Earthquake of September 19, 1985—On the seismic response of the Valley of Mexico. *Earthquake Spectra 4*(3), 569–589.

Sato, H. (1994). Multiple isotropic scattering model including P-S conversions for the seismogram envelope formation. *Geophys J Int 117*, 487–494.

Sato, H. and M. Fehler (2009). *Seismic Wave Propagation and Scattering in the Heterogenous Earth*. Springer.

Schellart, W. P. (2008). Overriding plate shortening and extension above subduction zones: A parametric study to explain formation of the Andes Mountains. *Geol. Soc. Am. Bull. 11-12*, 1441–1454.

Sedlock, R., F. Ortega-Gutiérrez, and R. Speed (1993). Tectonostratigraphic terranes and tectonic evolution of Mexico. *Geol. Soc. Am. Special Papers 278*, 153.

Seed, H. B., M. P. Romo, J. I. Sun, A. Jaime, and J. Lysmer (1988). The Mexico earthquake of september 19, 1985—relationships between soil conditions and earthquake ground motions. *Earthquake Spectra 4*(4), 687–729.

Shapiro, N., M. Campillo, S. Singh, and J. Pacheco (1998). Seismic channel waves in the accretionary prism of the Middle America Trench. *Geophysical Research Letters 25*(1),

101–104.

Shapiro, N., K. Olsen, and S. Singh (2000). Wave-guide effects in subduction zones: Evidence from three-dimensional modeling. *Geophys. Res. Lett 27*(3), 433–436.

Sheth, H. C., I. S. Torres-Alvarado, and S. Verma (2000). Beyond subduction and plumes: A unified tectonic-petrogenetic model for the Mexican volcanic belt. *Int. Geol. Rev. 42*, 1116–1132.

Singh, S., L. Astiz, and J. Havskov (1981). Seismic gaps and recurrence periods of large earthquakes along the Mexican subduction zone: A reexamination. *Bull. Seism. Soc. Am. 71*(3), 827–843.

Singh, S., A. Iglesias, M. Ordaz, X. Pérez-Campos, and L. Quintanar (2011). Estimation of strong ground motions in Mexico City from a repeat of the M∼7.0 Acambay earthquake 1912. *Bull. Seism. Soc. Am. 101*(5), 2015–2028.

Singh, S., E. Mena, and R. Castro (1988). Some aspects of source characteristics of the 19 September 1985 Michoacan earthquake and ground motion amplification in and near Mexico City from strong motion data. *Bull. Seism. Soc. Am. 78*(2), 451–477.

Singh, S., J. Pacheco, D. García, and A. Iglesias (2006). An estimate of shear-wave Q of the mantle wedge in Mexico. *Bull. Seism. Soc. Am. 96*(1), 176–187.

Singh, S. and M. Pardo (1993). Geometry of the Benioff zone and state of stress in the overriding plate in central Mexico. *Geophys. Res. Lett. 20*, 1483–1486.

Skinner, S. M. and R. W. Clayton (2011). An evaluation of proposed mechanisms of slab flattening in central Mexico. *Pure Appl. Geophys. 168*, 1461–1474.

Snieder, R. (2004). Extracting the Green's function from the correlation of coda waves: A derivation based on stationary phase. *Physical Review E 69*, 046610.

Song, T., D. V. Helmberger, M. R. Brudzinski, R. W. Clayton, P. M. Davis, X. Pérez-Campos, and S. Singh (2009). Subducting slab ultra-slow velocity layer coincident with

silent earthquakes in southern Mexico. *Science 324*, 502–506.

Stock, J. (1988). Uncertainties and implications of the late cretaceous and tertiary position of North America relative to the Farallon, Kula, and Pacific plates. *Tectonics 7*(6), 1339–1384.

Stock, J. and J. Lee (1994). Do microplates in subduction zones leave a geological record? *Tectonics 13*(6), 1472–1487.

Stubailo, I., C. Beghein, and P. M. Davis (2012). Structure and anisotropy of the Mexico subduction zone based on Rayleigh-wave analysis and implications for the geometry of the Trans-Mexican Volcanic belt. *J. Geophys. Res. 117*, B05303.

Suarez, G., T. Monfret, G. Wittlinger, and C. David (1990). Geometry of subduction and depth of the seismogenic zone in the Guerrero gap, Mexico. *Nature 345*(6273), 336–338.

Suteau, A. M. and J. H. Whitcomb (1979). A local earthquake coda magnitude and its relation to duration, moment M_0, and local Richter magnitude M_l. *Bull. Seism. Amer. 69*(2), 353–368.

Takada, A. (1994). The influence of regional stress and magmatic input on styles of monogenetic and polygenetic volcanism. *J. Geophys. Res. 99*(B7), 13,563–13,573.

Tselentis, G. A. (1998). Intrinsic and scattering seismic attenuation in W. Greece. *Pure Appl. Geophys. 153*, 703–712.

Urrutia-Fucugauchi, J. and J. H. Flores-Ruiz (1996). Bouguer gravity anomalies and regional crustal structure in Central Mexico. *Int. Geol. Rev. 38*(2), 179–194.

Valdés, C. M., W. D. Mooney, S. Singh, R. P. Meyer, J. H. Lomnitz, J. H. Luetgert, B. T. Helsley, B. T. R. Lewis, and M. Mena (1986). Crustal structure of Oaxaca, Mexico, from seismic refraction measurements. *Bull. Seism. Soc. Am. 76*(2), 547–563.

Valdés-González, C. and R. P. Meyer (1996). Seismic structure between the Pacific coast and Mexico City from the Petatlán earthquake (Ms= 7.6) aftershocks. *Geofis. Int. 35*, 377.

Van Der Lee, S. and G. Nolet (1997). Upper mantle S velocity structure of North America. *J. Geophys. Res. 102*(B10), 22,815–22,838.

Vergnolle, M., A. Walpersdorf, V. Kostoglodov, P. Tregoning, J. A. Santiago, N. Cotte, and S. I. Franco (2010). Slow slip events in Mexico revised from the processing of 11 year GPS observations. *J. Geophys. Res. 115*, B08403.

Verma, S. (2002). Absence of Cocos plate subduction-related basic volcanism in southern Mexico: A unique case on Earth? *Geology 30*(12), 1095–1098.

Wagner, L. S., M. L. Anderson, J. M. Jackson, S. L. Beck, and G. Zandt (2008). Seismic evidence for orthopyroxene enrichment in the continental lithosphere. *Geology 36*, 935–038.

Walpersdorf, A., N. Cotte, V. Kostoglodov, M. Vergnolle, M. Radiguet, J. A. Santiago, and M. Campillo (2011). Two successive slow slip events evidenced in 2009–2010 by a dense GPS network in Guerrero, Mexico. *Geophys. Res. Lett. 38*, L15307.

Wu, R. and K. Aki (1985). Elastic wave scattering by a random medium and the small-scale inhomogeneities in the lithosphere. *J. Geophys. Res 90*(B12), 10,261–10,273.

Xie, J. (2010). Can we improve estimates of seismological q using a new "geometrical spreading" model? *Pure and Applied Geophysics 167*(10), 1147–1162.

Xie, J. and M. Fehler (2009). Comment on "thirty years of confusion". *Seismol. Res. Lett. 80*, 648–649.

Yang, T., S. P. Grand, D. Wilson, M. Gúzman-Speziale, J. M. Gómez-González, T. Domínguez-Reyes, and J. Ni (2009). Seismic structure beneath the Rivera subduction zone from finite-frequency seismic tomography. *J. Geophys. Res-Sol Ea. 114*,

B01302.

Yoshimoto, K. (2000). Monte carlo simulation of seismogram envelopes in scattering media. *J Geophys Res-Sol Ea 105*(B3), 6153–6161.

Yoshioka, S., T. Mikumo, V. Kostoglodov, K. M. Larson, A. Lowry, and S. Singh (2004). Interplate coupling and a recent aseismic slow slip event in the Guerrero seismic gap of the Mexican subduction zone, as deduced from GPS data inversion using a Bayesian information criterion. *Phys. Earth Planet. In. 146*, 513–530.

Zeng, Y. (1993). Theory of scattered P- wave and S- wave energy in a random isotropic scattering medium. *B Seismol Soc Am 83*(4), 1264–1276.